Synthesis, characterization and photocatalytic activity of BiOX (X = Cl, I, Br) and their composites with carbon nanotubes (CNT)

Ph.D. Thesis

Nikita Sharma

Supervisor:	Prof. Klara Hernadi
Co-Supervisors:	Dr. Pap Zsolt
	Dr. Seema Garg

Doctoral School of Environmental Chemistry

Department of Applied and Environmental Chemistry

Faculty of Science and Informatics, University of Szeged

Szeged

2021

Dedicated to my beloved family

for their endless support and love for me

TABLE OF CONTENTS

List of Abbreviations

AOP	**A**dvanced **O**xidation **P**rocess
BiOX	**Bi**smuth **O**xy **H**alide
CB	**C**onduction **B**and
CNT	**C**arbon **N**ano **T**ube
DRS	**D**iffuse **R**eflectance **S**pectroscopy
MWCNT	**M**ulti-**W**alled **C**arbon **N**ano **T**ube
RhB	**Rh**odamine **B**
SWCNT	**S**ingle-**W**alled **C**arbon **N**ano **T**ube
SEM	**S**canning **E**lectron **M**icroscopy
TEM	**T**ransmission **E**lectron **M**icroscopy
VB	**V**alence **B**and
XRD	**X**-**R**ay **D**iffraction

1. Introduction

Water is an indispensable resource for every living being and used in nearly all sectors including agriculture, industry and household. The demand for water sources has increased more than three times since 1950. The following two reasons are attributed to water scarcity: (a) Overconsumption of water, (b) Decrease in water quality which is primarily due to reckless discharge of pollutants largely by the industries, such as textile, pharmaceutical, pesticides and polymer industries *etc*. **Figure 1** shows parts of the globe distributed and categorized into water-stressed regions in 2019. Consequently, water shortage would halt economic growth of the nation and cause several environmental issues which may have direct impact on every living organism on this planet.

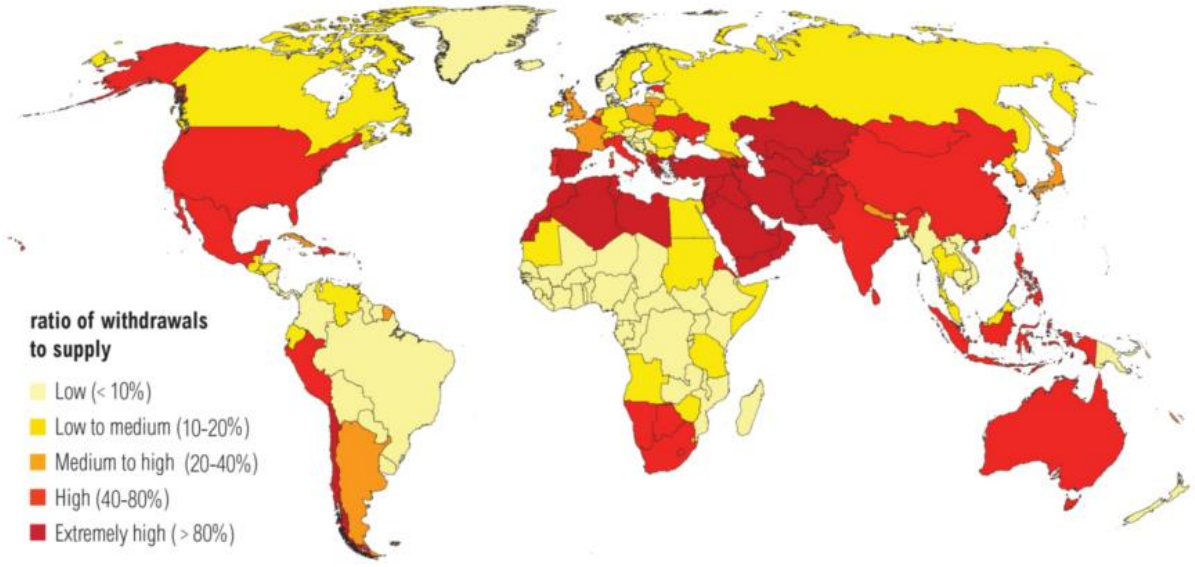

Figure 1. Parts of the globe at risk from water scarcity by 2040.

The issues concerning water pollution have risen over the past few decades. Some authors have called contaminated water an *"invisible crisis"*. According to a report by the World Economic Forum, almost 40 million liters of wastewater is disposed of into rivers and lakes in India on a daily basis. The United Nations has clearly estimated over 80% of wastewater is discharged back into the environment without any form of treatment. The report of the World Water Development Program 2018-UN also predicts that almost 6 billion people will suffer from water pollution by 2050 [1].

The prime reason that could be held accountable for this upcoming situation is the constant increase in contamination level of the available water resources. Factors like population growth, proliferation of agricultural activities, increased economic activity and inadequate treatment of sewage and industrial waste effluents act as an ultimate driver for increasing water pollution. Water crisis, thus, stands among the top 5 global risks that will have devastating effect on the world economy by 2050.

Richard Damania, one of the top economists in the World Bank's water program, has made several wake-up calls in this regard. As rightly quoted by him: *"Pollution affects countries, both rich and poor. It's bad all around. It is just the cocktails of chemicals that change. Plastics and pharmaceutical contaminants are problems everywhere."* The only solution to this problem is to treat the industrial effluents since there is no alternative to water resources that can make life sustainable. Therefore, scientists and researchers around the world are continuously putting efforts to develop effective technologies for treating wastewater.

2. Literature review

2.1 Background

2.1.1 Phenols and dyes: threat to environment

Nowadays, a number of harmful chemicals can be found in water supply, arising from industries, including phenols and phenolic compounds, pharmaceuticals, pesticides and synthetic dyes. Their improper disposal and handling pose a serious threat to human health and ecosystem. Therefore, it becomes imperative to treat them before discharging into water bodies.

The US Environmental Protection Agency (EPA), National Pollutant Release Inventory (NPRI) of Canada and the European Union has shed light on increasing phenol pollution levels in several water reservoirs and listed it under the category of priority pollutant. Its long-term persistence, bio-resistant nature and toxicity towards living organisms has raised the concerns for its removal. The main source of phenol and phenolic compounds include discharge from pulp and paper industries, resin manufacturing, pharmaceutical, petrochemical, oil refining, coking operations, pesticide production and agrochemicals. Due to its wide scale applications, it seems that the production of phenol will not cease so it becomes critical to focus on the treatment of industrial effluents containing phenols and phenol-based contaminants for a sustainable environment. However, oxidation and disinfection processes for phenol removal leads to other carcinogenic compounds like chlorophenols. Therefore, phenol removal by environmentally friendly methods is highly desirable because its effect on human health can be both acute and chronic. For instance, long-term exposure to phenols can result in shortness of breath, muscle weakness, coma, tremor and respiratory failure or can be lethal in humans. The chronic effects were observed in animals exposed to phenol like neurological symptoms, kidney and liver toxicity, irritation in the gastrointestinal tract and cardiovascular effects [2]. Moreover, phenol can be chemically transferred to other compounds like halophenols which are even more hazardous for living beings.

Besides phenols, the other most popular class of pollutant comes from textile industries that accounts to almost 17-20% of total wastewater pollution alone [3]. **Figure 2** shows the comparison of dye effluent discharge from different industries with the textile industry generating more than half of the existing dye effluents into the environment [4].

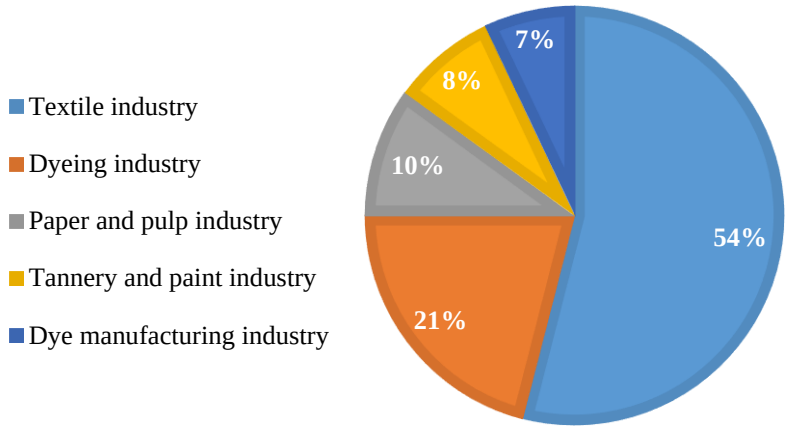

Figure 2. Comparison of dye effluent discharge from various industries.

The dye industries produce around 80 billion pieces of garments annually and for a ton of dyed fabric nearly 200 tons of water is used which indicates a huge amount of wastewater is being generated at the end of the process. More than 700,000 tons of dyes are produced annually. Among many dyes, the most commonly used is azo dye which is characterized by the nitrogen π-bonds and comprises 60-70% of the whole dye industry [3]. Azo dyes are known for their chemical stability and found to be widely used in several sectors in today's market including textile industry, cosmetics, printing and many more consumer products. These dyes break down into aromatic amines upon certain conditions which increase the risk of cancer. Also, they do not dissipate rather stay in the air that we breathe or may even be absorbed through the skin. Azo dyes have also been reported to interfere with the solubility of gases in water reservoirs. Exposure to such synthetic dyes can lead to skin irritation, rash, allergic reaction and cancer in severe cases. Surprisingly, as stated by the World Bank, 72 noxious chemicals come from the textile dyeing industry in the water supply. Dye pollution is, therefore, a "year-round epidemic". One of the popular azo dye is rhodamine B (RhB), 9-(2-Carboxyphenyl)-6-(diethylamino)-*N*, *N*-diethyl-3*H*-xanthen-3-iminium chloride. It is a waste soluble cationic xanthene dye. It is extensively used in food, textile and photographic industry, biological stain and tracing agent [6]. Due to its toxicity, ingestion of this dye can cause irritation in the eyes, skin and respiratory tract. Studies have shown its neurotoxicity, reproductive and developmental toxicity, carcinogenicity and chronic toxicity for humans and animals [6,7]. Hence, treatment of these waste effluents becomes vital. In addition to such proper waste disposal treatments, one great approach to avoid problems associated with water scarcity and environmental pollution is to reuse these treated wastewater for agricultural and industrial purposes.

Previously, different conventional methods were used for treating industrial wastewater such as biological methods, chemical precipitation, coagulation and flocculation, incineration or adsorption process. The downside of these methods largely outweighs its potential gains. Some of their disadvantages can be listed as too slow a process, large space requirement for operation, waste chemicals produced at the end which generates secondary harmful products and its compatibility with the environment. For instance, biological treatment needs a longer time to show an effect, and methods like adsorption or chemical precipitation results in transfer of pollutants from one phase to another (known as sludge) and thereby, increasing the challenges for its disposal. On the other hand, methods like chlorination, although effective in killing microorganisms, it produce more toxic by-products and causes cancer. Through continuous efforts and massive amounts of studies on the severe impacts of such hazardous waste on living beings and ecosystems, scientific studies are now being used as a tool for the development of new environmentally friendly treatment technologies for industrial effluents.

2.2 Advanced Oxidation Process (AOP)

Advanced Oxidation Process (AOP) is among the advanced technologies capable of degrading a wider section of contaminants (partially or totally) by reduction and oxidation reactions in water. It can be defined as the oxidation process that is based on the generation of highly reactive species (free radicals primarily hydroxyl radicals) and is widely used for treating wastewater containing recalcitrant organic pollutants at low concentrations. Other reactive species are also generated during the reaction such as superoxide ($O_2^{\cdot-}$) and hydrogen peroxide (H_2O_2). The overall effectiveness of AOPs is governed mainly by the production of hydroxyl radicals due to their high oxidation potential (2.70 eV) after fluorine, and its non-selective nature that results in complete mineralization of a wide range of organic pollutants to harmless end-products like carbon dioxide, water and inorganic salts. One of the major advantages of this method over traditional methods is no generation of waste or sludge. AOPs initially were used for treating drinking water in the 1980s and later extended for the treatment of various kinds of wastewater due to its potential to degrade refractory organic and some inorganic contaminants. Broadly, AOPs can be grouped under different categories based on: (a) chemical oxidants used (for, *e.g.* O_3, O_3/H_2O_2), (b) ultraviolet photolysis, or (c) heterogeneous photocatalysis. This thesis focuses on the study of the removal of pollutants by heterogeneous photocatalysis. Thus, in the subsequent sections you will find discussions related to it including semiconductors (solid state theory), mechanism

of heterogeneous photocatalysis and conventional and non-conventional semiconductor photocatalysts in use.

2.3 Heterogeneous Photocatalysis

Heterogeneous photocatalysis can be defined as *"Change in the rate of a chemical reaction or its initiation under the action of ultraviolet, visible, or infrared radiation in the presence of a substance, the photocatalyst that absorbs light and is involved in the chemical transformation of the reaction partners"* [9]. The popularity of heterogeneous photocatalysis dates back to 1972 when Fujishima and Honda first reported photochemical splitting of water molecules using TiO_2 as photoanode under UV light [10]. Since then, it has grown rapidly over the past few decades and included applications like solar water splitting, removal of contaminants from water and air, fabricating anti-fogging surfaces, solar cells/batteries, NO_x and heavy metal removal and so on. Some other areas of its applications involve organic syntheses under mild conditions and construction areas as well. The ability to inactivate different microorganisms further makes it a more promising tool for water disinfection. The process could be applied either as the final step in wastewater treatment plants or directly used for disinfection. Currently in some cases heterogeneous photocatalysis is also combined with other AOPs technologies. It has several advantages over conventional methods, like ambient temperature conditions, no strong oxidants, no waste disposal issues and complete mineralization of a wide range of organic pollutants. Therefore, there is a high potential of photocatalysis in the field of renewable energy production and cleaning environment.

This process employs semiconductors as a photocatalyst that plays an important role in redox reactions by using radiation sources, like UV or visible light, in the presence of an oxidant, usually air or oxygen. The process takes place under ambient temperature and pressure conditions. The effectiveness of the whole process depends on a number of factors but primarily, on the type of semiconductor used (metal oxides like TiO_2, ZnO, BiOX *etc*.) and source of radiation (UV or visible). Due to the specific electronic structure of semiconductors, they are the perfect choice for heterogeneous photocatalysis. They form a complete package in terms of their electronic structure, charge transport characteristics and their light absorption properties. Generally, there are two bands where the electrons can reside: valence band (VB) and conduction band (CB). The VB is made up of completely occupied molecular orbital and is characterized by lower energy whereas the CB consists of

molecular orbital of higher energy. The energy difference between the lowest CB edge and highest VB edge is called *band gap* (E_g) and it varies depending on the type of semiconductor. The position of these bands categorizes the material as conductors, insulators or semiconductors, also represented schematically in **Figure 3**. The energy band theory for electrons is used to study the behavior of crystalline solid (either insulating or conductive). In other words, the difference of energy between the different bands and the distribution of the electrons within defines the properties of a solid. In case of conductors, the valence band is partially or completely filled with electrons and the two bands overlap with each other, thus the electrons can move freely between the two bands allowing conduction, for e.g. in case of metals. In contrast, insulators are characterized by a large energy gap between the two bands and as a result, the valence band is completely filled as the electrons cannot cross the long barrier even if high electric fields are applied. Hence, there is no conduction in case of insulating materials. Semiconductors, on the other hand, have a small band gap between valence and conduction band. When a sufficient amount of energy is given in the form of thermal or light, some electrons move to the empty conduction band and the material acts as a weak conductor or a semiconductor. Therefore, in the ground state all electrons are present in the VB and once sufficient energy (equal to or higher than their band gap) is applied, the electrons jump from the filled lower energy VB to the empty higher energy CB. This movement of electrons results in the formation of vacancy in the VB acting as positively charged species, called holes and is denoted as h_{VB}^{+}. The electrons in the conduction band are denoted as e_{CB}^{-}.

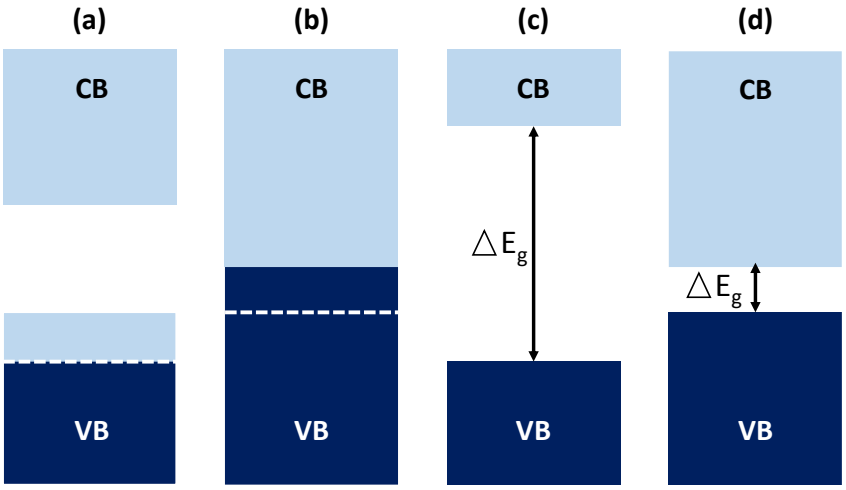

Figure 3. Schematic representation of energy bands for: **(a)** conductors with partially filled valence band (VB); **(b)** conductors with overlapped bands; **(c)** insulators; **(d)** semiconductors.

Mechanism of heterogeneous photocatalysis

The primary step in the photodegradation process is the generation of electron/hole pairs (e^-/h^+) which occurs when the semiconductor photocatalyst is irradiated by light (UV or visible), *see Eq. 1*. When the semiconductor is radiated with light of appropriate energy (equal or higher than its band gap), electrons from VB are excited to the CB generating electron/hole pairs, also called excitons, due to the absorption of photons by the semiconductor. Upon excitation of a semiconductor, multiple scenarios can occur: (a) recombination of electron/hole pairs releasing energy in the form of heat. This process is very common and also, unfavorable for the photocatalytic system as these photogenerated charge carriers (e^-/h^+) could not take part in further redox reactions; (b) trapping of electrons and holes in the metastable surface states; or (c) reaction of these excitons with electron-donor and electron-acceptor species that are adsorbed on the surface of semiconductor resulting in chemical transformation and finally mineralization of the pollutant. At this point, the most important reactions take place: (i) oxidation of water molecules by holes to produce hydroxyl radicals, a very powerful oxidant (ii) reduction of adsorbed oxygen to oxygen radicals (O_2^-), *Eq. 2*. Interestingly, the hydroxyl radicals could be formed in two ways either by the reaction of photogenerated holes with the adsorbed water molecules or by the reaction of these holes with the hydroxyl groups on the surface of the photocatalyst particles, *Eq. 3 & 4*.

$$Photocatalyst \xrightarrow{h\nu} e^-_{CB} + h^+_{VB} \qquad \textit{Eq. 1}$$

$$O_2 + e^- \rightarrow O_2^{\cdot -} \qquad \textit{Eq. 2}$$

$$h^+ + OH^- \rightarrow OH^{\cdot}_{ad} \qquad \textit{Eq. 3}$$

or

$$h^+ + H_2O_{ad} \rightarrow HO^{\cdot}_{ad} + H^+ \qquad \textit{Eq. 4}$$

These superoxide radicals are crucial because they prevent the recombination of holes and electrons. Consequently, more oxygen radicals are available for degrading the contaminants. **Figure 4** shows the photoexcitation process in a semiconductor. The photogenerated electrons transfer to the adsorbed organic species. This transfer of electron process to the semiconductor surface is more efficient if the pollutant is pre-adsorbed on the semiconductor surface [11]. At the surface, the e_{CB}^- reduce the electron acceptor (usually

dissolved oxygen) since they are strongly reducing and h_{VB}^{+}, in turn, can migrate to the surface of semiconductor and combines with the electron from the electron-donor species (pollutant), thereby, oxidizing the pollutant due to their strong oxidizing nature. Simultaneously, recombination can occur either on the surface or in the bulk of semiconductor particle, as shown in **Figure 4**.

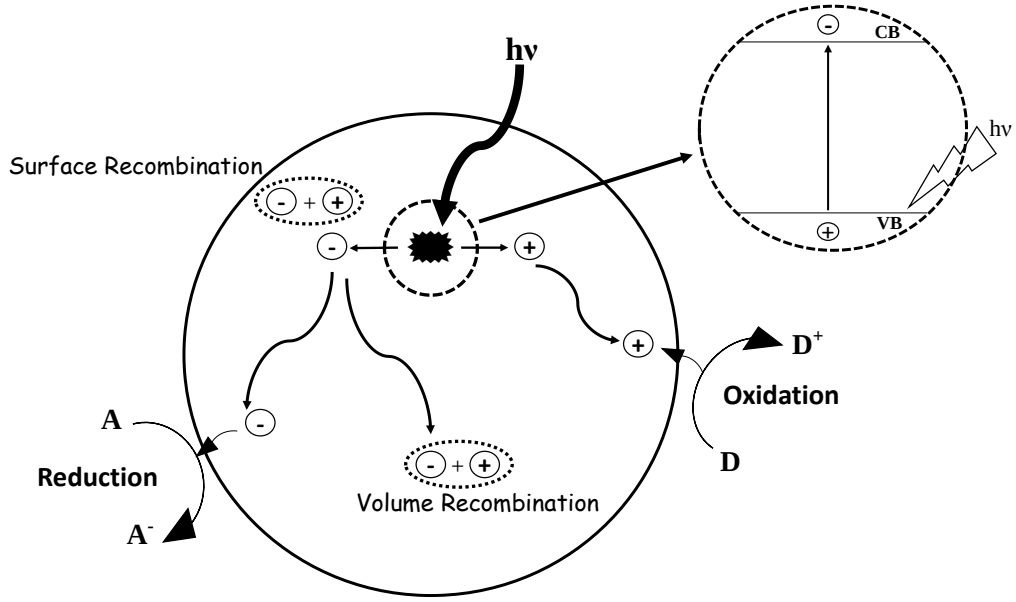

Figure 4. Photoexcitation phenomena in a semiconductor upon irradiation.

The process of photocatalysis could be summarized into the following main steps:

(i) Diffusion of reactants from the external surface of the catalyst
(ii) Adsorption of reactants onto the surface of semiconductor
(iii) Reaction in the adsorbed phase (photocatalytic reactions occurs in this step)
(iv) Desorption of the product(s) from the surface of the semiconductor
(v) Transfer of products to the exterior of the catalyst surface
(vi) Transfer of products from the external surface of the catalyst to the bulk of the fluid

The photocatalytic efficiency for a semiconductor lies in the redox potential of the photogenerated valence band holes and conduction band electrons. The potential of these holes and electrons are defined by the energy of the valence band edge, denoted as E_v, and the energy of conduction band edge, denoted as E_c, respectively. As per thermodynamics concept, E_c must be higher or more negative than the reduction potential of A/A^{-} to be able

to reduce electron-acceptor (O_2). However, E_v needs to be lower or more positive than the oxidation potential of D/D^+ in order to oxidize the electron donor (pollutant).

2.4 Conventional photocatalysts

After Fujishima's pioneer work on TiO_2, photocatalysis became a hot topic in environmental remediation field. Several studies were carried out on the photocatalytic properties of TiO_2. Significant findings were found for the photodegradation of organic pollutants by TiO_2 and slowly the research was extended to other materials as well. Few more semiconductors came into the picture, such as ZnO, ZnS, WO_3, CdS, Fe_2O_3 but most of them are not as efficient as TiO_2. For instance, ZnO has instability and photo corrosion issues [12], photocatalytic efficiency of WO_3 is far too low in comparison to TiO_2 [13], and CdS has similar problems of photocorrosion and low efficiency as ZnO and WO_3. In other words, the photocatalytic activity of these semiconductors did not meet the requirements of practical applications. Therefore, TiO_2 became the most prevalent photocatalyst in the industry till today with the advantage of being chemically inert, (photo) stable, cheap and abundant in nature. However, TiO_2 also has disadvantages such as high recombination rates for electron/hole pairs and wide band gap which is around 3.0 eV that makes it applicable only in the UV region. Considering the solar spectrum that reaches the Earth only 4-5% of the solar spectrum comprises the UV region and the part of visible light radiation is far more abundant (around 42-43%) (**Figure 5**) [14].

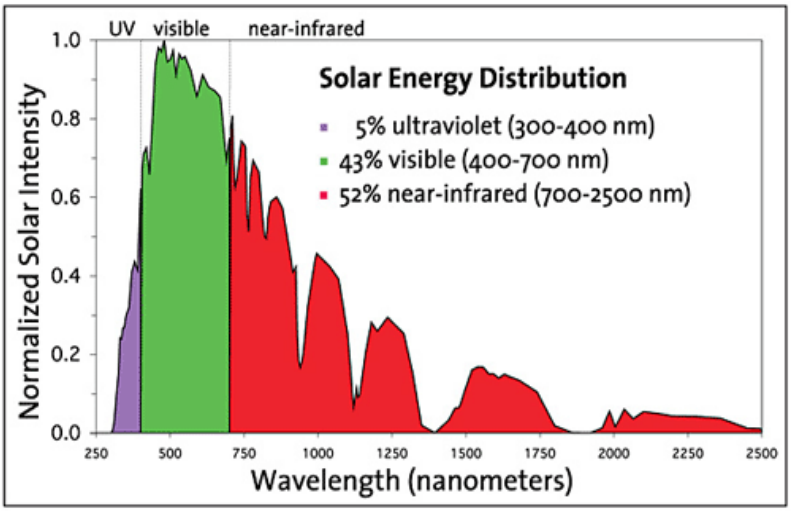

Figure 5. The spectrum of solar radiation. This image has been taken from [14].

This indicates that the process of photocatalysis could be economically feasible if the visible light-driven photocatalysts are developed. For this purpose, several strategies

have been adopted. For instance in the case of TiO_2 to extend its light absorption capacity to visible light. One way is doping with metal or non-metal which has proven to be an effective approach for modifying the wide band gap materials like TiO_2, for *e.g.* C-doped TiO_2, N-doped TiO_2 or Bi-doped TiO_2. In a similar fashion, doping with noble metals like Ag or Au, has also received much attention because of strong absorption of visible light by noble metal nanoparticles which is due to surface plasmon resonance effect. Another widely used strategy to modify the band structure and enhance the light absorbing ability of wide band gap semiconductors is forming composites. Recently, focus is being made on designing some novel photocatalytic materials which are active under visible light. The concept to develop visible light-induced photocatalysts was introduced to enhance the photocatalytic efficiency by widening the light absorption region, maximizing the charge transfer phenomena at the surface, suppressing the recombination process, efficient charge separation and increased surface redox reactions. This results in a photocatalyst with high performance. One such class of visible light driven photocatalyst is the bismuth oxyhalide group (BiOX).

2.5 Visible light-driven photocatalyst: bismuth oxyhalides (BiOXs)

Bismuth oxyhalides are one of a kind. These are layered materials with advantageous features like high chemical stability, excellent optical properties, low cost, nontoxicity, resistance to photocorrosion and easy availability. The layered structure benefits the electron transfer to the photocatalyst surface along the layered network while suppressing the recombination of charge carriers. This is why tremendous research is being carried out nowadays to explore the promising potential of such layered materials in photocatalytic applications. In the past, BiOX was used as thermal induced catalysts, pigments in cosmetic industry [15, 16], gas sensors [17], pharmaceutical industry [18], catalysis [19, 20], phosphors [21] and as ferroelectric materials [22]. Recently, their applications has been extended to environment protection and energy saving areas, including solar water splitting, solar cells, photocatalytic oxidation of heavy metal ions and obnoxious organic pollutants, photo reduction of CO_2, removal of air pollutants (NO_x) [23], N_2 fixation [24], energy storage devices such as lithium-ion batteries and supercapacitors [25, 26], photodynamic therapy [27] and selective oxidation of alcohols [28]. This wide spectrum of possible applications ranging from eliminating toxic organic pollutants to solar water splitting and CO_2 photoreduction is shown in **Figure 6** and it explains why they become popular and widely studied in the areas of developing novel visible light active photocatalysts.

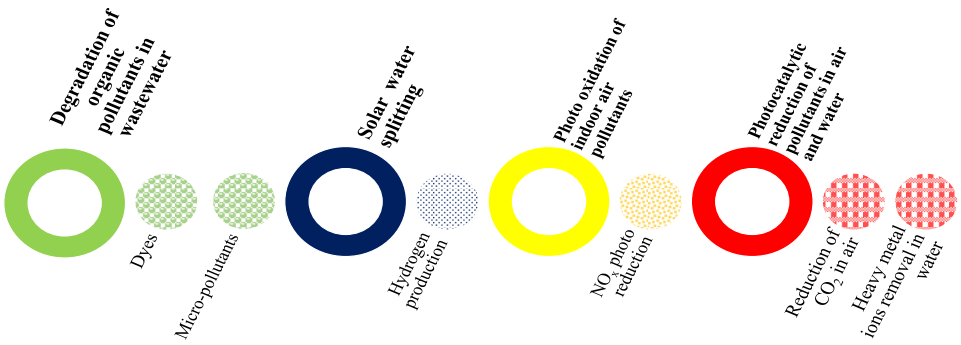

Figure 6. Different applications of BiOX photocatalysts.

2.5.1. Structural properties of BiOX

BiOX are unique, crystalline layer-structured materials. It forms an open-layered assembly which is responsible for its visible light driven photocatalytic activity. In addition to this, their layered structure bestows them with fascinating physicochemical properties as mentioned in the previous paragraph. From a structural point of view, all BiOX crystallizes in a tetragonal matlockite structure where each $[Bi_2O_2]$ slab is interleaved by double slabs of halogen atoms [29]. In this way, each Bi center is surrounded by four oxygens and four halogen atoms resulting in an asymmetric decahedral geometry. The [X-Bi-O-Bi-X] slabs are held together by weak van der Waals interaction. There exists a combination of strong intralayer covalent bonding and weak interlayer van der Waals interaction giving rise to highly anisotropic structural, optical, electrical and mechanical properties. The prime advantage of BiOX is the low recombination rate of electron/hole pairs which is attributed to its open structure and indirect band gap energy. Their structure induces the internal electric field perpendicular to [X-Bi-O-Bi-X] slabs that facilitate the charge separation and migration of photogenerated electron-hole pairs, therefore, suppressing recombination process [30]. The pictorial representation of BiOX crystal structure can be seen in **Figure 7**.

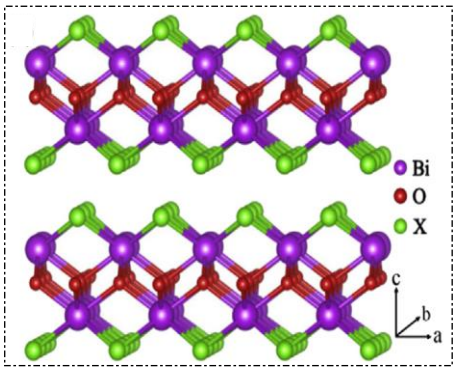

Figure 7. Crystal structure of 2-D layer of BiOX.

2.5.2. Optical properties of BiOX

All BiOX, except BiOF, has an indirect band gap energy and therefore, is known to show photocatalytic response. For indirect band gap semiconductor, the maximum energy of the valence band occurs at a different value of momentum to the conduction band minimum energy while in case of direct band gap, this value is the same [31]. Very few studies have been reported for BiOF as a photocatalyst because of its wide and direct band gap which means it is active only under UV light. In other words, it would not be an economical option if we want to make effective and efficient use of solar radiation. The direct band gap is advantageous for absorption of photon energy while the indirect band gap is favorable for separation of electron/hole pairs and thus, hampering the recombination process of the photogenerated charge carriers [32]. The indirect band gap semiconductor is, therefore, more advantageous than direct band gap one. Some recent studies showed that doping of BiOF with I, Cl or Br or with noble metals has resulted in indirect band gap semiconductors [32, 33].

One of the main factors that is closely related to the photocatalytic activity of a semiconductor is its band gap positions (valence and conduction band). Generally, for metal oxide, the valence band has O 2p orbitals. But what makes BiOX special from other metal oxides is its valence band which is composed of Bi 6s, O 2p and X np orbitals (n = 2, 3, 4 and 5 for F, Cl, Br, I, respectively). Their conduction band has Bi 6p orbitals. The presence of the well-dispersed Bi 6p orbitals together with the O 2p orbital is the main cause of increased mobility of photogenerated charge carriers in BiOX. Simultaneously, the increase in density states of X np orbitals is observed above the valence band edge as we go down from F to I in BiOX which results in narrowing of the band gap value of BiOX [30, 34]. This is why as the halogen's atomic number in BiOX increases, the band gap decreases following the sequence as BiOF > BiOCl > BiOBr > BiOI which, in turn, defines their increasing order of photocatalytic activity in visible region as BiOI> BiOBr> BiOCl> BiOF. The values for their respective band gap are as follows: BiOI has the lowest band gap energy around 1.79-1.92 eV, followed by BiOBr which is around 2.3-2.9 eV, then BiOCl 2.9-3.4 eV and finally, BiOF with wide band gap of 3.5-3.6 eV [35, 36]. As a result, BiOI and BiOBr exhibit visible light photoactivity while BiOCl and BiOF are active under UV radiation. The suitable band structure of BiOX facilitates effective absorption of radiation and initiates further photocatalytic reactions.

2.5.3. Synthesis methods

Generally, the photocatalytic efficiency of several photocatalysts depend on a number of factors, such as type and amount of photocatalyst, illumination source, type and concentration of pollutant used, synthesis method, pH and temperature, *etc*. Studies have shown that the photocatalytic behavior of semiconductor photocatalysts, including BiOX, is largely dependent on their structural, surface and optical properties. But all of it is governed by the type of method used because different methods result in different structural, morphological and optical properties which ultimately lead to differences in photocatalytic response. As per the previously mentioned reports, the main based morphology for BiOX is 2-D nanosheets [37], although recently other types of morphologies were also reported such as 1-D (nanoparticles or nanobelts) [38, 39] or 3-D hierarchical structures (microspheres, microflower-like) [40, 41]. The common source for bismuth includes $Bi(NO_3)_3 \cdot 5H_2O$, $Bi(NO_3)_3$, $NaBiO_3 \cdot 2H_2O$, Bi_2O_3, Bi, $BiCl_3$, and BiI_3 while surfactants like hexadecyl trimethylammoniumchloride (CTAC) and hexadecyltrimethylammoniumbromide (CTAB), halogen acids HX (X = Cl, Br, or I), NaX (X= Cl, Br, or I), KX (X= Cl, Br, or I) and ionic liquids with halogen element served as halogen source in most cases.

By far, liquid-phase synthesis methods are very popular for producing BiOX nanomaterials with the desired functionality. These methods include hydrothermal and solvothermal synthesis, reversed-phase micro-emulsion method, interface-mediated synthesis, sonochemical method, templated synthesis and anion-exchange synthesis. Out of all these, hydrothermal and solvothermal are the most frequently used methods for synthesizing BiOX with different nanostructures. Therefore, in our study, we have used the hydrothermal method for synthesizing our BiOX samples. In hydrothermal and solvothermal methods, a sealed vessel is used to synthesize BiOX nanostructures and it undergoes thermal treatment which in turn creates an auto-generated pressure during heating. This high temperature and pressure conditions could result in BiOX with different morphology and in some cases, non-stoichiometric BiOX [42]. In the case where Bi and halogen sources are dispersed in aqueous media, Bi^{3+} cations tend to react with H_2O molecules to form $(Bi_2O_2)^{2+}$ and H^+ cations in the initial stage [29]. This is a very fast reaction resulting in the formation of several small crystalline nuclei of X-Bi-O-Bi-X, where the interaction between Bi and O atoms is through covalent bond. The positive cations $(Bi_2O_2)^{2+}$ combine with X^- anions *via* coulombic coupling force. The driving force for 2-D structure is the low surface energy of

{001} facet and the layered structure of BiOX that results in [X-Bi-O-Bi-X] slabs. The preparation of BiOX in aqueous solution, however, suffers from a disadvantage which is the fast nucleation rate but this problem is solved if the hydrolysis rate of bismuth precursor is controlled. This is done by adding acids, such as acetic acid to the aqueous solution of bismuth precursor and these acid derivatives, therefore, can inhibit $(Bi_2O_2)^{2+}$ cations formation and be likely to maintain ionic form of bismuth precursors in aqueous solution. Another strategy is to use alcohols, like ethylene glycol, which results in the formation of bismuth-based coordination compounds. In this thesis, we have focused on the synthesis of BiOX in aqueous phase and using acetic acid for bismuth precursor.

The advantage of using this method is that it enhances the solubility of the precursors and initiates the chemical reaction between them which, otherwise, is not possible to occur at ambient conditions. Another significant benefit of this treatment is the improvement in crystallinity of the nanostructures. As shown in several studies, crystallinity is one of the critical parameters that affects the photocatalytic efficiency [43]. For instance, amorphous TiO_2 plays a role as a recombination center while if the crystallinity is improved, the photocatalytic activity is greatly enhanced [44, 45]. Talking about crystallinity, another vital factor comes into the picture which is crystallite size [46]. The crystallite size influences the photoreactivity because it governs many physical properties of the pristine nanoparticles such as surface area, surface energy, lattice distortion and light absorptivity. As a general rule of thumb, the smaller crystallite size means larger surface area, thereby improving the adsorption of reactants and photocatalytic activity. Nevertheless, contradictory results could also be seen in some cases where increase in photocatalytic activity was seen with increase in crystallite size [42, 46].

2.5.4. Influence of synthesis parameters

The above-mentioned methods are not enough alone to obtain novel nanostructures with high efficiency but their controlled synthesis has helped in many ways. For instance, by adjusting some thermodynamic and kinetic parameters of synthesis, BiOX with different characteristics could be obtained. The size, shape, dimensions, crystal facets and phases of the nanostructured BiOX could be controlled by tuning the synthesis conditions, for, *e.g.* reactant concentrations, duration and temperature of the synthesis method. One easy way is to regulate the reaction time and temperature used during hydrothermal or solvothermal processes which would produce a material with desired physicochemical properties.

Optimizing the synthesis method is one of the crucial aspects that requires much attention. The temperature in hydrothermal synthesis is very important because it directs the crystal growth or orientation in a specific direction with changes in hydrothermal crystallization temperature. Another important parameter is time. The duration of hydrothermal heat treatment is also crucial and affects structural properties of the photocatalyst such as average particle size. The pH and reactant concentration are, yet, another important factors that influences the crystal structure but it will not be discussed here. This work dealt with the former two parameters since the impact of these two factors (time and temperature) is more pronounced on the performance of the photocatalyst. For instance, in a study by Adriana *et al*. the effect of different synthesis conditions on the photocatalytic activity of BiOCl was studied [48]. They reported the high removal rate of gallic acid using the synthesized BiOCl at optimal conditions. The physicochemical properties and photocatalytic efficiency of BiOCl was majorly affected by synthesis temperature conditions. This shows how changes in synthesis conditions can have substantial effect on overall performance of the photocatalyst. Also, studying the effect of these synthesis conditions on aspects like crystallization process is essential as it not only gives an idea about changes in optical, morphological or structural behavior of the material but also provides important information on its thermal stability and photocatalytic efficiency. Therefore the knowledge of optimized conditions for the respective material is an added advantage. This will not only save time and unnecessary workload but also will be economical from the industrial point of view. There have been several studies which have focused on the aspect of impact of synthesis conditions on BiOX. For example, the effect of solvothermal synthesis conditions (temperature and time) on morphology and crystallinity of BiOX and the significant effect on their photocatalytic efficiency as studied by Bardos *et al* [49]. In this study, the author discovered that lower temperatures and shorter durations of the crystallization process resulted in more active BiOX photocatalysts while, in contrast, presence of metallic Bi was observed in larger amounts in the opposite case. This suggests that BiOX with preferred structural orientation, crystallinity, morphology, surface or optical properties can be attained by using suitable concoction of synthesis conditions [50].

Based on these works, it can be said that by applying different parameters, a photocatalyst with completely different physical and chemical behaviors and thus, totally different photocatalytic response can be obtained. In the subsequent section, we will briefly discuss each member of the BiOX family and their photocatalytic applications. The previous

studies have shown some correlations between synthesis methods, photocatalytic efficiency and physicochemical properties of the photocatalysts. However, the detailed study on this subject has not been discussed so far.

2.6 Bismuth oxychloride and its photocatalytic activity

BiOCl is considered among novel and promising candidates in the field of photocatalysis. It is a white-colored semiconductor and was the first among other BiOXs to be studied for its photocatalytic properties in 2006 by Zhang *et al* [51]. Since then it has received much attention. BiOCl has a wide band gap (~3.2-3.5 eV) which is quite close to the classically-known photocatalyst, TiO_2 (E_g: ~3.0-3.2 eV), therefore, it is UV active [51, 41]. The dye-sensitized BiOCl have also shown good response under visible light for the photodegradation of dyes and in air remediation applications [52, 53]. Apart from this, BiOCl, in general, also covers a broad spectrum of applications in the areas of photocatalytic energy conversion and environmental remediation, such as hydrogen production by solar water splitting, indoor-gas purification, photocatalytic wastewater treatment, photodegradation of volatile organic compounds (VOC) and nitrogen fixation to ammonia [54, 55]. BiOCl has also shown superior performance for the photodegradation of pollutants like methyl orange, methylene blue and phenol under UV light irradiation [56, 57]. BiOCl has been synthesized in well-defined nanostructures that has an impact on its overall photocatalytic performance. Different morphologies of BiOCl have been reported such as cotton-like BiOCl nanostructures [58], hollow BiOCl microspheres [59], porous nanocubes BiOCl [60], hexagonal prism shaped BiOCl [61], BiOCl nanosheets [62]. It is known for forming oxygen vacancies under oxygen deficient UV or thermal conditions during photocatalysis due to low bond energy and long bond of Bi-O, unlike other metal oxides. BiOCl alone would not serve the role of an efficient photocatalyst at industrial level. In addition to this, there are two main drawbacks of BiOCl that need to be addressed. Firstly, it's wider band gap energy that limits its application under visible light and secondly, synthesizing this material through environmentally friendly routes. Thus, exploring new strategies to optimize its photocatalytic activity remains a necessity.

2.7 Bismuth oxyiodide and its photocatalytic activity

BiOI has a narrow band gap of ~1.8-1.92 eV. Theoretically speaking, BiOI can absorb visible light of the solar spectrum much better than BiOBr and BiOCl due to its narrow band gap energy and hence, it can show higher photocatalytic activity than the other two under

visible light [63, 64]. As a result of this, the recombination rate is also higher in the case of BiOI as compared to the other two BiOXs. However, BiOI is one of the most extensively studied among other two BiOXs (X= Cl and Br) because of its visible light photocatalytic activity due to its narrowest band gap. It is even anticipated that the thermal treatment of BiOI leads to the generation of other forms of bismuth oxyiodides, mainly the iodide-deficient BiOIs, ($Bi_4O_5I_2$, Bi_5O_7I, and $Bi_7O_9I_3$) that have also been reported as a photocatalytic material in the majority of the cases [64-66]. The thermal treatment of BiOI, unlike other bismuth oxyhalides, results in deficiency of iodine atoms, possibly, due to easy loss of iodine atoms and subsequently, producing iodide-deficient BiOI. In some cases, these bismuth oxoiodides and its composites were reported to have higher photoactivity than pristine BiOI [67]. Some of the important applications reported for BiOIs include photocatalysis, photovoltaic applications [68, 69], photoelectrochemical devices [70], H_2 production [71], CO_2 reduction [72], X-ray detectors [73], antifouling [74]. Recently, another significant application of BiOI included organic synthesis *via* greener and environmental-friendly way. The study by Varga *et al.* shows a great diversity in the characteristics of BiOI [75]. This work reported the use of BiOI as an efficient and selective catalyst for Ullmann-type CN-coupling reactions with excellent recycling ability of the catalyst under mild operating conditions. It has also been reported in thermoelectric devices and in fabricating low-cost solar cells [75, 76]. A study on photocatalytic reduction of CO_2 to CH_4 by flower-like BiOI and electrochemical hydrogen storage by hierarchical BiOI were also investigated [77, 78]. This shows that BiOI is also another promising candidate not only among visible-light driven photocatalysts but in non-photocatalytic applications. This shows the diversity of BiOIs. Despite having a narrow band gap, BiOI also suffers from drawbacks such as phase transformations under heat treatment, intrinsic rapid recombination of photogenerated charge carriers and their low oxidation and reduction ability. This affects the overall photocatalytic activity of BiOI which unfortunately limits its applications for industrial use. If the lifetime of these charge carriers is prolonged, the photoactivity of BiOI could be improved. This could not be possible in single component BiOI, therefore, its modification is necessary.

2.8 Bismuth oxybromide and its photocatalytic activity

Bismuth oxybromide (BiOBr) is known to show visible light photocatalytic activity [80]. This could be attributed to its reasonable band gap energy (~ 2.5-2.9 eV) because the band gap directly affects the light absorbing characteristics and charge carrier generation in a

photocatalyst. BiOBr is also known for its high photocorrosion stability, good chemical stability, non-toxicity, and the low probability of charge carrier recombination [81]. The promising results for the removal of toxic dyes by BiOBr under visible light illumination has been widely reported, such as photodegradation of dyes like methyl orange, rhodamine B, methylene blue, orange II [82, 83]. These studies show their huge potential in the applications of wastewater treatment. The ability of BiOBr to degrade recalcitrant pollutants were also seen for other classes of contaminants, such as microorganisms like microcystins [84], Escherichia coli (*E. coli*) and Staphylococcus aureus (*S. aureus*) [85], anitbiotics like tetracycline and norfloxacin [86, 87], pesticides and phenols and phenolic compounds [88]. In addition to this, recently a study by Tang *et al.* reports the photodegradation of glyphosate by BiOBr in combination with a metal sulfide [89]. Apart from this, BiOBr nanoparticles were also studied for the photocatalytic reduction of CO_2 to CO and NO_x removal [89, 90]. All of these studies indicate that BiOBr has the potential to be applied to a wider scale of applications. Just like any other semiconductor photocatalyst, BiOBr has been reported in different types of morphology, ranging from micro to nanostructures like nanobelts, nanoplates, nanoparticles, nanotubes, microsheets. The researchers have also explored 3-D hierarchical structures of BiOBr in order to further extend its photocatalytic applications and these have shown superior performance over low-dimensional structures in many cases. For instance, in one study removal of highly toxic Cr(VI) from water could be obtained *via* BiOBr microspheres [92]. Despite these high performances, the overall photocatalytic efficiency of BiOBr is still not high enough for large-scale practical applications. This is why modifications concerning industrial use are being carried out by the researchers to tackle the problems.

Although studies have shown high potential of BiOX materials in the areas of environmental management and energy conversion, their weak reduction power and relatively positive CB position is unable to meet the demands in such fields. From the industrial perspective, their photocatalytic efficiency is still too low under solar radiation which limits its practical applications. To enhance the photocatalytic activity of BiOX materials under sunlight, several strategies have been adopted in order to tune their band gap energy position, promote charge separation and transportation, and boost the sunlight harvesting. Some of these include facet and morphology-control, defect control, micro-structure alteration, heterojunction formation and composites with carbonaceous materials. Among these, the composite formation is one of the most popular ways to enhance their

light absorption properties. The subsequent section deals with the discussion on the composites of BiOX with carbonaceous materials with the prime focus on one class of carbon nanostructure which is carbon nanotubes (CNT) and its role in photocatalysis.

2.9 Carbon nanostructures in photocatalysis

Carbon-based composites have played a major role in designing and synthesizing novel photocatalysts. This is because of their advantageous characteristics like high surface area, good electron conductivity, chemical inertness, excellent mechanical strength, tunable structural and electrical properties and facile synthesis routes. Different carbon nanostructures have been developed so far and have diverse fields of applications from electronic and semiconductor industry to next-generation advanced materials [92, 93]. For instance, use of carbon nanosheets as electrode material in energy storage devices [94, 95]. Some of the most commonly and widely used carbon nanostructures in photocatalysis include activated carbon, carbon nanotubes, graphene (or reduced graphene oxide) and g-C_3N_4. In the following section, general characteristics of these nanostructures are discussed.

2.9.1. Advantageous features and different roles

Carbonaceous materials, presently, dominate a range of research areas in water purification and play a significant role in the field of photocatalysis, particularly as composite materials [96]. Owing to their extraordinary electrical and structural properties, besides their conductive nature, suppressing the recombination process is, yet, another benefit that can be attained that would further boost the photocatalytic activity. Conductive carbon-based materials are well-known from ages for their high surface area, porous structure, high adsorption capacity, excellent electrical and thermal conductivity and extremely high mechanical strength [97]. The increasing popularity of these materials is also due to their chemical inertness, environmentally benign nature, thermal stability, low cost as compared to other commercial polymeric agents, and their easy availability. For example, activated carbon is a very good adsorbent used for pollutant removal and can be obtained easily from waste material, such as the pyrolysis of any kind of nut shells [98]. Another significant feature of carbon is that it can be doped easily with a variety of metal oxide nanoparticles and therefore, is regarded as a promising material in photodegradation of organic pollutants [99]. Additionally, their stability under acidic and basic conditions and easy recovery of metals is another interesting property. Several authors have reported improvement in photocatalytic efficiency by forming semiconductor composites with carbon-based

materials. This enhanced photocatalytic activity is attributed to their high adsorption ability, enhanced absorption of visible light and easy separation of photogenerated charge carriers. The introduction of carbon nanostructures can have significant impact on a photocatalyst such as preventing the agglomeration of particles and enhancing their dispersion besides the reduction in recombination rate and high adsorption capacity [99, 100]. In most cases, it leads to higher surface area which means more number of active sites on the photocatalyst surface and thus high photocatalytic activity. The different roles played by carbon nanostructures in a semiconductor-carbon composite system are listed below:

- as a support material for metal oxide nanoparticles
- as an adsorbent due to its high adsorption capacity towards pollutants
- as an electron acceptor and transport channel due to its high electrical conductivity
- as a co-catalyst
- as a photosensitizer
- as a structure-directing agent

These carbon nanostructures with different morphologies are promising materials and have diverse field of applications such as photodegradation of toxic pollutants [101,102], CO_2 photoreduction [103], H_2 production [104] and solar water splitting [105]. These nanostructures have an advantage of extending the absorption edge of bare semiconductor photocatalysts into visible region that may lead to the enhancement of photocatalytic response of the composite. The advantageous features of some carbon-nanostructures such as activated carbon, graphene, graphene oxide, graphitic nitride and carbon nanotubes, are briefly discussed in the following section. Below is the schematic representation of those carbon-nanostructures, *see* **Figure 8**.

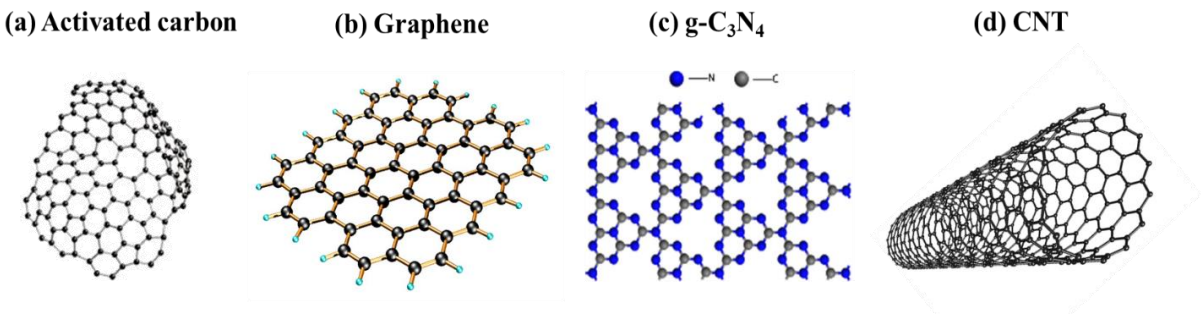

Figure 8. Structures of different types of carbon nanomaterials.

2.9.2. Types of carbon nanostructures

2.9.2.1. Activated Carbon (AC)

Activated carbon is a highly porous adsorbent material and to date has been extensively utilized in several water purification devices [106]. Its adsorptive properties are well-recognized and extensively studied for many years. The classical elemental composition could be denoted as 80% carbon and the rest of it includes oxygen and nitrogen as the remaining materials resulting from the activation process. It can be prepared from pyrolysis and chemical treatment of some organic materials like wood, bamboo or nut shells. The treatment at high temperature creates a porous network within the material. This porous structure imparts high surface area to activated carbon and thus, excess binding sites are available for adsorbate to interact with it. Interestingly, its adsorption capacity towards different adsorbates (inorganic or organic) is dependent on physical and chemical properties of AC. However, its adsorptive property alone would not be sufficient if the main application involves mineralization of organic pollutants because the removal of pollutants using AC is primarily based on surface adsorption. Therefore, the studies on composites of semiconductor photocatalysts with AC are carried out to exploit the benefits of each of these materials.

2.9.2.2. Graphene and reduced-Graphene oxide (r-GO)

Graphene is a two-dimensional carbon allotrope. It has seen a tremendous increase in its applications like water purification after gaining popularity from the electronics industry owing to its excellent electrical conductivity and thermal resistance properties. Currently, the research on developing the next-generation level of circuitry, batteries and solar cells are in progress. Although the study on it goes back to 1859, the wide-scale research started after its isolation in 2004, especially in academic interest. Graphene, structurally speaking, is composed of sheets of carbon atoms arranged in a hexagonal or honeycomb fashion. Many sheets piled on top of each other forming multilayer graphene and at some point this results into graphite which is commonly used as pencil tips. Its combination with a semiconductor has resulted in a composite structure with a great tendency to eliminate contaminants due to its conjugate structure that provides a pathway for the transfer of charge carriers. Additionally, the pronounced adsorption of pollutants on its surface is another beneficial point that accelerates the photodegradation mechanism of adsorbed pollutants. Liang *et al.* reported the first study on photocatalytic CO_2 reduction by

carbon-titania composite system [107]. Since then, it is greatly studied, particularly from the aspect of CO_2 photoreduction. Their large specific surface area and high chemical stability is known to play a significant role in enhancing the photocatalytic efficiency for CO_2 reduction. Further, the idea of using hollow and mesoporous nanostructures together with graphene have also been reported. It offered promising results in many cases reporting enhanced photocatalytic activity due to high surface area and high number of active sites. This leads to enhanced diffusion and adsorption of reactant molecules [108]. Another sub-class of graphene is formed by reducing graphene oxide in various reductive conditions. It has also received much attention due to its high surface area and several oxygen functionalities present on its surface that makes it suitable as an excellent support and electron acceptor [109]. It has similar properties as that of graphene. Due to the oxidation of graphite, several functional groups containing oxygen are introduced on its surface that makes them hydrophilic in nature. As a result of this, it is easily mixed in water and therefore, has much higher exposed area in aqueous solution. This has an added advantage in solar water splitting applications.

2.9.2.3. Graphitic carbon nitrides (g-C_3N_4)

g-C_3N_4 has been extensively used in photocatalysis and is sometimes referred to as "metal-free visible light photocatalyst" [110]. The electronic properties differ markedly from graphene. It exists in seven different phases, out of which, only polymeric graphitic-C_3N_4 is the most stable with highly ordered polymeric structure with pendant amino groups and tri-s-triazine (C_6N_7) as the building structural units. It has a narrow band gap of 2.7 eV, which is appropriate for excitation under visible light while graphene is a conductor with zero band gap and excellent conductivity properties. Due to its high reduction ability, it has shown many effective results in photoreduction for H_2 production and CO_2 reduction. The unique surface properties of g-C_3N_4 makes it perfect as a support material for other photocatalysts [111] or as a photosentisizer in other cases [112]. Besides its rich surface characteristics, g-C_3N_4 offers other beneficial features such as high specific surface area, good chemical stability even under harsh acidic conditions, good light absorption properties, and low-cost for photocatalytic CO_2 reduction [112, 113].

From the above examples, it is clear that these carbonaceous materials have ever-growing possibilities in the field of environmental remediation. The next class of carbon nanostructures is carbon nanotubes (CNT). Because the main topic of my dissertation

involves composites of BiOX with CNT so from this point, the further discussions will be focused on carbon nanotubes, their special characteristics and its composites with bismuth oxyhalides for heterogeneous photocatalysis.

2.9.2.4. Carbon Nanotubes (CNTs)

Initially, CNTs were a popular choice in nano-electronics and optical industries. After gaining much attention from the electronics industry, scientists began to explore more applications where CNTs could be used and in the beginning of the 21st century, CNTs were used in pharmaceutical and medical research for drug delivery [115]. Researchers have reported improvement in photocatalytic activity of semiconductors owing to its excellent electronic and adsorption properties. CNTs form one of the most promising candidates as dopants for a wide class of photocatalysts by virtue of their porous structure, large surface area, high mechanical and thermal stability, good electrical properties and high aspect ratio. Apart from this, CNT offers high mobility of charge carriers in a composite system and acts as a support for metal oxide nanoparticles [93]. The role of CNT as a catalyst support would prevent the aggregation of photocatalyst nanoparticles. In this way, a high rate of ion transport is possible due to their remarkable conducting properties which means efficient separation of electron/hole pairs. The prime advantage of employing CNTs in a photocatalyst is the trapping of electrons transferred from metal oxides resulting in stabilization of charge separation and thus, hindering the recombination process.

CNTs are grouped into two categories, namely, single-walled CNT (SWCNT) and multi-walled CNT (MWCNT). SWCNT consists of only a layer of graphene sheet while MWCNT is composed of multiple concentric layers of graphene. From the past, numerous research and efforts were put into increasing the photocatalytic activity of the semiconductor material by incorporating CNT. A major portion of these studies are concerned with TiO_2. In many studies, visible-light response was seen in TiO_2/CNT-based composite due to the beneficial properties of CNT, also reported by some authors as a temporary electron reservoir [116]. MWCNT, during the photocatalysis process, could also act as a photosensitizer [117]. A majority of studies have reported that there exists a synergistic effect between CNT and semiconductor that is responsible for the enhancement of the overall efficiency of the photocatalytic process. These composites were not just restricted to degradation of pollutants rather find its application in other areas of energy conservation such as hydrogen evolution, dye-sensitized solar cells, photoreduction of CO_2 and sensor

devices. The authors have summarized the reasons for visible light activity of TiO_2/CNT composites because of their high surface area, suppression of recombination of charge carriers and availability of high quality active sites by CNTs. Moreover, in some cases, CNTs have also provided greater control over morphology and different forms of structures for TiO_2/CNT hybrid composite systems. CNTs in photocatalysis have been tested for various pollutants by forming composite structures with a variety of semiconductors like TiO_2, ZnO, WO_3, $BiVO_4$, Bi_2WO_6 *etc*. [117, 118]. One of the important parameters to consider regarding CNT usage as a composite material is its optimum dosage because high content of CNT results in reduction of reaction rate due to light scattering. In a study by Wand *et al.,* high adsorption of pollutants on photocatalyst surface occurred when CNTs amount was controlled which favored the photodegradation process. However, in another study, Réti *et al.* observed that increased MWCNT amount deteriorates the activity due to light absorbing properties of MWCNT and their shadowing effect [119, 120]. This study revealed that low amounts of MWCNT prove to be beneficial for obtaining higher photocatalytic efficiency. Some regarded MWCNT as "conductive wires" that is responsible for transferring and storing electrons and increasing the lifetime of these charge carriers. Furthermore, the incorporation of CNT, in some cases, has led to inhibition of photocorrosion of the photocatalysts, *e.g*, CdS [121].

Recently, CNTs have a broader range of applications including photocatalysis by undergoing functionalization or attachment of certain functional groups to its surface [122]. These functionalized CNT-based composite materials have played a substantial role as enhanced adsorbents in wastewater treatments. Another interesting possible application for CNT has been postulated in water filtration as nano-membrane filters for over a decade [123]. The idea behind is to provide an alternative to polymeric membranes for desalination as CNT materials could offer improved water permeability and reduced size. This shows the diversity and versatility of CNTs applications. Bounded by the limited space, the dissertation talks only about CNT-based BiOX composites. However, I have carried out study with *Activated Carbon*, the other carbon-based nanomaterial, for which a manuscript is in preparation but is not included in the current thesis.

2.10 Composites of BiOX with CNT and its photocatalytic applications

Carbon materials, as discussed in the previous section, are known to improve the dispersion and increase the surface active sites on *semiconductor-carbon interface*. When CNTs are used in a composite form, the nanotubes and the metal oxide are in close contact that forms

a barrier junction which prevents the recombination process by transferring the electrons to the nanotubes. CNTs, therefore, promote interfacial electron transfer process and act as a photo-generated electron acceptor and the semiconductor becomes an electron donor under irradiation [122]. The electrons react with the adsorbed oxygen molecules on the carbon nanotubes generating reactive superoxide anion (O_2^-) which further oxidizes the target pollutant. Oppositely, the holes (h^+) oxidize hydroxyl groups forming hydroxyl radicals that result in decomposition of the pollutant. Yin *et al.* reported that in the composite of BiOCl/MWCNT, the transfer of electrons was promoted by the introduction of MWCNT and suppressed the recombination of electrons and holes. Another significant observation was the structural stability of MWCNT even after being embedded into BiOCl crystal structure [124]. In another work, BiOI/MWCNT composite was synthesized and showed enhanced photocatalytic activity for the removal of Acid Orange II (AOII) dye. The enhanced photocatalytic activity was attributed to the efficient transfer of electrons between BiOI and MWCNT. The composite also demonstrated high adsorption for AOII dye *via* π-π interaction between MWCNT surface and AOII [125]. Further, novel work reported by Weng *et al.* to form a composite of BiOX-carbon nanofiber (CF)/CNT [126]. This type of hierarchical structure where there is a combination of *"semiconductor-substrate"* was designed to maximize the possible recycling of nanosheets from aqueous solution after a photocatalytic process [127]. Furthermore, there exists a synergistic effect between the semiconductor and carbon, as reported by Guo *et al.* that retards the recombination of photogenerated electron-hole pairs, thereby enhancing the photocatalytic performance [127]. Due to high adsorption capacity for pollutants and excellent mechanical strength of CNT, it is said to tailor the energy gaps of semiconductors through the covalent bonding [126]. In some reports, the effect of carbon nanomaterials on narrowing band gap energy of the composite has also been reported. The work by Shijie Li and coworkers reported excellent photodegradation for RhB (98.3% removal after 60 min), MO (84.2% removal after 180 min.) and 4-chlorophenol (78.3% (after 180 min.) by BiOI/MWCNT composite under visible light [128]. The enhanced photocatalytic performance is attributed to the strong coupling interface between MWCNT and BiOI that promoted the efficient separation of electron-hole pairs. The author reported the following significant findings by the incorporation of MWCNT: (a) higher surface areas of composites than pure BiOI (b) more adsorptive and reactive sites for organic pollutants (c) enhanced visible light absorption of BiOI (d) efficient charge transfer and separation (f) low recombination rate. All of these examples suggest that the strategy of forming "composite" materials proved successful in

many cases and accounted for superior photocatalytic activity as compared to their pristine materials. This is mainly due to the efficient transfer of electrons and suppression of recombination of photogenerated electron-hole pairs which ultimately led to an increase in photocatalytic activity. As seen in the above-mentioned examples, the performance of the photocatalyst/CNT hybrid composite is defined mainly by the interfacial contact between the two. The close contact between BiOX and CNT can improve the interfacial electron transfer and restrain the recombination process. For instance, in a study of Xia *et al.*, MWCNT/BiOBr composites were synthesized using ionic liquid to facilitate the dispersion of MWCNTs, due to which close interfacial contact developed between BiOBr and MWCNT [129]. Based on this, the author explained the enhanced photocatalytic activity of the composites but no explanations were found for decrease in band gap energy. Recently, another study was reported on the synthesis of BiOBr/MWCNT *via* interfacial covalent bonding where the better charge separation was obtained because of this interfacial covalent bond between MWCNT and BiOBr [130].

In the examples given above, only the binary-component composites are discussed and, based on it, a few studies have been reported until now for BiOBr/CNT, BiOI/CNT and BiOCl/CNT composites. However, few more studies could be found if these composites are composed of a third component that may be either another semiconductor or another carbon nanostructure, *etc*. However, if composites of CNT with TiO_2 are considered, a huge pile of studies could be easily found as compared to BiOX/CNT composite-hybrid system where the number still remains fairly low. Also, not much detailed studies have been carried out so far. Importantly, no further detailed analysis, correlations or explanations have been presented by authors on several factors like decrease of band gaps of the composites with the addition of CNT (as mentioned before) and possible explanations on its effect on phenomena like crystallization.

3. Aim of Thesis

The majority of the published works in photocatalysis have shown its strong potential concerning environmental-related issues. However, the big challenges of the classically-known photocatalysts, as discussed, such as large band gap and fast recombination shows that there is still a long way to go when it comes to their applicability in a real-world scenario. The general aim of this work is to determine if BiOX together with a carbon nanostructure could be used as one of the alternatives in future to address these big challenges in the field of photocatalysis by exploring the photocatalytic removal of model pollutants. Our aim is to study deeply the influence of CNTs on photocatalytic activity of BiOX and also study its impact on the structural, morphological and optical properties of BiOX. The work comprises three parts. In this thesis, the order of presenting the results of halogen type from BiOX family follows: BiOCl, BiOI and BiOBr. This is because of the ease of presentation and in terms of challenges faced in the case of each halide.

The first is the **hydrothermal synthesis of BiOX/CNT composites** for their applicability as a photocatalyst in industrial wastewater treatment. The main aim of this work is to study the enhancement of photocatalytic activity of BiOX materials by incorporating CNTs. For this, **different compositions of CNTs** will be used. In this study, a range of sample series will be prepared at **different synthesis conditions** (temperature and time) to evaluate the influence of hydrothermal crystallization conditions on the composite's physico-chemical properties. The reference samples (without CNT) in each case will be used to make relevant comparisons.

As a second step, the prepared samples will be characterized for their **structural, surface, morphological** and **optical properties** using different techniques such as XRD, N_2-adsorption, SEM, and DRS.

Lastly, the prepared photocatalysts will be investigated for their **photocatalytic efficiency** towards model pollutants removal. The present study deals with the photodegradation of **phenol** under **visible and UV** irradiation and in some cases photodegradation of **RhB** under **visible light** irradiation. From these important features like crystallinity, surface area, crystallite size or band gap energy and the photocatalytic performance of BiOX/CNT composites can be identified so as to gain the insight in the functioning of the as-prepared CNT-modified BiOX photocatalysts.

4. Experimental section

4.1 Materials

All the reagents used in this study were of analytical grade and used without further purification. For the synthesis and photocatalytic experiments, ultrapure *Millipore Milli-Q* (MQ) water was used. For the synthesis of BiOX/CNT (X = Cl, Br, I), following reagents were used as precursors: bismuth nitrate pentahydrate (Alfa Aesar, 98.0%, Germany), glacial acetic acid (VWR Chemicals 100%, France), potassium chloride (VWR chemicals, 100%, Belgium), potassium bromide (VWR chemicals, 98.0%, Hungary), potassium iodide (Molar chemicals, 98%, Hungary), functionalized multiwalled carbon nanotubes (Nanothinx S.A., Greece). The model pollutants used in our study included phenol (VWR, analytical grade) and RhB (Alfa Aesar, analytical grade).

4.2 Synthesis of BiOX and BiOX/CNT composites (X= Cl, I, Br)

In this study, BiOX composites with CNT were prepared using hydrothermal synthesis method. For comparison, bare BiOX as reference samples were also synthesised. Based on previous reports in literature, the molar ratio of Bi:X was taken as 1:1. This is because if either excess of bismuth ions are present, it may result in metallic bismuth or the excess of halide ions will remain undissolved at the end of synthesis as an impurity. All of these possibilities could deteriorate the photocatalytic performance of the samples. The following paragraphs explain the detailed synthesis procedure for BiOX and BiOX/CNT composites.

In the synthesis process, two solutions A and B were prepared. The solution A served as bismuth source and solution B as halogen source. For solution A, 3 g $Bi(NO_3)_3 \cdot 5H_2O$ was dissolved in 3 mL glacial acetic acid under continuous magnetic stirring and heated up to 45°C to speed up the mixing process until a clear transparent solution was obtained. After the complete mixing of $Bi(NO_3)_3 \cdot 5H_2O$ in acetic acid, 25 mL deionised water was added under magnetic stirring. In case of composites, the desired amount of CNT (0.5, 1, 2 wt%) was added to this solution and ultra-sonicated for one hour. This was marked as solution A. In case of reference samples (pure BiOX), the step of CNT addition was skipped. Solution B was prepared by mixing the calculated amount of potassium halide in 25 mL deionized water. Solution B was then added dropwise to Solution A under continuous magnetic stirring followed by 20 minutes of homogenization. The colour of the precipitate changed in each case of halogen during the reaction. The mixture was transferred to 120 mL Teflon®-lined stainless-steel autoclave and subjected to heat treatment at a designated temperature for a

designated duration. It was then allowed to cool to room temperature and the product was collected and washed with ethanol and deionized water, three times, each time using centrifugation at 4400 rpm for 5 minutes. The final product was dried at 60-80 ºC in an oven overnight.

The effect of CNT amount and synthesis parameters (temperature and time) on the overall performance of the catalyst was studied. To investigate the impact of time, the samples were heated for 4.5 and 6.5 hours. Simultaneously, the effect of temperature was also studied at 120 ºC and 150 ºC for a period of both 4.5 and 6.5 hours. These temperature and time conditions were chosen based on our preliminary studies which showed that higher temperatures (160°C) led to the formation of metallic bismuth which proved detrimental to the photocatalytic activity in the case of BiOX [49]. The shorter durations were used for this study keeping the economical aspect in mind and evaluating the effect of shorter time on the crystallization process of BiOX materials. For each halide, a fixed percentage of CNT was added (0.5, 1 and 2 wt.% CNT) resulting in BiOX/CNT composite. Since solution B was different in all three cases of halides different coloured precipitates were obtained in each case, as presented in **Table 1**.

Table 1: Different halide sources used and the colour of precipitate obtained in each bismuth oxyhalide.

KX	**Color of precipitate obtained for bare BiOX**	**Color of precipitate obtained for BiOX/CNT composites**
KBr	Off-white	Light-grey to dark grey color with increasing % CNT
KI	Dark brick-red	Dark red to brown color with increasing % CNT
KCl	White	Light-grey to dark grey color with increasing % CNT

4.3 Characterization

The prepared samples were characterised using X-ray diffraction to study the phase compositions and crystal orientations. A *Rigaku Miniflex II* diffractometer, X-Ray Diffraction, with the following measurement conditions was used: 2θ° = 10-80°, λ (Cu Kα) = 0.15406 nm, 40 kV and 30 mA. The primary crystallite size (d) was calculated by using following the well-known Scherrer equation:

$$d = k\lambda \div \beta \cos\theta \qquad Eq.\ 5$$

where, *k* is the shape factor constant, usually in the range of 0.8-1.2 (typically taken value is 0.9, in case of spherical particles or if shape information is unknown), λ is the X-ray wavelength, θ is the bragg angle and β is the peak width at full width at half maximum intensity (FWHM) of the peak in radians, also known as line broadening and can be calculated as $\beta = \beta_s - \beta_0$, where β_s and β_0 are XRD peak half-widths of the sample and of the silicon standard.

Morphological and elemental compositional analysis were carried out using Scanning Electron Microscopy (SEM) with Energy Dispersive X-ray (EDX) spectrometer, *Hitachi S-4700 Type II* SEM. N_2 adsorption-desorption measurements were carried at 77K using a *BELCAT-A* device to measure the specific surface areas of the samples and calculations were done *via* BET (Brunauer-Emmett-Teller) method.

A *Jasco-V650* spectrophotometer with an integration sphere (*ILV-724*) was used for measuring the diffuse reflectance spectra of the samples (λ = 220-800 nm). The indirect band-gap energy was calculated using the Kubelka-Munk equation, that is $[F(R).h\nu]\ p = A(h\nu - E_g)$, where F(R) is the Kubelka-Munk function, h is Planck constant, E_g is the band gap energy, A is constant and p is dependent on the type of optical transition and is obtained by plotting the graph between $(\alpha h\nu)^{1/2}$ vs. photon energy (hν) [131]. In some cases the possible electron transitions were evaluated by plotting the $dR \cdot d\lambda^{-1}$ vs. λ, where R is the reflectance and λ is the wavelength.

Raman spectroscopy was used to study the composite formation and crystal defects in some cases. A multilaser confocal Renishaw in Via Reflex Raman spectrometer equipped with a RenCam CCD detector was employed to record the Raman spectra. The 532 nm (green) laser was applied as an excitation source. Using a 0.9 NA objective of 100× magnification, the Raman spectra were collected. The integration times were 20 seconds,

1800 lines/mm grating for all spectra, and 10% of the maximum laser intensity – laser power was 20 mW. 4 cm^{-1} was the spectral resolution.

The photoluminescence (PL) spectra were acquired on a fluorescence spectrophotometer (JASCO LP-6500 spectrofluorometer) with 1 nm spectral resolution equipped with Xe lamp as the excitation source and coupled to an epifluorescence accessory (EFA 383 module). The measurements were recorded in the wavelength range of 350-800 nm with fixed excitation wavelength at 365 and 450 nm.

4.4 Photocatalytic activity evaluation

The photocatalytic activity of the prepared samples was determined by measuring the degradation of phenol, a colourless pollutant, in aqueous solution under UV and visible light. The prime focus of our study is phenol photodegradation. However, in some cases the photodegradation of a colored pollutant, rhodamine B, under visible light region was also investigated. For the simple reason that phenol is hard to degrade due to the presence of stable benzene ring which makes it further difficult to adsorb on the surface of the semiconductor material. Besides, phenol is known to undergo complex degradation mechanism which involves phenol intermediates. The kinetics of the phenol mineralization probably consists of competitive degradation reactions between phenol and its intermediates. In literature also, not many studies have been reported on phenol photodegradation in comparison to the data available on the dyes photodegradation. Dyes, on the other hand, are known to absorb visible light, therefore, sometimes it is difficult to predict whether the decolorization of the dye is due to actual photocatalytic activity of the semiconductor or it is merely adsorption on the surface of the photocatalyst.

The photocatalytic test was carried out in a double-walled Pyrex® glass reactor, surrounded by a thermostated jacket (T = 25°C) with either water (in case of UV) or sodium nitrate (in case of visible light). The role of sodium nitrate ($NaNO_2$) was to provide wholly visible light to the suspension since $NaNO_2$ has a tendency to absorb UV photons. The four energy saving conventional fluorescence lamps (*Düwi 25920/R7S*, 24W) were used for the visible light measurements and 6 fluorescent tubes (*Vilber-Lourmat T-6L UV-A*, 6W) were used in case of UV light measurements. The suspension containing the pollutant and photocatalyst was continuously purged with air to keep the dissolved oxygen concentration constant during the whole experiment. The following important parameters were adopted for the test: (a) 1.0 $g \cdot L^{-1}$ of prepared samples suspended into the solution, (b) initial

concentration of pollutants (C_0): phenol = 0.1 mM for BiOX (x=Cl, Br, I) and RhB = 0.02mM for BiOI and 0.04 mM in case of BiOCl. For BiOBr, photodegradation study for only phenol was conducted because our main aim was to study the phenol removal. Different concentrations of RhB were used for BOI and BiOCl based on their adsorption equilibrium tests performed. The suspension was sonicated for 5 minutes in both cases of pollutant. Initially, the suspension is kept for desired period of time (listed in **Table 2**), depending on the pollutant, under dark to ensure the establishment of adsorption-desorption equilibrium with continuous stirring and air supply. After this, the suspension was irradiated under visible light and in some cases with UV light, depending on the type of BiOX, for a desired period of time (see **Table 3**) followed by sample collection at regular time intervals. The samples collected were then centrifuged for 3 minutes at 15000 rpm and filtered using Filtratech 0.25 µm syringe filter. The changes in concentration of the model pollutants (phenol and RhB) was measured by HPLC and UV spectrophotometer, respectively. HPLC system of *Hitachi* was used equipped with *Merck-Hitachi L-7100* low-pressure gradient pump and a *Merck-Hitachi L-4250* UV-Vis detector attached to a *Lichrospher R_p 18* column. The mobile phase used for measurements was methanol/water of composition (50:50 v/v) mixture. The detection wavelength ($\lambda_{detection}$) used for phenol was 210 nm. The concentration of Rhodamine B (RhB) was measured by using a JASCO V-650 spectrophotometer with maximum wavelength absorption at 554 nm.

The changes in the concentration of the model pollutants (phenol and RhB) were measured by using the following equation (*Eq. 6*):

$$\%\, deg.efficiency = (100 - \frac{C_f}{C_0}) * 100 \qquad Eq.\ 6$$

where, C_0 and C_f are the initial and final concentrations at t = 0 and t min, respectively.

It is very important to point out here some of the variable parameters that were used. For instance, different concentrations of RhB were selected depending on the halogen type in BiOX based on the results obtained through adsorption studies. The final concentrations chosen were the ones in which less than 15% of adsorption occurred in the absence of light. This way the actual removal by photocatalytic degradation could be obtained. Thereafter, different radiation sources were used depending on BiOX and type of pollutant. For example, BiOBr and BiOI studies were conducted under visible light irradiation for both the pollutants due to their narrow band gap. On the other hand, BiOCl was illuminated with both visible and UV light in the case of both the pollutants. However, for phenol

photodegradation, almost negligible photodegradation took place under visible light due to its wider band gap so our results for phenol removal by BiOCl will be restricted to only UV light irradiation. In the case of RhB, BiOCl reported photocatalytic activity under visible light irradiation. This explains the different parameters used in the case of each halide and the nature of the pollutant. A short summary of it is presented in **Table 2**.

Table 2: Different experimental conditions used for studying the photodegradation of pollutants (phenol and RhB) depending on the pollutant type and BiOX.

Pollutants used	**Concentration (mM)**	**Adsorption/desorption time (min)**	**Irradiation time under visible light (min)**	**Irradiation time under UV light (min)**
Phenol *(BiOX: X= Cl, Br, I)*	0.1	30	240	120
RhB (*for BiOI*)	0.02	60	120	120
RhB *(for BiOCl*)	0.04	60	120	120

5. Results and Discussion

To begin with, the prepared composites of BiOX/CNT are firstly characterized for their structural, morphological and optical properties then followed by the photocatalytic activity investigations. At the end of each section, some important correlations are pointed out with respect to the photodegradation efficiency of the composites to study the factors governing the efficient removal of phenol and RhB.

5.1 BiOCl and its composites with CNT

5.1.1 Characterization of BiOCl and BiOCl/CNT

The crystal structure of pure BiOCl and BiOCl/CNT composites were determined by X-Ray Diffraction (XRD) and the diffractograms of the samples are shown in **Figure 9 (a)** and **(b)**. All the diffraction peaks can be indexed to tetragonal structure of BiOCl (JCPDS 06-0249). The peaks at 12.17°, 24.1°, 25.92°, 32.50°, 33.29°, 36.50°, 40.87°, 46.66°, 49.64°, 55.21°, and 58.60° correspond to the crystal planes of (0 0 1), (0 0 2), (1 0 1), (1 1 0), (1 0 2), (0 0 3), (1 1 2), (2 0 0), (1 1 3), (2 1 1) and (2 1 2). All other samples showed similar diffraction patterns. The characteristic peaks for CNT was absent in all the cases probably due to its low amount and overlapping with the diffraction peak of (101) crystal facet of BiOCl. As it can be seen from **Figure 9 (a)**, the diffractograms of composites are similar to their respective reference samples (pure BiOCl) which indicates that no change in the structure of BiOCl occurred with the introduction of CNTs. However, a little variation in the relative intensity values of the peak profiles can be seen among different sample series. Interestingly, compared to the standard diffraction pattern (JCPDS: 06-0249), the diffraction peak intensity of (102) plane, in all cases, is relatively stronger than the other planes and in some situation, the diffraction peak of (001) was missing, as shown in **Figure 9 (b)**. Additionally, the literature has reported mostly (101) or (110) as the dominant crystallographic planes but in our study, the preferred orientation is along (102) for all the sample series [132]. Higher degree of crystallinity could be seen in case of samples containing CNTs (**Figure 9 (a)**) as reported elsewhere in [133]. From **Figure 9 (a)** and **(b)**, it is evident that a larger portion of amorphous region is present in case of the reference samples (pure BiOCl). Besides CNT amount, higher temperature conditions have also contributed to the high crystallinity of the samples. For instance, at high temperature condition (150°C), the reference samples were also crystalline and the amorphous region

disappeared unlike in the case of 120°C, *see* **Figure 9 (a).** This indicates that the contribution of CNT and hydrothermal crystallization temperature is enhancing the overall crystallinity of the materials.

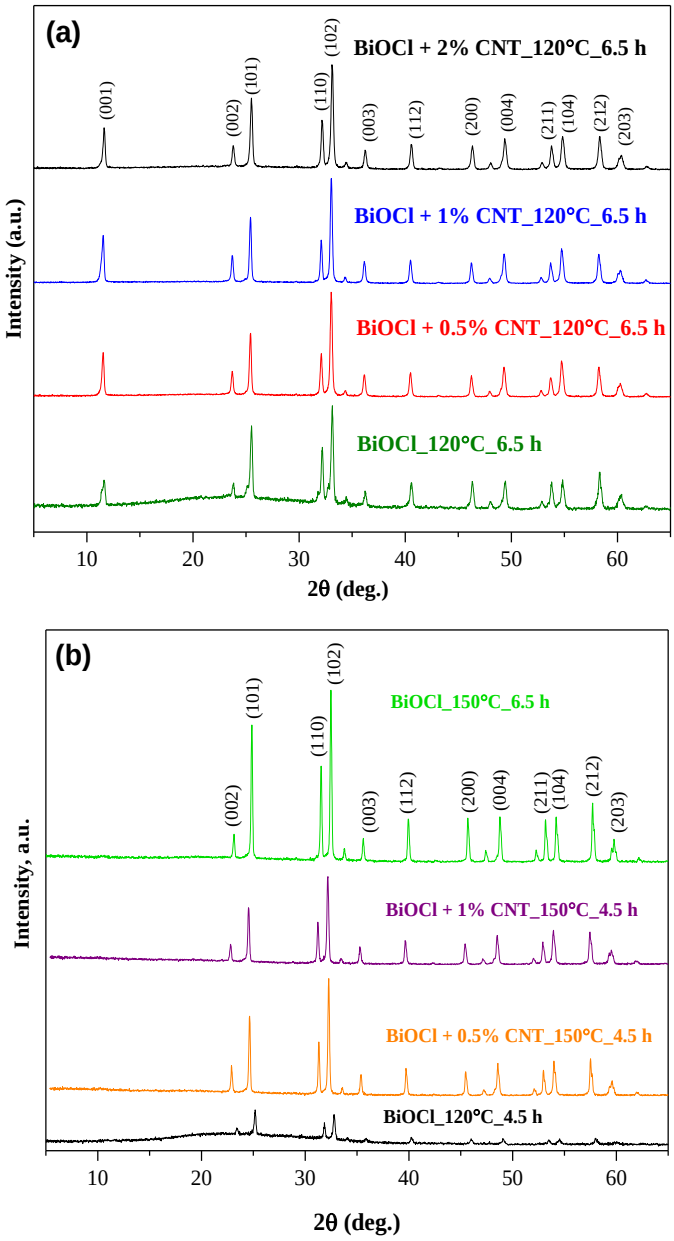

Figure 9. XRD diffraction patterns showing reflections of the investigated BiOCl and BiOCl/CNT samples prepared at **(a)** 120°C and 6.5 h, and **(b)** samples showing absence of (001) crystallographic plane.

The primary crystallite size was also calculated for the samples using the Scherrer equation as discussed in the experimental section. Through the calculations, it was observed that the primary crystallite size of the samples prepared at 120°C were comparatively lower than that of the samples prepared at 150°C (shown in **Appendix 1**). This is a common

phenomenon because generally higher temperature conditions lead to larger crystal formation. At 150°C, a wider variation in crystallite size was observed. For example, the primary crystallite size varied approximately between 40-125 nm in the case of 150°C while those synthesized at 120°C were in between 60-80 nm. Although there is a wider range in the primary crystallite size of the samples at 150°C, but a clear sharp decrease was observed with increasing CNT content which means that CNTs were also affecting the primary crystallite size of the composites beside crystallinity. The range of crystallite size, specific surface areas and band gap energy values of BiOCl and BiOCl/CNT samples is given in **Appendix 1**.

In order to study the influence of CNT and hydrothermal synthesis conditions on morphology, the samples were measured using SEM. BiOCl/CNT composites displayed mostly irregular, non- hierarchical structure of microsheets. All the samples showed similar morphology. **Figure 10 (a-c)** is the representative image concerning BiOCl and BiOCl/CNT samples. **Figure 10 (b)** and **(c)** shows the stacking of these micro-sheets. In addition to this, the surface of those sheets were extremely smooth while no pores could be seen on its surface. It is quite common to see the aggregation of nano/microsheets in the case of BiOX, as in our case, especially when the synthesis involves aqueous media, also discussed previously in [29]. For this reason, some authors have reported the use of ionic liquids during the synthesis to avoid random aggregation of individual nanoplates/sheets [134]. In addition to this, the samples containing CNT, those irregular shaped nanoplates/sheets started to build edges at the corners creating uniform square-like nanoplates, shown in the inset of **Figure 10 (d)**, as the amount of CNT increased. This square-like morphology was also observed in a study by Xiong *et al.* where the author used mannitol as a template-directing agent which resulted in the formation of such square-like BiOCl nanoplates [135]. However, this distribution of square-like nanoplates was, of course, not homogeneous in our case since no template-directing agents were used. Also, these changes were not significantly dependent on synthesis parameters (time and temperature).

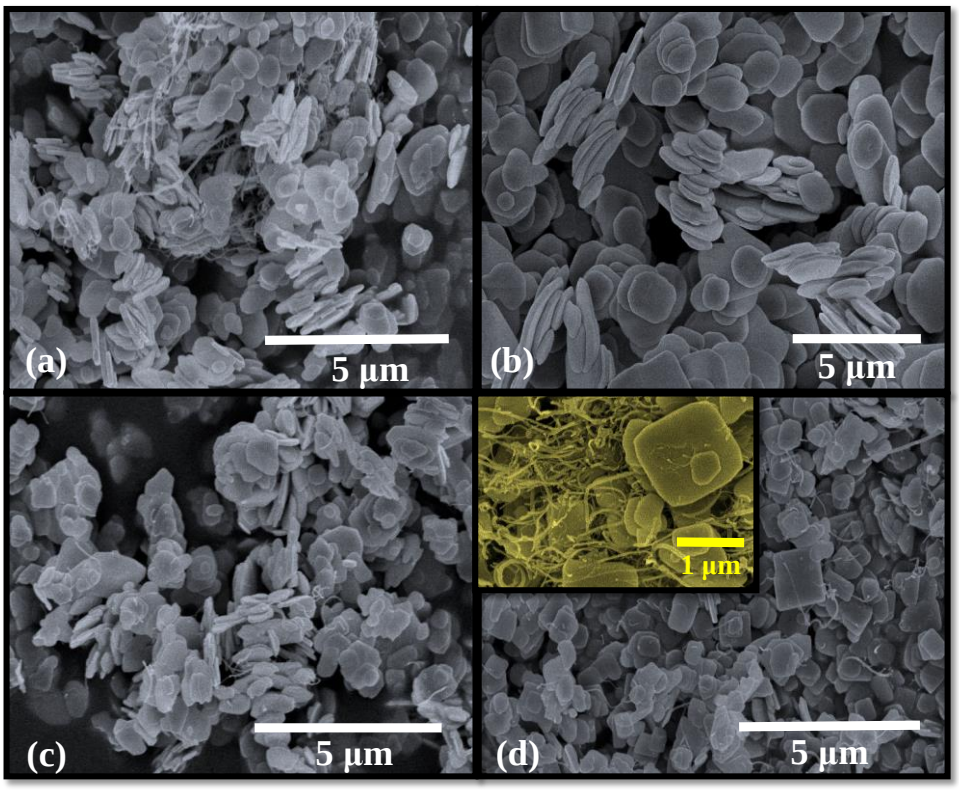

Figure 10. SEM micrographs of the investigated samples showing microsheets-like morphology for samples **(a)** BiOCl + 0.5% CNT prepared at 120°C for 6.5 h, **(b)** BiOCl prepared at 150°C for 4.5 h, **(c)** BiOCl + 0.5% CNT prepared at 120°C for 4.5 h, and **(d)** BiOCl + 2%CNT prepared at 120°C for 4.5 h.

The optical properties of the composites were studied by using diffuse reflectance spectroscopy (DRS). The band gap (E_g) values of BiOCl and BiOCl/CNT composites were calculated using Kubelka-Munk function, as discussed in the experimental section. The range of E_g values for BiOCl and BiOCl/CNT samples fall in between 2.96 and 3.38 eV. **Appendix 1** provides the exact E_g values of all the samples. **Figure 11 (a)** shows the DRS spectra of the composites prepared at 120°C for 6.5 h. The absorption maximum for BiOCl was observed around ~353 nm. This suggests that the samples have strong light absorption in the UV region. Through the first derivative of the DRS spectra, as shown in **Figure 11 (b)**, it was found that the addition of CNT led to blue shift in the absorption edge maxima. Similar blue-shift was also observed in another study of BiOI with increasing CNT amount [125]. This means that the emission and excitation bands are different. Additionally, the composites showed a decrease in the band gap values. In case of reference samples (without CNT), E_g values varied from 3.26 to 3.38 eV while for composites the band gap values fall in a much wider range between 2.96-3.15 eV, depending on the amount of CNT and

synthesis conditions. The decrease in the band gap of composites was also reported in [136]. These identical results could be explained through the previous reports which dealt with the influence of CNT on the optical properties of a photocatalyst. One of them explains the photosensitizer behavior of CNT that is responsible for extending the light absorbing spectrum for photocatalyst [137]. Also, it is assumed that the presence of covalent bonding between the photocatalyst and CNT can even contribute to extended light absorption. We assume that a similar phenomenon of enhanced light absorption occurred in our study after the incorporation of CNT.

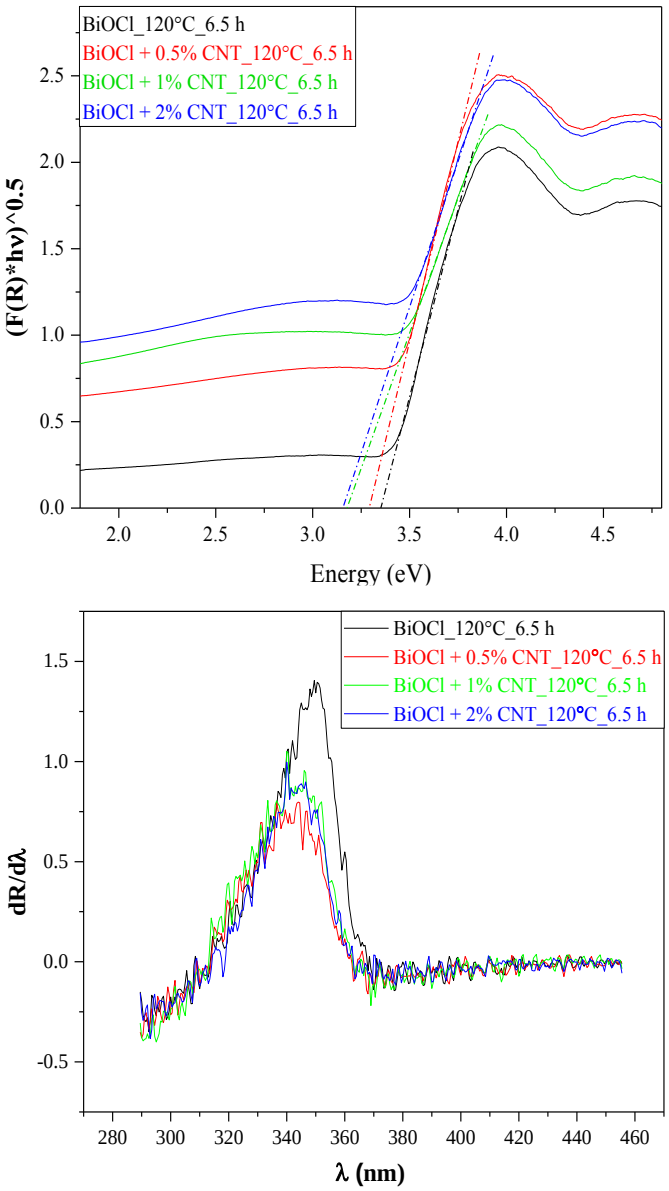

Figure 11. (a) DRS plots of transformed Kubelka-Munk function *versus* the energy of samples prepared at 120°C for 6.5 h showing band gap energy values (E_g) **(b)** first derivative DRS spectrum of the same sample showing blue-shift.

5.1.2 Photocatalytic evaluation of BiOCl and BiOCl/CNT

The photocatalytic efficiency of BiOCl and BiOCl/CNT samples was determined using two model pollutants. The samples were tested for aqueous solution of RhB and phenol, as model pollutants, under visible and UV light, respectively. In the case of RhB, the highest photodegradation efficiency was 98% by pure BiOCl sample prepared at 120°C for 6.5 h and the solution became transparent after 120 min of irradiation. This sample showed the presence of an amorphous region, as evident from XRD, which indicates the role of other factors that are contributing for its higher photocatalytic activity and will be discussed in later sections. Considering the composites prepared at 120°C for 6.5 h, the minimum degradation efficiency of 52% and maximum 88% of RhB removal rates were obtained under visible light irradiation, shown in **Figure 12.** Almost 20% of the dye adsorption took place and the rest of the dye was photo-catalytically removed, *see* **Figure 12**. In spite of the wide band gap of BiOCl, the results from photodegradation experiments showed that it can efficiently degrade RhB under visible light irradiation. This is, apparently, due to the phenomenon called "indirect dye photosensitization" process, where the dye molecule gets excited and transfers the photo excited electron to the conduction band of semiconductor [37, 42]. This could possibly be one of the reasons for higher photocatalytic activity of BiOCl for RhB under visible light.

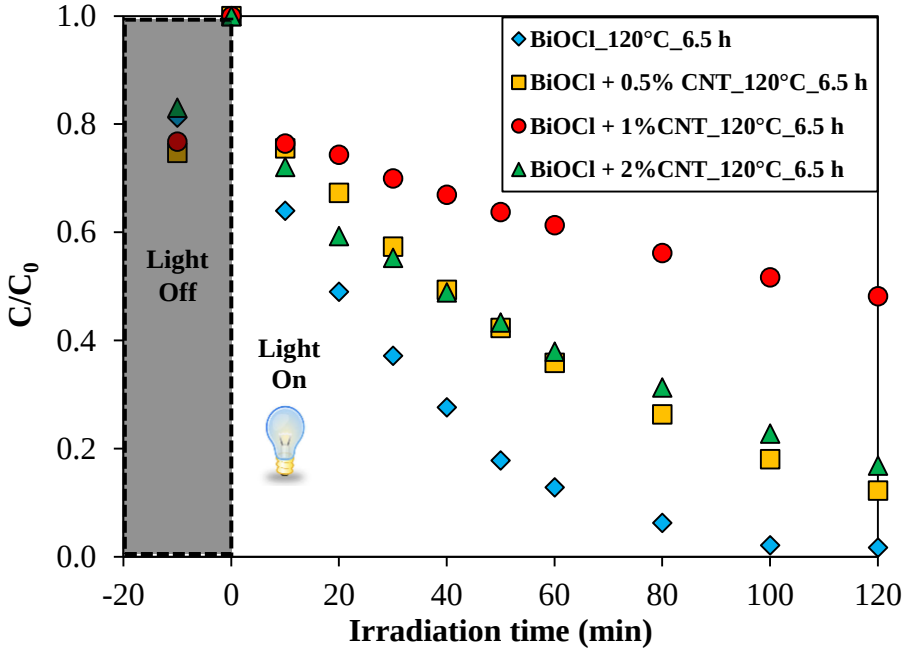

Figure 12. Photocatalytic activity of BiOCl and BiOCl/CNT composites prepared at 120°C for 6.5 h for RhB under visible light irradiation representing higher photodegradation efficiency of pure BiOCl sample.

Among BiOCl/CNT composites, the sample with 0.5% CNT prepared at 120°C for 6.5 h showed the maximum degradation efficiency of 88% for RhB under visible light irradiation in 120 min. For the rest of the samples, the removal efficiency ranged between 60-83%. **Figure 13** shows the different trends observed in the photocatalytic degradation of RhB as a function of CNT amount under visible light. It is clear from **Figure 13** that the composites with 0.5% and 2% CNT show a similar pattern for photodegradation efficiency (% deg.) as a function of CNT amount. However, no specific trend can be seen for 1% CNT and pure BiOCl samples. This suggests that the difference in the photocatalytic activity in the latter case cannot be directly correlated to CNT amount. The difference in the behavior of the samples are explained further through some correlations which will be discussed in the further sections.

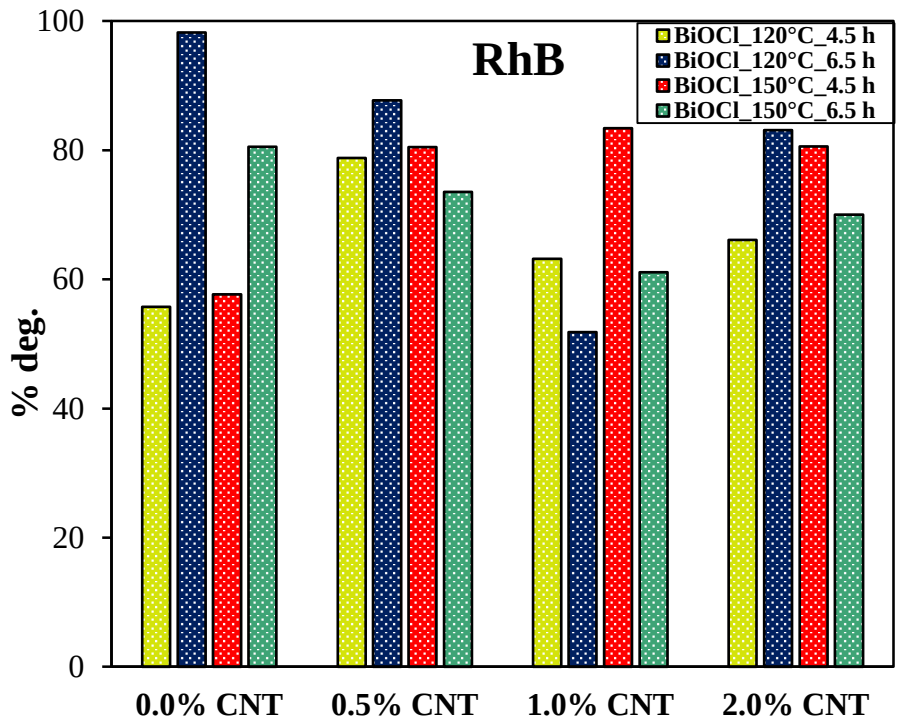

Figure 13. Trend reflecting the degradation efficiency (%) of the investigated BiOCl and BiOCl/CNT samples for RhB under visible light as a function of %CNT.

To better elucidate the photocatalytic efficiency of the composites, the photocatalytic activity was compared by using a colorless pollutant (phenol). Since phenol is colorless, the photosensitization process does not occur. Additionally, phenol is a weakly adsorbing compound on the surface of several catalysts [138]. Due to the wide band gap of BiOCl, no photocatalytic activity was observed for phenol under visible light. The degradation efficiency of the samples fall in the range between 30-45% under UV-A irradiation. It is

important to note here that ordinary lamps were used in this study, therefore, such values are promising in the areas of removal of recalcitrant pollutants like phenol. The samples prepared at higher temperature and under longer heat treatment conditions (150°C for 6.5 h) showed the maximum removal efficiency for phenol under UV light. **Figure 14** shows the concentration changes in phenol over time for the samples prepared at 150°C for 6.5 h with different CNT content. Similar to the RhB case, the photodegradation efficiency of BiOCl and BiOCl/CNT samples for phenol was also compared as a function of CNT amount and hydrothermal crystallization conditions, shown in **Figure 15**. It was observed that all the compositions of CNT, except for 1% CNT, showed a similar increasing trend which means that the rise in hydrothermal crystallization conditions (time and temperature) proved to be beneficial for phenol photodegradation. The composition with 1% CNT again did not show any specific trend and showed lower photocatalytic activity. When the amount of CNT was high (2%), the photocatalytic activity was also high under UV light. Even lower CNT amounts (0 or 0.5%) resulted in higher photodegradation efficiency in some cases. Therefore, the next step was to verify if there were any correlations or some connections between the photocatalytic activity and physico-chemical properties of the composites, like structural and optical properties.

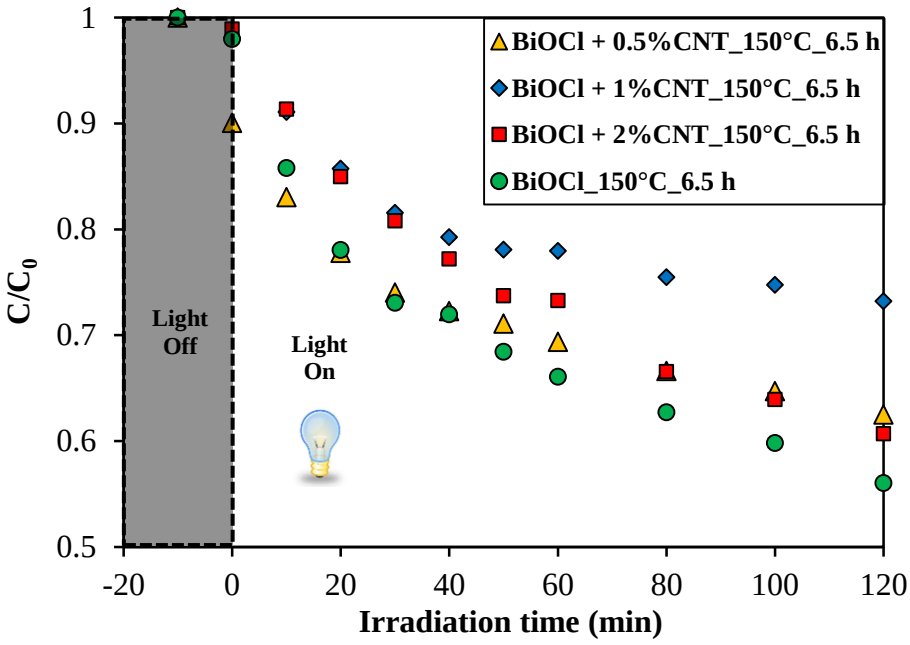

Figure 14. Photocatalytic activity of BiOCl and BiOCl/CNT composites prepared at 120°C for 6.5 h for phenol under UV-A irradiation representing higher photodegradation efficiency of pure BiOCl sample.

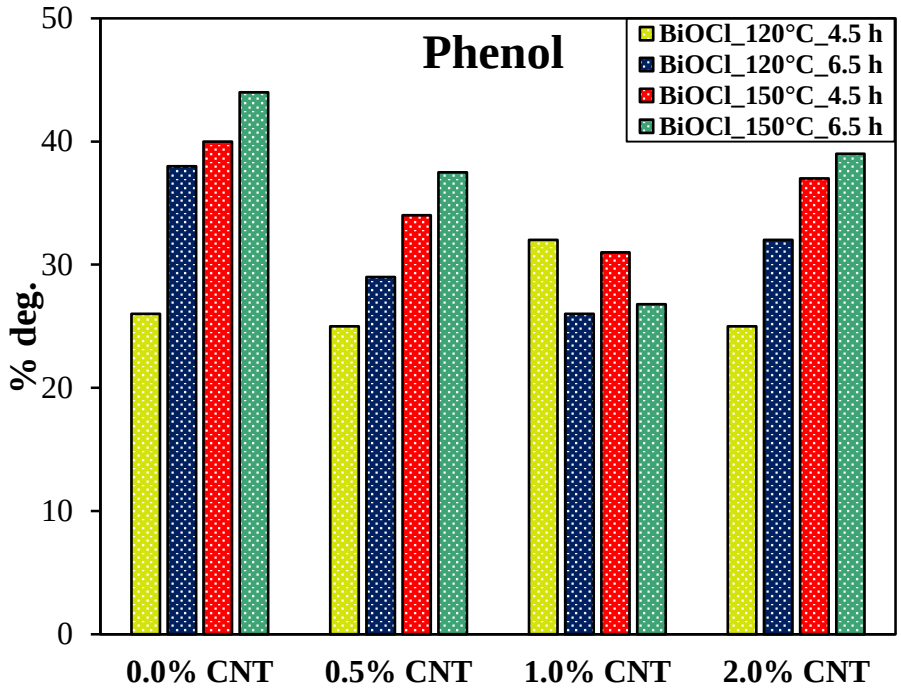

Figure 15. Different trends reflecting the degradation efficiency (%) as a function of % CNT of the investigated BiOCl and BiOCl/CNT samples for phenol under UV-A light irradiation.

Role of CNT and crystallization conditions on photocatalytic activity of BiOCl

From **Figure 13**, some interesting observations were found with respect to the amount of CNT and hydrothermal crystallization conditions (time and temperature). As can be seen from **Figure 13**, in the case of reference samples (0% CNT) when the crystallization time is short (4.5 h), it is presumed that the process of crystallization did not complete and hence, not sufficient time was given for the crystal to grow which could be favorable for achieving higher photocatalytic performance. As a result, some amorphous regions are still present with low crystallinity. However, when enough time was given (6.5 h), higher crystallinity was attained, as evident through XRD. Therefore, even when no CNT is present, the samples show significant photocatalytic activity for RhB under visible light irradiation. The influence of higher temperature and longer time was also seen in the case of phenol photodegradation where higher photocatalytic activity was seen with rise in time and temperature. This shows that the time and temperature of hydrothermal crystallization was very effective in enhancing the photocatalytic performance of our BiOCl samples. In addition to this, the effect of CNTs on crystallinity was also visible, for instance, increase in the degree of crystallinity with increase in CNT amount. Contrary to this, the activity enhancing role of CNT was suppressed in other cases due to hydrothermal crystallization

conditions which means higher hydrothermal time and temperature were sufficient for crystal formation even in the absence of CNT. This is why we cannot see any clear trend for samples with different CNT compositions in **Figure 13**. This shows that parameters like time, temperature and CNT amount were competing with each other to gain effective crystallization. In the case of phenol photodegradation, the beneficial effect of CNT was suppressed due to hydrothermal crystallization, as can be seen in **Figure 15**, the increasing photocatalytic activity, in most of the cases, with increase in hydrothermal time and temperature.

The difference in photocatalytic activity of RhB and phenol can be explained by two facts. Firstly, the adsorbability of the two model pollutants: it can be presumed that CNT could enhance the adsorption of RhB in certain cases (especially in the case of shorter hydrothermal time, 4.5 h). Thus, the trapping of the organic compound on the surface of the photocatalyst is facilitated which then can migrate to the photo catalytically-active sites. Secondly, the photosensitizing effect of the dye which helps in harvesting the energy of visible light *via* RhB adsorption even though a semiconductor with relatively high band gap was present (with higher crystallinity of BiOCl these effects are suppressed).

5.1.3 Correlation of photocatalytic activity with different parameters

Several correlations were made to see the dependence of photocatalytic activity on the structural and optical properties of BiOCl. These two parameters were selected because the results from XRD and DRS gave some hints. Firstly, the correlation with the structural properties (*primary crystallite size)* of BiOCl with the photocatalytic activity was made. Crystallite size is one of the important parameters to consider because it has an influence on the photoactivity, as reported in previous studies [42, 45]. Generally, the higher crystallite size means lower specific surface area which means lower number of active sites and thus, lower photocatalytic performance – although the surface normalized values could be higher [46]. In our case, BiOCl samples with higher crystallite size showed higher photocatalytic activity and were among the best samples for phenol photodegradation. Therefore, in the subsequent section you will find the discussion related to this in detail.

Crystallite size vs. photocatalytic activity

In this section, we tried to correlate the CNT amount with the primary crystallite size and photodegradation efficiency. When lower temperature was used (120°C), a narrow range of crystallite size was seen, as shown in **Figure 16** (marked in green and blue). As more and

more energy was applied to the samples which means when the higher temperature was used (150°C, 4.5 and 6.5 h), a wider range of crystallite size was found, *see* **Figure 16** (marked in red and purple). The spectrum of crystallite size grew with rise in hydrothermal crystallization temperature which was enough for CNT to impart crystallinity and further take part in the charge distribution process. This means that if enough time and temperature is given to the crystals for their growth and higher crystallinity could be obtained which may be advantageous for photocatalytic processes and *vice-versa*. From **Figure 16** (*top right)*, it is clear that the samples with lower or no CNT amount (0.5 or 0%) prepared at higher temperature (150°C) showed higher photocatalytic activity even though they have larger crystallite size and lower crystallinity (evident from XRD). This indicates that crystallite size is one of the prime or controlling-factor in defining the photocatalytic activity of BiOCl/CNT composites at a lower CNT amount. The samples with higher CNT amount (2%) from the same sample series also showed higher photodegradation efficiency (*top left* in **Figure 16**) which again points to the fact that there could be other factors also that might be influencing the photocatalytic activity of the composites.

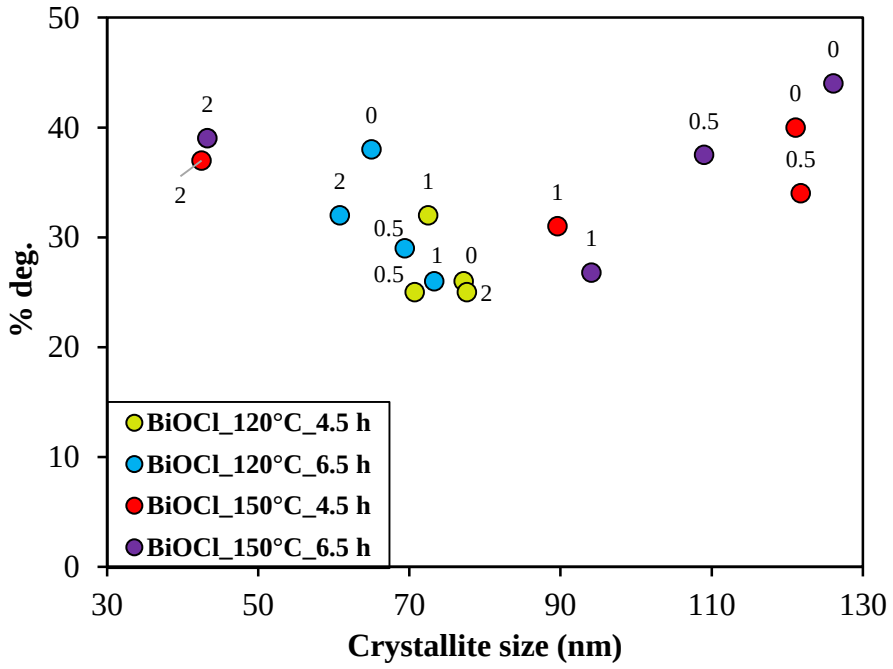

Figure 16. Correlation between crystallite size and photocatalytic activity of BiOCl and BiOCl/CNT for phenol under UV-A light irradiation.

Thereafter, we made a correlation with the band gap energy and the photodegradation efficiency but no direct relation was seen. However, when we compared the first derivative spectra (absorption maximum) with the photocatalytic activity,

significant conclusions could be made. As represented in **Figure 17**, at the highest percentage of CNT (2% CNT), clear dependence on excitability was observed. Therefore, it was an indication that there exists a relation between the CNT amount and optical properties of BiOCl/CNT samples. Moreover, at a lower percentage of CNT (0, 0.5 and 1% CNT), no dependence on optical properties was found. These compositions do not seem to interfere with the optical properties of BiOCl/CNT composites although lowering of band gap was observed in the case of composites (**Appendix1**). This is why these compositions of CNT-containing samples were not represented in **Figure 17**. Out of all, the most relevant and significant relation, as mentioned above, could be seen for the highest CNT amount (2%). These samples showed red-shift (still in the UV region due to the wide band gap of BiOCl) which could be considered as one of the other possible reasons for their higher photocatalytic activity. Considering **Figure 17**, as the crystallization conditions favored higher crystallinity, red shift appeared in the samples with increasing hydrothermal crystallization time and temperature which further resulted in higher photocatalytic activity.

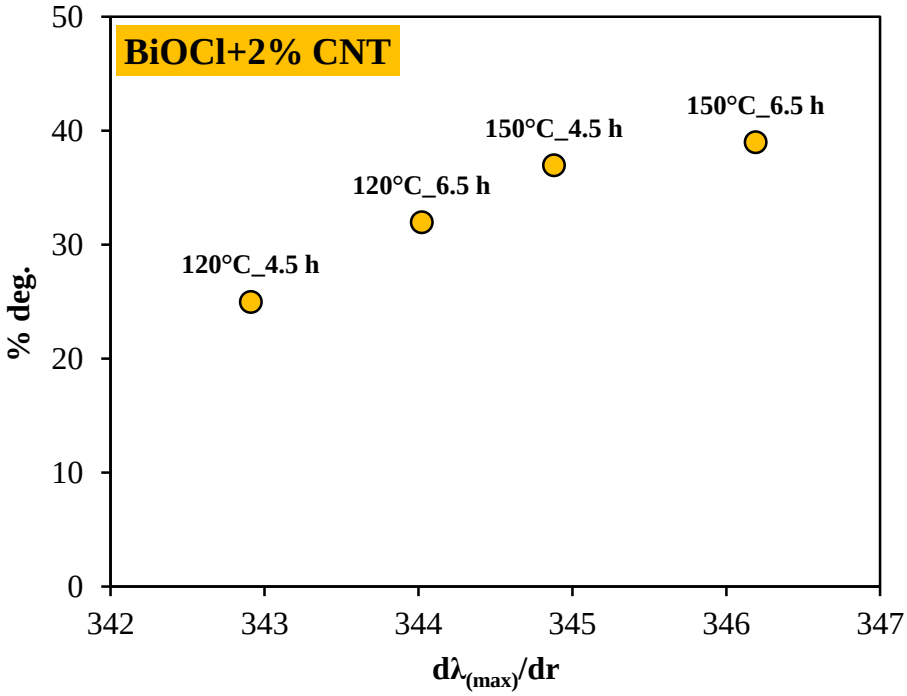

Figure 17. Correlation between the first derivative absorption maximum and degradation efficiency of BiOCl+2% CNT composites (prepared at 120°C, 150°C and 4.5 h, 6.5 h each) showing dependence on excitation wavelength.

It is evident that samples on the left in **Figure 17** were the ones with the least crystallinity (visible through XRD) which increased as we go up with higher hydrothermal temperature and time conditions. As calculated from the Scherrer equation, the highly

crystalline material among this (150°C, 6.5 h) has the smallest crystallite size and therefore, higher surface properties and thus superior photocatalytic activity. This correlation showed that there is an interaction between the optical properties of the semiconductor material and CNTs at a specific concentration. From **Figures 16** and **17**, important conclusions could be made in regard to CNT amount and hydrothermal crystallization conditions on the photocatalytic performance of BiOCl. As evident from these results, 1% CNT did not show any clear relation neither to structural nor to optical properties with respect to photocatalytic activity. Nonetheless, lower CNT amount showed dependency on structural properties (crystallinity and crystallite size) and higher CNT amount on optical properties (absorption wavelength). From all the results obtained and different correlations seen, it can be considered that not just the presence of sole CNT could contribute to higher photocatalytic activity of semiconductor materials like BiOCl. Such a modifier also requires sufficient energy to play a role as a photocatalytic activity enhancer in the charge separation phenomena.

5.2 BiOI and its composites with CNT

5.2.1 Characterization of BiOI and BiOI/CNT

Similar to the structural investigation of BiOCl, the diffraction patterns of BiOI and BiOI/CNT composites were investigated using X-ray diffraction technique. The diffractograms showed the presence of pure BiOI phase along with the other iodide-deficient bismuth oxyoiodides phase, namely, $Bi_4O_5I_2$, $Bi_7O_9I_3$ and Bi_5O_7I. **Figure 18 (a)** and **(b)** shows the diffractograms of BiOI and BiOI/CNT sample series prepared at 150°C for 6.5 and 4.5 h, respectively. The characteristic peaks for CNT were not observed, as in the previous case of BiOCl, due to their relatively low amount and overlapping with the diffraction peaks of BiOI crystallographic planes.

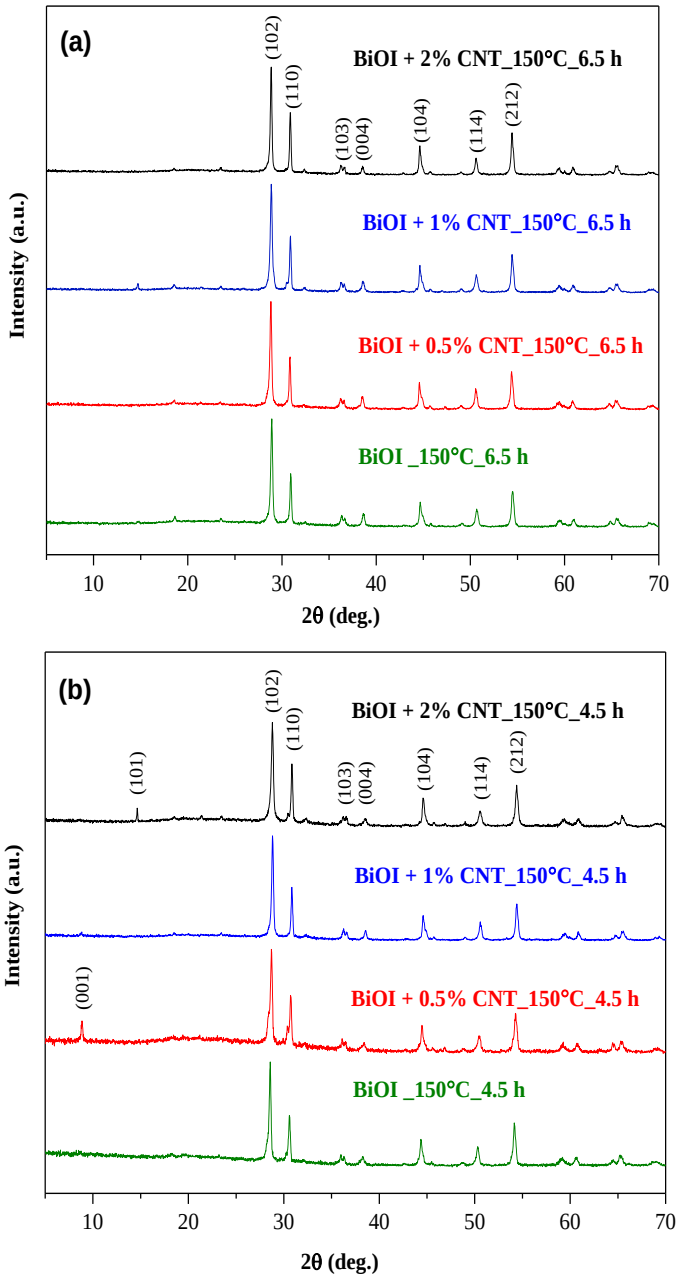

Figure 18. XRD diffractograms of the investigated BiOI and BiOI/CNT samples prepared at 150°C with different time intervals **(a)** 6.5 h **(b)** 4.5 h.

It is interesting to note here that all the characteristic peaks for tetragonal BiOI phase (JCPDS 00-73-2062, 10-0445) were found to be shifted towards smaller diffraction angles. For instance, the characteristic peak for BiOI (the most intense peak (102)) was shifted from 29.7° to 28.5°-28.8°, as shown in **Figure 19**. This peak shifting was observed for nearly all the samples. For instance, the peaks at 28.6° and 28.8° correspond to the characteristic peaks of $Bi_7O_9I_3$ and $Bi_4O_5I_2$, respectively, as reported previously in [138, 139]. This shift in peak position is probably due to the extra bismuth and oxygen atoms due to iodide-deficiency in

BiOI crystal lattice, which is also well-supported by other reports, giving rise to other iodide-deficient bismuth oxoiodides [65].

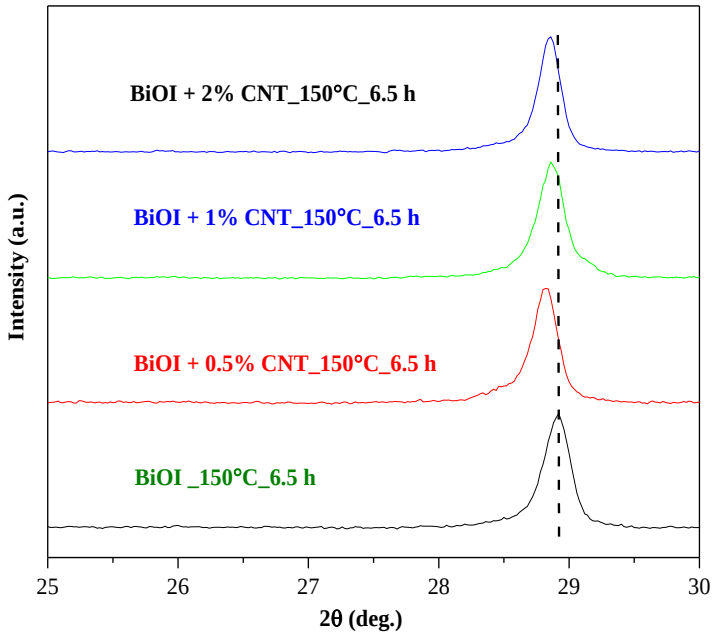

Figure 19. The zoom view of the XRD diffraction pattern of BiOI/CNT samples prepared at 150°C for 6.5 h showing the peak shifting of (102) crystal facet to smaller diffraction angles indicating the presence of other iodide-deficient bismuth oxoidodes besides BiOI.

The diffraction pattern of $Bi_4O_5I_2$ (characteristic peak at 28.8°, JCPDS # 713448) is quite different from that of BiOI (characteristic peak at 29.7°, JCPDS # 10-0445), which makes it easier to distinguish between the two phases. Interestingly, it has been reported that the XRD pattern of tetragonal BiOI and $Bi_7O_9I_3$ are very similar and it is hard to clearly identify the two phases [141]. This seems to be misleading because after a thorough literature search we found that everywhere the standard JCPDS file or reference of $Bi_7O_9I_3$ diffraction pattern is wrongly quoted and rather, in most cases, denoted to $Bi_4O_5I_2$ standard diffraction file. Therefore, we concluded that the diffraction patterns of $Bi_4O_5I_2$ and $Bi_7O_9I_3$ are very close to each other with their characteristic peaks at 28.8° and 28.6°. This is because the more iodine loss, the stronger shift of diffraction peaks to lower angle due to increase in lattice parameters [142].

An important observation was made at this point. The presence of $Bi_4O_5I_2$ was seen at higher temperature conditions (150°C) while application of lower temperature leads to the stabilisation of $Bi_7O_9I_3$ and Bi_5O_7I phases. This phase transformation of BiOI is supported by the fact that as the heat treatment is applied or calcination of BiOI progresses, pure BiOI transforms to other oxyiodide or oxide-forms, since those are thermodynamically

favourable [143]. Yu Changlin *et al.* also reported about the thermal instability of BiOI [144]. Unlike in their work, lower temperature influenced the crystallinity, however, in our studies, CNTs enhanced the crystallinity of our samples which was also observed in our BiOCl case. With increasing amounts of CNT, a higher degree of crystallinity was achieved which, indeed, influences the photodegradation process. In this way, it could be considered that CNT facilitates the formation of ordered structure. Hence, for obtaining crystalline structures, CNT could play a major role. Finally, the primary crystallite size of all BiOI and BiOI/CNT samples were also calculated *via* the Scherrer equation. The average crystallite size falls in the range between 55 and 90 nm, except for the sample BiOI at 120°C for 4.5 h. Moreover, the variations in crystallite size were found to be independent of the amount of CNTs. There is also no significant difference observed in the particle size based on the compositions prepared at different synthesis conditions. The effect of synthesis conditions on the occurrence of different forms of bismuth oxoiodides are as follows:

(i) Applying higher temperature conditions for longer duration (150°C, 6.5 hours), $Bi_4O_5I_2$ phase was identified.

(ii) When the temperature was increased but with the shorter duration (150°C, 4.5 hours), $Bi_4O_5I_2$ phase became predominant again.

(iii) When the temperature was decreased (at 120°C), irrespective of time, the end result indicated the presence of different phases ($Bi_7O_9I_3$ + Bi_5O_7I). In a similar condition, the presence of mixed phases was observed and such changes were reported due to the difference in pH conditions, as described by Xian Xao *et al.* [145].

These results suggest that heat-treatment plays a crucial role in defining the conversion and formation of new crystal structures, especially in the BiOI case. This issue was also highlighted by Hang Liu [146]. Herein, correctly identifying the different phases of BiOI becomes very important, as will be discussed in the subsequent sections. One significant point here is that in our study we have used simple hydrothermal crystallisation conditions and not special heat treatments, like calcination, which operates at higher temperatures (>300°C) which are quite well-known with crystal structure transformations. Contrary to this, as mentioned before, co-existence of other forms of bismuth oxoiodides in our study was observed without performing heat treatments. This subject raises question on the compositional changes that may occur in the case of BiOI as induced by synthesis conditions, especially at lower temperature. Therefore, these parameters must also be considered that may interfere with the phase transformation-like phenomena in BiOI. If the

above descriptions are true about the presence of iodide-deficient species then we may get some confirmation also through the following subsequent section of EDX.

As mentioned, the samples were tested for their elemental composition by EDX to further confirm the iodine deficiency in the prepared BiOI and BiOI/CNT samples. As it was demonstrated in the previous section's XRD part, the higher hydrothermal temperature condition led to changes in the structural properties of BiOI/CNT composites. Interestingly, similar observations were also noticed in case of compositional characteristics. The measurements of samples synthesised at 150°C showed compositional changes which indicates iodine deficiency, as presented in **Table 3**. Further, the iodine leaching was also observed during washing of samples which again indicates the loss of iodine from the samples. Not only this but iodine fumes were also visible when autoclaves were opened and the "free" iodine painted the Teflon® of the autoclave in "pinkish/purplish" colour which again proves iodine deficiency in the prepared samples. At this point, it is important to note that iodine was not added in excess (*see in synthesis section*).

Table 3. Atomic ratio values of Bi/I/O elements in sample series of BiOI and BiOI/CNT prepared at 150°C for 4.5 h.

BiOI and BiOI/CNT prepared at 150°C for 4.5 h	**Bi (atomic%)**	**I (atomic%)**	**O (atomic%)**	**Theoretical Ratio (Bi:I:O)**	**Experimental Ratio (Bi:I:O)**
BiOI	15.44	14.48	66.39	1:1:1	1:**0.93**:4.5
BiOI+0.5%CNT	16.47	14.49	64.51	1:1:1	1:**0.88**:3.92
BiOI+1%CNT	16.37	15.12	64.00	1:1:1	1:**0.92**:3.91
BiOI+2%CNT	17.43	14.53	65.41	1:1:1	1:**0.83**:3.75

All BiOI and BiOI/CNT samples were found to have low specific surface areas ranging from 2.6 to 9.2 m^2/g. This was also seen in the case of BiOCl. No specific trends were observed with different CNT content or hydrothermal synthesis conditions (time and temperature). The low specific surface area of composites is also evident from XRD due to higher primary crystallite size. These low values for specific surface area for our samples is usual in the case of bismuth-based or bismuth oxyiodides as discussed in [147]. The detailed

list of average primary particle size, specific surface areas and band gap energy values of all BiOI and BiOI/CNT samples is provided in **Appendix 2**.

The morphology of BiOI samples was analysed by SEM to study the influence of temperature (if any) on morphology of the samples. As shown in **Figure 20**, two distinct types of morphology were observed with changes in the hydrothermal crystallization temperature, unlike BiOCl where no morphological changes were seen with temperature changes. With the rise in temperature from 120°C to 150°C, a complete transformation in morphology of BiOI and BiOI/CNT was observed. The morphology changed from sheet-like to microflower-type structure when the temperature was increased from 120°C to 150°C, respectively. The BiOI/CNT composites have irregular nanosheet-like morphology with smooth surface at 120°C, as shown in **Figure 20 (a-c)**. The catalyst particles could be seen as aggregated on the CNT surface just like in the case of BiOCl and also, CNT were found to be non-uniformly distributed throughout the sample. The microsheets were stacked on top of each other and partially aggregated as well, shown in **Figure 20 (a)**. As discussed above, the samples have low specific surface areas which was also reported in a study by Yun Jang *et al.* [148]. Apart from agglomeration of nanosheets and carbon nanotubes, there were holes present on the surface of microsheets obtained at lower temperature conditions (120°C). Similar porous-kind of morphology was also observed by Yang *et al*, where porous Bi_5O_7I microsheets was reported in [148]. The deposition of catalyst particles on the walls of CNT could be seen in **Figure 20 (c)**. In most of the studies, it was reported that the use of solvents like polyethylene glycol can facilitate in obtaining hierarchical structures and helps in the prevention of agglomeration of sheets but the use of water doesn't seem to solve this problem. This is why we could see agglomeration of plates at lower temperature (120°C). However, in our study, with change in temperature conditions, three-dimensional morphology was obtained. In a way, it could be said that, in our study, the self-assembly of sheets occurred at higher temperature conditions without using any surfactant or template-directing agent.

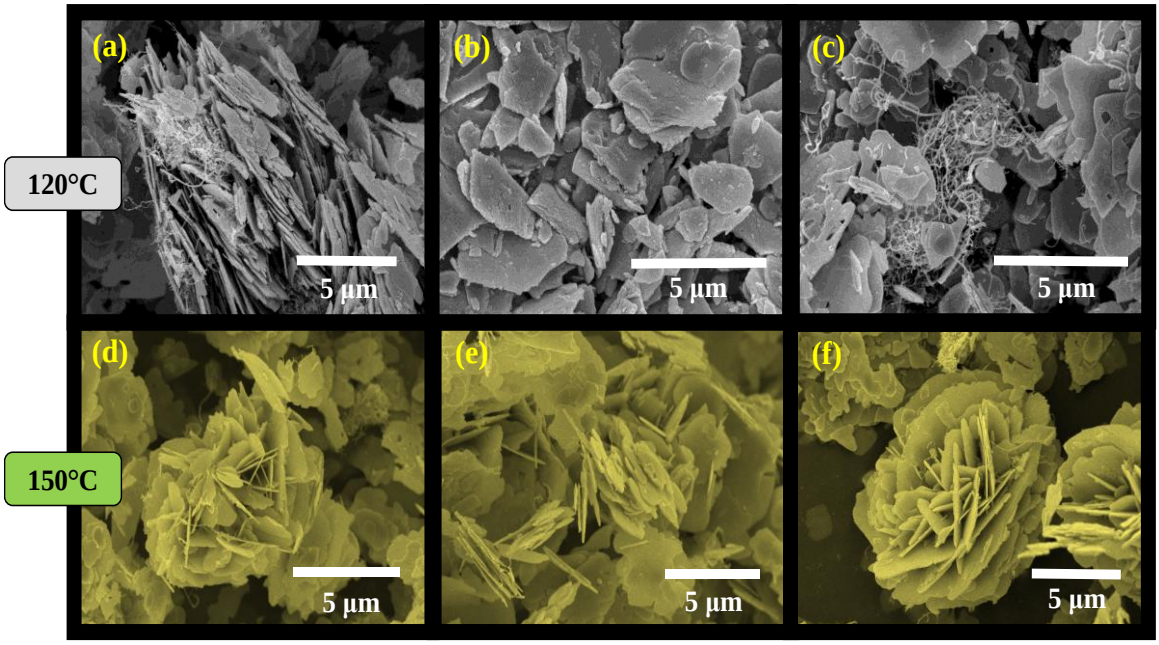

Figure 20. SEM micrographs of BiOI and BiOI/CNT composites representing the nanosheets and microflower-like morphology for the samples prepared at 120°C and 150°C, respectively. **(a)** BiOI+1% CNT_120°C_6.5 h **(b)** BiOI_120°C_4.5 h **(c)** BiOI+1% CNT_120°C_4.5 h **(d, e)** BiOI+1% CNT_150°C_6.5 h **(f)** BiOI+0.5% CNT_150°C_4.5 h.

The optical properties of BiOI and BiOI/CNT composites were investigated by diffuse reflectance spectroscopy (UV-DRS). **Figure 21 (a)** and **(b)** shows the DRS spectra of the composites for the band gap values of the prepared samples. The light absorption edge of prepared BiOI and BiOI/CNT composites was above 620 nm which suggests that the samples can be efficiently excited under visible light. The E_g of the prepared samples falls in the range of 1.46 – 1.82 eV. In the case of samples prepared at lower temperature condition (120°C) with nanosheets morphology, E_g values lied between 1.60 and 1.79 eV while in the case of higher temperature (150°C) with microflower-like morphology, the broader range of E_g was observed; ranging from 1.46 to 1.82 eV. The blue shift in absorption edge maximum was also observed. This blue shift is probably due to the presence of several iodine defects that modifies the band structures, also reported by Xuewen Wang *et al*. [70] This is in accordance with a report where a similar shift was also noticed in samples with iodine deficiency and oxygen rich bismuth oxoiodides.

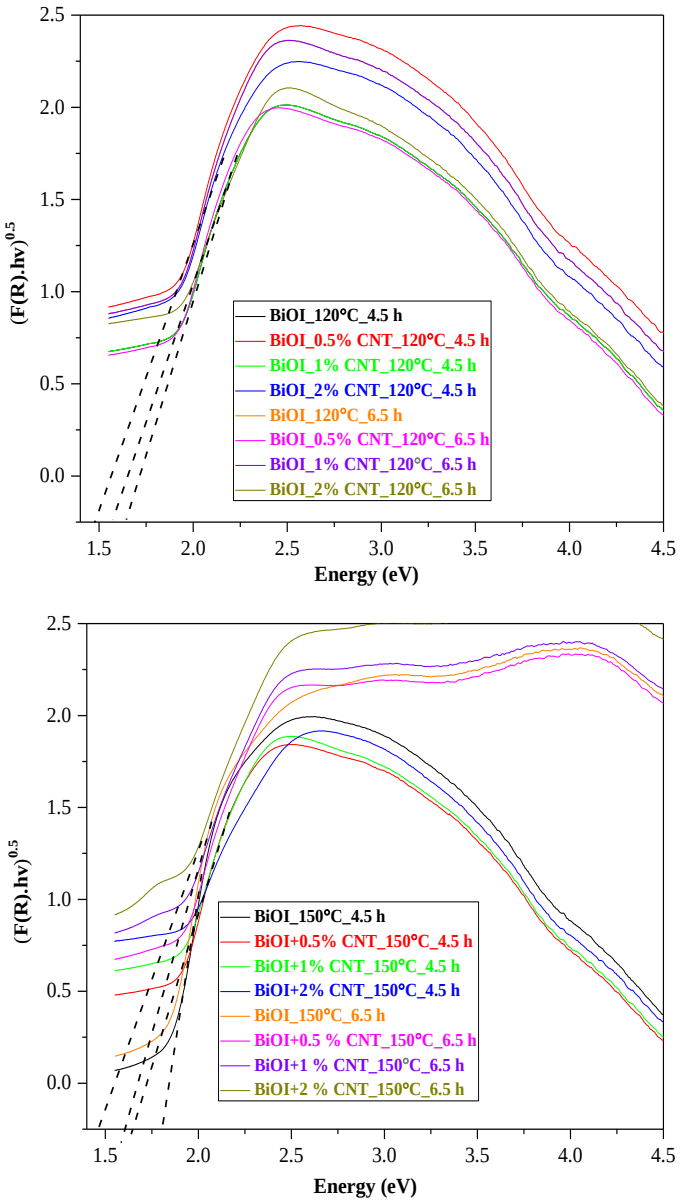

Figure 21. DRS plots of transformed Kubelka-Munk function *versus* the energy of BiOI and BiOI/CNT sample series prepared at **(a)** low (120°C) and **(b)** high (150°C) temperature conditions, both for 4.5 and 6.5 h.

Clearly, transition from tetragonal BiOI to monoclinic $Bi_4O_5I_2$ occurred when temperature was raised from 120°C to 150°C. As evident from our previous XRD and EDX discussion about the successful identification of iodine-deficient BiOI ($Bi_4O_5I_2$ + $Bi_7O_9I_3$ + Bi_5O_7I), this could be further supported through our DRS results which indicates the presence of compounds in a stoichiometric ratio (*i.e.* in a definite amount). This means that if the loss of iodide was in an indefinite amount, the peak of the first derivative spectra would be randomly distributed. This is in contrast to our results where the absorption maxima of those iodide-deficient bismuth oxoiodides had the maxima at the same point which again

indicates that controlled loss of iodide took place. The first derivative spectra for the samples with mixed phases are not represented here since their maxima was difficult to separate and not concrete information could be obtained from it. Another spectacular observation found was the relation of iodine deficiency on band gap values of composites. Theoretically, $Bi_4O_5I_2$ has least iodine deficiency and in this case, the samples containing predominantly $Bi_4O_5I_2$ phase showed lower band gap values. In contrast, $Bi_7O_9I_3$ and Bi_5O_7I are relatively more iodine-deficient in theory but samples with these phases attained higher band gap.

The Raman spectra of the BiOI and BiOI/CNT samples reveal information about the samples' crystallinity and surface defects. We identified vibrations modes at 96, 125, 148 (weak shoulder of the 125 cm^{-1} vibration mode), 238, and 307 cm^{-1} in the Raman spectra, as shown in **Figure 22 (a)**. We also observed weak shoulders in the 400 – 500 and 550 – 650 cm^{-1} regions. The Raman bands at 96 (slightly cut off on the spectrum), 125 and 148 cm^{-1} correspond to the Bi-X, respectively Bi-I bonds. The band at 238 and 307 cm^{-1} correspond to Bi-O vibrations bonds. The shoulders in the 400 – 500 and 550 – 650 cm^{-1} regions have been attributed to the Bi-O and Bi-O-Bi bonds. Regarding the presence of CNT in the composites, it is speculative to prove it by Raman Spectroscopy since only the G band was identified in the spectra, *see* **Figure 22 (b)**. The weak intensity of the G band and the D band's lack could be explained by the small amount of the added CNT.

From the information obtained from the Raman spectra, there is probably not only BiOI but also other bismuth oxides in the samples, evidenced by the shoulders at 238 cm^{-1}, between 400 – 500 and 550 – 650 cm^{-1} regions, and the band at 307 cm^{-1}. These bands appeared in every sample, so it is safe to conclude that the CNT addition did not induce their presence.

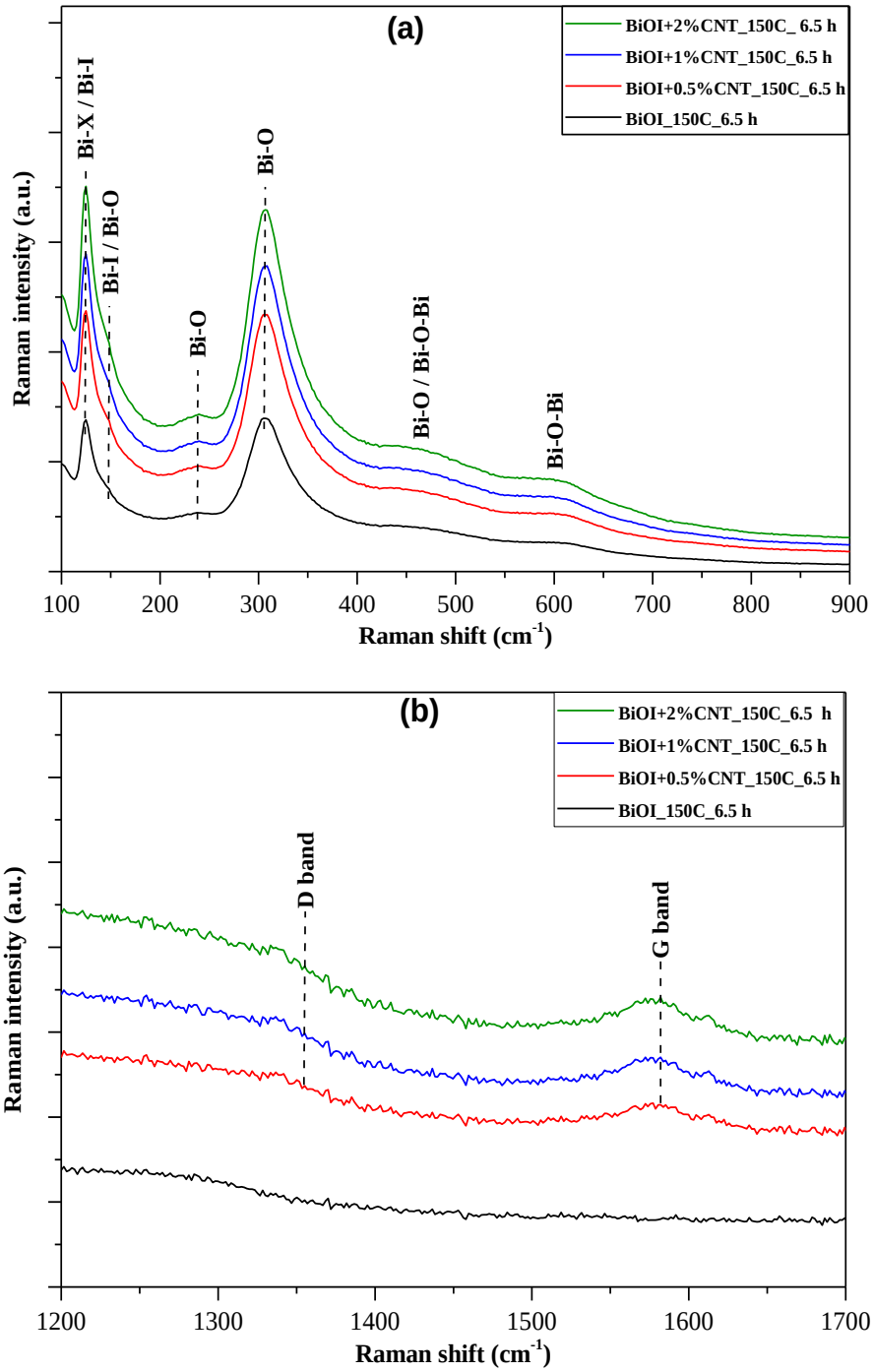

Figure 22. Raman spectra of **(a)** BiOI and BiOI/CNT composite samples **(b)** D and G bands of the CNT.

To prove the presence of surface defect in the samples, respectively I-vacancies, we have used the information obtained from the Raman spectra. To determine the surface defects ratio, we have chosen the intensities of the 307, 238 and 125 cm^{-1} bands since they provide information about the Bi-O and Bi-I bonds. The ratio of the following intensities was calculated: I_{307}/I_{125}, respectively I_{238}/I_{125}. The percentage of carbon nanotubes directly

influenced the samples' surface defects, *see* **Figure 23 (a)** – increased percentage of CNT lead to a higher number of surface defects, but also it impacts the photocatalytic activity concerning phenol degradation. The sample to which no CNT was added presented the smallest number of surface defects, but also the lowest photodegradation of phenol. The addition of CNT to the samples lead to more and more surface defects; which in turn lead to a higher photocatalytic activity for phenol degradation. This behaviour can be explained as with increase in the number of surface defects, more and more so-called active sites on the samples' surface are present which help to generate $^{\bullet}OH$ and $^{\bullet}O_2^-$ radicals, which are crucial for the photocatalytic degradation of phenol.

Concerning the percentage of CNT and surface defects determined from the I_{238}/I_{125} ratio (**Figure 23 (b)**) no obvious trend can be observed between them, but it should be mentioned that the peak percentage of CNT leads to the highest number of surface defects. In contrast when 1% CNT was present, the lowest number of surface defects was observed. Just as in the case of phenol degradation, also in the case of Rhodamine B degradation the same phenomenon was observed – namely that a higher number of surface defects leads to higher conversion rates. In contrast with phenol degradation, these surface defects, in the case of Rhodamine B can act also as active sites for the adsorption of the dye, but as well can enhance the samples' photocatalytic activity as discussed above.

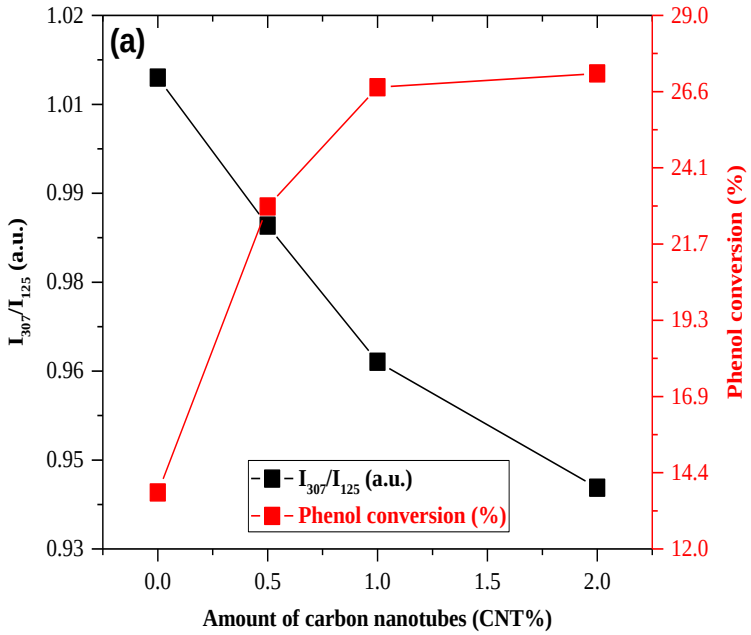

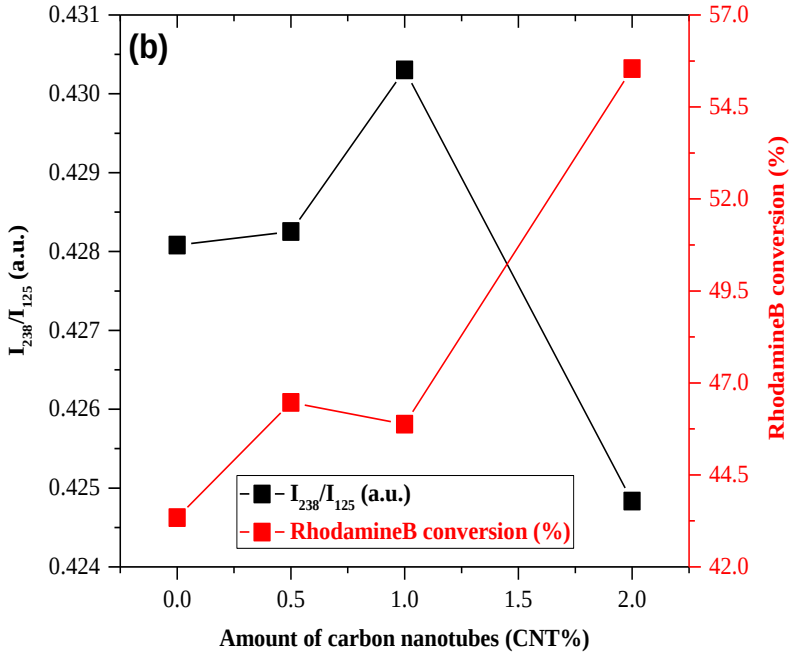

Figure 23. Correlations between the samples' surface defects and degradation efficiency (%) in function of carbon nanotubes (%) in the samples for **(a)** phenol photodegradation**,** reflecting the increase of surface defects with increase of CNT amount and hence, higher photocatalytic activity; **(b)** RhB photodegradation, representing no specific trends.

The photoluminescence is one of the most useful technique to evaluate the recombination rate of electron/hole pairs (e^-/h^+). **Figure 24 (a)** and **(b)** shows the PL spectra with excitation wavelengths at 450 nm and 365 nm, respectively. As we know, the lower intensity of PL spectra means lower recombination rate of e^-/h^+. In our case also, we could observe lower PL intensity and no fluorescence signal detected which indicated extremely low probability of charge carriers in all the sample cases suggesting higher photodegradation for phenol.

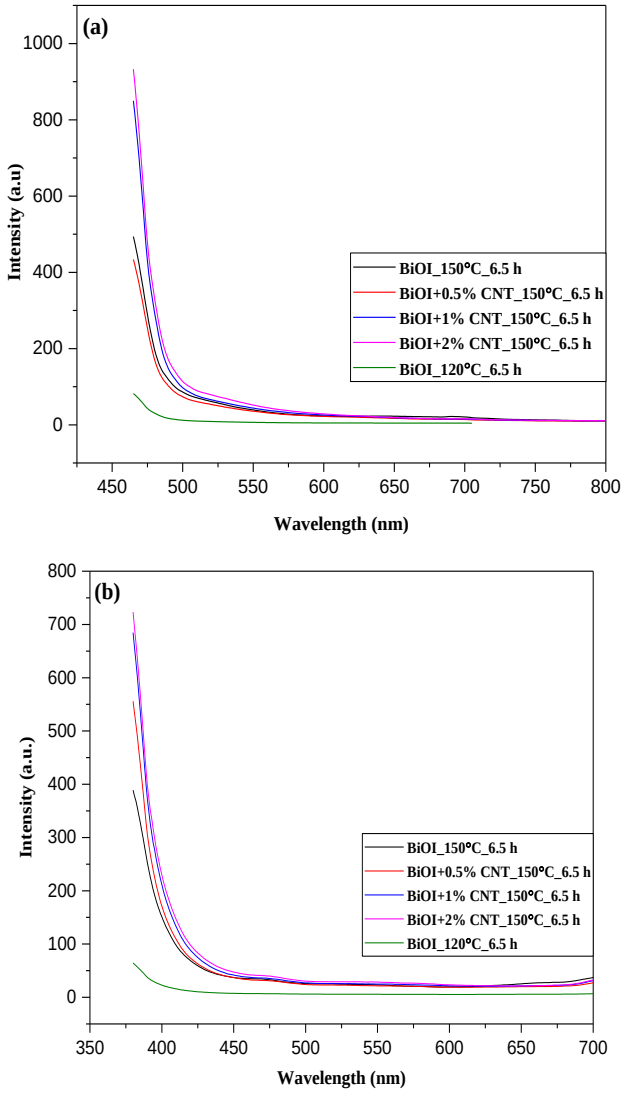

Figure 24. Photoluminescence (PL) spectra of BiOI and BiOI/CNT composites conducted at **(a)** 450 nm **(b)** 365nm.

5.2.2 Photocatalytic evaluation of BiOI and BiOI/CNT

Photocatalytic efficiency of BiOI and BiOI/CNT samples was demonstrated by the removal of two model pollutants (phenol and RhB) in aqueous solution under visible light (λ> 420 nm). This time-dependence degradation efficiency of BiOI/CNT composites was compared with their respective reference samples (without CNT). The composites were first tested for phenol. The minimum degradation efficiency of approximately 13% was attained after 240 minutes under visible light irradiation. This low efficiency was observed in the case of all BiOI reference samples, **Figure 25 (a)**. Conversely, an improved photocatalytic activity was seen in the case of BiOI/CNT composites. The highest degradation efficiency of around 28% was achieved by the sample BiOI+0.5%CNT prepared at 120°C for 4.5 h followed by BiOI+2%CNT synthesized at 150°C for 6.5 h under visible light irradiation.

The obtained-results show that in case of phenol the composites performed better than their respective references with maximum degradation efficiency of almost 2.8 times of the reference samples under visible light irradiation. **Figure 25 (b)** shows the photocatalytic efficiency of BiOI/CNT composites for phenol photodegradation under visible light irradiation.

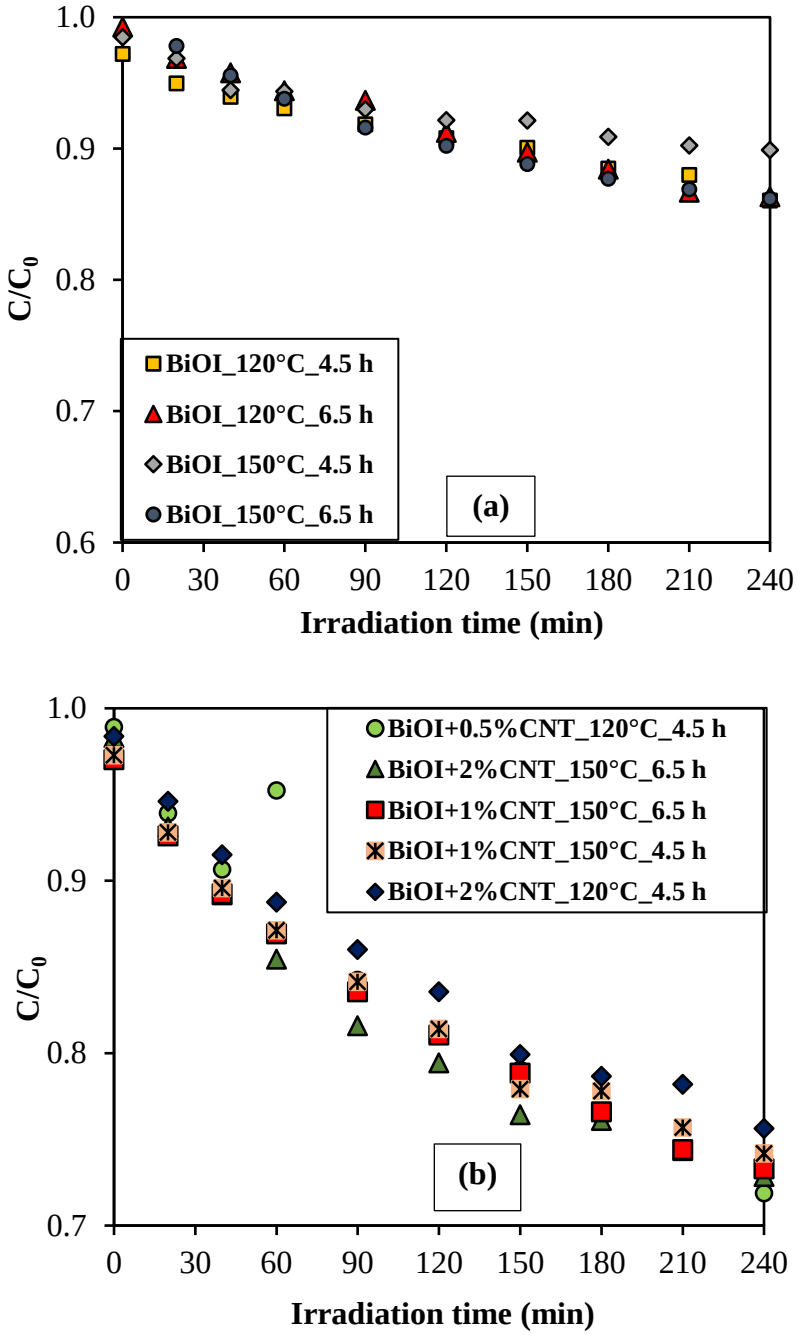

Figure 25. Photocatalytic degradation of phenol under visible light irradiation by **(a)** BiOI reference samples (without CNTs) showing poor performance; **(b)** BiOI/CNT composites showing higher photocatalytic activity.

The photocatalytic efficiency of BiOI and BiOI/CNT sample series was also evaluated for a coloured pollutant, rhodamine B (RhB), under visible light irradiation for a period of 120 min. Similar to phenol results, here also the composites of BiOI with CNT showed higher photodegradation of RhB than their reference samples, can be seen in **Figure 26 (a)** and **(b).** The best performing composites were from the sample series prepared at 150°C for 6.5 h. As can be seen from **Figure 26**, increase in CNT content resulted in enhanced photocatalytic activity of these composites with the maximum degradation efficiency of 56% under visible light irradiation. This is almost 2.5 times of its reference. It is noteworthy to point here that at this temperature the composites have microflower-like morphology which has been known to contribute in improving the rate of photodegradation process. The "second" best performing sample series was also from the higher temperature condition but with shorter duration, which again has hierarchical morphology. Among all, the composite of BiOI with 2% CNT composition prepared at 150°C and 4.5 h showed the best photocatalytic activity for RhB under visible light after 120 minutes while the same sample also performed relatively good in case of phenol photodegradation with almost 24% degradation efficiency under visible light irradiation. These results prove that CNT addition in BiOI resulted in gain of activity besides imparting crystallinity to the composites structures. This is opposite to what we have observed in our BiOCl case.

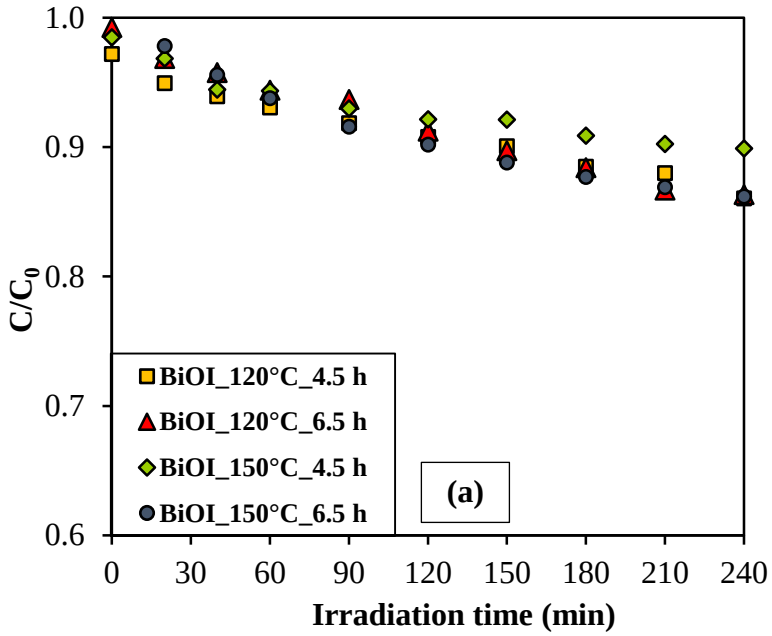

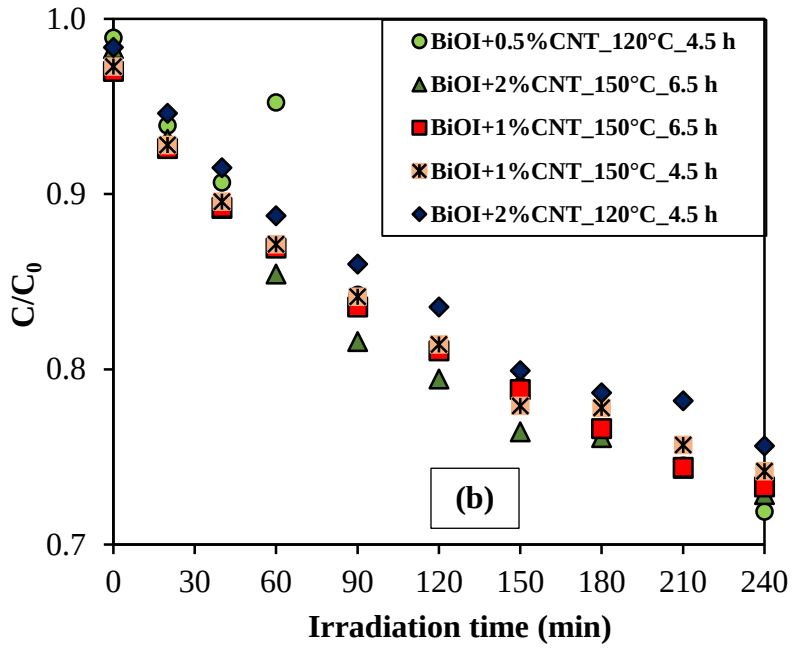

Figure 26. Photocatalytic degradation of RhB under visible light irradiation by **(a)** BiOI reference samples (without CNTs) showing poor performance; **(b)** BiOI/CNT composites showing higher photocatalytic activity.

It is ascertained here that CNT is not the sole reason for the enhanced photocatalytic activity as changes in physico-chemical properties of the samples were seen. For this reason, we wanted to correlate different parameters with the photocatalytic efficiency of the BiOI and its composites with CNT. In the subsequent section, some significant correlations are discussed.

5.2.2 Correlation of photocatalytic activity with different parameters

The best parameter to analyze the photocatalytic activity of a photocatalyst is their band gap (E_g). For that reason, we attempted to find correlations with E_g of all the samples with their respective photocatalytic efficiency for phenol and RhB and further, connecting with the different phase compositions obtained from XRD, EDX and DRS results.

Firstly, the connection between E_g and photocatalytic activity of the composites were made, shown in **Figure 27**. The correlation shows the similar trend for band gap energies of the composites to the degradation efficiency for both the pollutants (phenol and RhB) under visible light. From **Figure 27**, it is clear that as the band gap energy of the composites is increased, the photocatalytic activity decreases. This was a completely opposite trend which was observed in our previous BiOBr results. Besides, as mentioned in our DRS, the sample

with dominant phase **$Bi_4O_5I_2$,** has lower band gap energy value. Clearly, it is now also visible from our correlation that samples with lower E_g outperform the samples with higher band gap. Therefore, **$Bi_4O_5I_2$** could be regarded as an active phase.

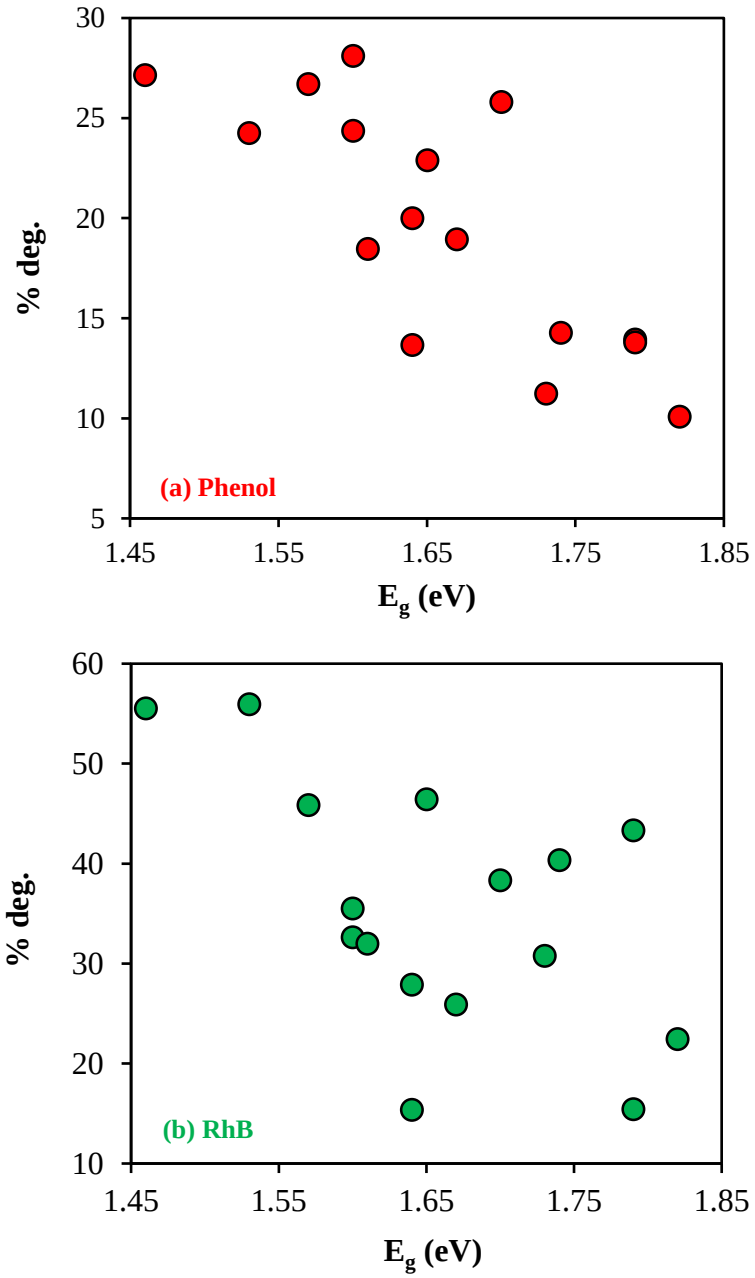

Figure 27. Correlation between the band gap energy (E_g) and photocatalytic degradation efficiency (%) of the investigated BiOI and BiOI/CNT composites for **(a)** phenol; and **(b)** RhB, under visible light irradiation, representing a decrease in photocatalytic activity with increasing E_g value of the samples.

Another significant correlation was made with the E_g and the presence of these different iodine-deficient BiOI species. The following observations were derived from this:

(a) It can be seen from **Figure 28** that samples containing **$Bi_4O_5I_2$** (denoted by number 5) is the most active, again verified previously from **Figure 27**.

(b) The samples with **$Bi_7O_9I_3$** (denoted by number 9) have relatively moderate activity.

(c) The samples with **Bi_5O_7I** (denoted by number 7) are the least active, even in its pure phase form, unlike the above-mentioned two phases, also justified from **Figure 27**.

(d) Another significant thing to be considered here is when the samples consisted of just the pure phase (5 or 7 or 9), the activity was lower as compared to the samples comprising of mixed phases (for *e.g.* 5+9 or 9+7 or 5+7).

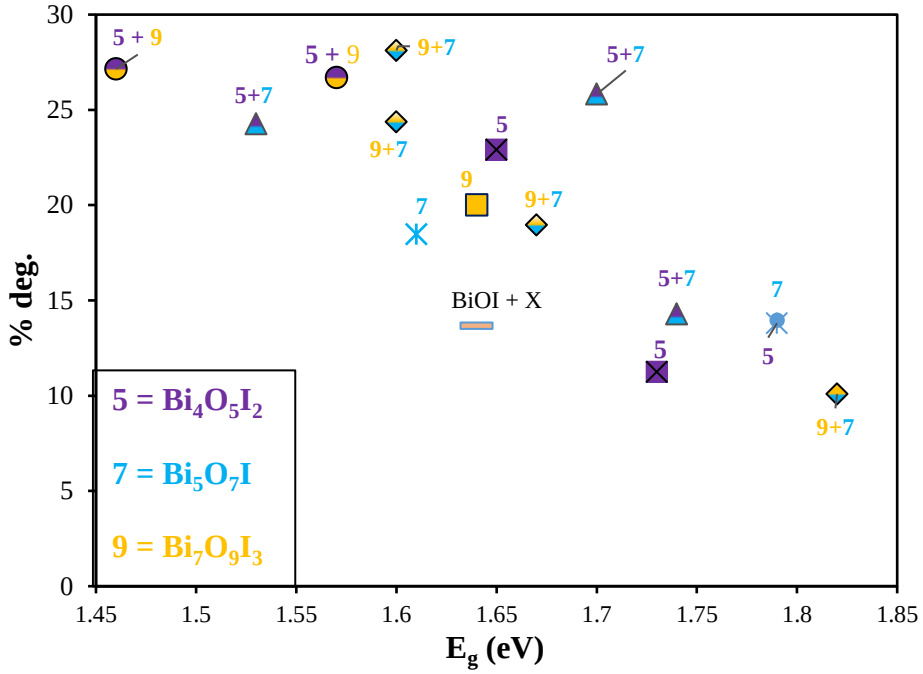

Figure 28. Correlation with E_g, photocatalytic efficiency and different phases of iodide-deficient BiOIs representing the influence of mixed phases on the overall photocatalytic performance of the investigated BiOI samples.

Theoretically, the order of iodine deficiency in the iodine-deficient bismuth oxoiodides is as follows: **Bi_5O_7I> $Bi_7O_9I_3$> $Bi_4O_5I_2$**, which means **Bi_5O_7I** has the least amount of iodine out of all and **$Bi_4O_5I_2$** contains more iodine than the other two. After carefully analyzing the correlations given in **Figure 28**, we can say that the activity of pure phases was enhanced when combined with other phases. This can be thought of appearance of a *"junction"* at the inner composite interfaces, in other words, the presence of mixed phases in the sample leads to the formation of certain heterojunctions within the same structure just like in the case of TiO_2 (at the interface of anatase and rutile phase) and that could be another reason for an enhanced activity of the composites. Moreover, the presence

of CNT is yet another important factor for increased photocatalytic activity as can be seen from photodegradation results. With slight increase in CNT content, high photocatalytic activity can be obtained. Therefore, it could be concluded here that a number of factors are contributing in efficient removal of the pollutants (phenol and RhB) by BiOI and the inter-dependence of several factors can explain the significance of studying about the thermally unstable behavior of bismuth oxoiodides.

5.3 BiOBr and its composites with CNT

5.3.1 Characterization of BiOBr and BiOBr/CNT

The structural and crystal phase analysis of BiOBr/CNT samples were done by X-ray diffraction technique. All the diffraction peaks for the BiOBr/CNT samples represent the pure tetragonal phase of BiOBr (JCPDS file number 09-0393), *see* **Figure 29** [149]. The characteristic peaks for CNT were not visible due to their low content and its overlapping with the diffraction peak (for instance, at $2\theta = 26.1^{\circ}$ [JCPDS 41-1487]) of (101) crystal facet of BiOBr. There were no observed shifts in the peak positions of the BiOBr/CNT samples indicating that the lattice structure of BiOBr did not change upon the addition of CNT. Crystallite sizes were also calculated *via* the Scherrer equation (**Appendix 3**). The increase in crystallite size was seen in two cases, (i) firstly, in the case of longer reaction times, *i.e.* from 34 nm to 61 nm when time increased from 4.5 to 6.5 h, and (ii) secondly, in the case of increased hydrothermal temperature, *i.e.* from 34 nm to 102 nm when the temperature was raised from 120ºC to 150ºC during 4.5 h of reaction time. This is consistent with other reports [150]. **Figure 29** shows the diffractogram of composites prepared at 120ºC and 4.5h with different amounts of CNT.

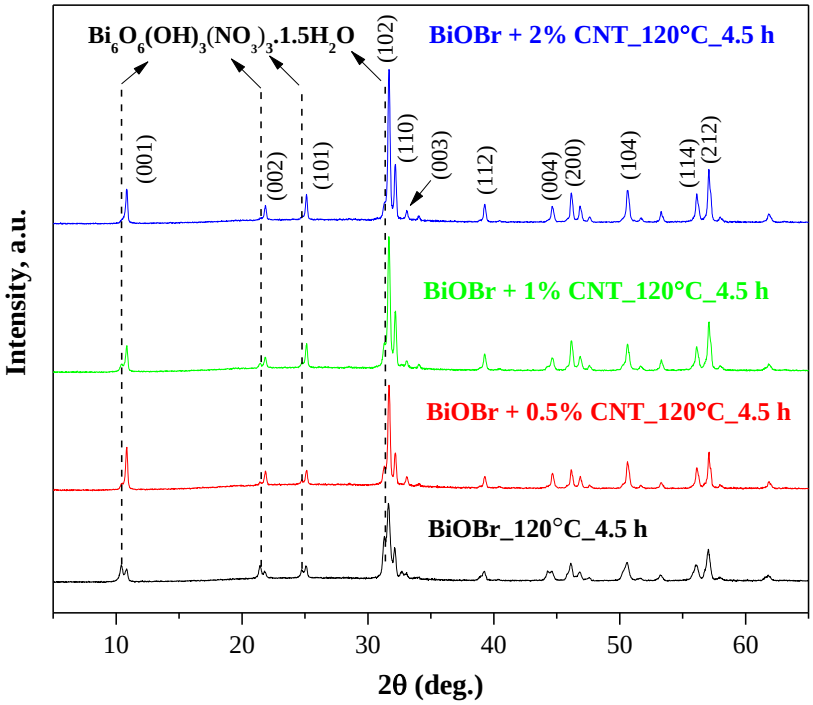

Figure 29. X-Ray diffractograms of BiOBr/CNT composites with different amount of CNT prepared at 120ºC and 4.5 h representing peaks indexed to BiOBr tetragonal phase (JCPDS#09-0393) and appearance of additional peaks of $Bi_6O_6(OH)_3(NO_3)_3•1.5H_2O$ as a side-product.

Additional peaks were observed in nearly all the samples at 10.3, 21.4, 24.6 and 31.3 (2θ°) values, which were identified as $Bi_6O_6(OH)_3(NO_3)_3•1.5H_2O$ (JCPDS # 53-1038), also shown in **Figures 29** and **30**. It is reported in literature that $Bi(NO_3)_3•5H_2O$ is readily hydrolyzed and leads to the formation of bismuth (III) nitrates with complex structures. These exist in 15 different structures and $Bi_6O_6(OH)_3(NO_3)_3•1.5H_2O$ is one of them. Also, $Bi(NO_3)_3•5H_2O$ was the precursor in our study, it can be imagined that the first hydrolytic step of the salt occurs by forming this structure. Furthermore, it disappears (maximum content calculated was 8.23 wt.% for the sample BiOBr_120°C_4.5 h) as the crystallinity of the sample increases. For instance, the parameters like increase of the CNT content or increased hydrothermal crystallization time resulted in higher degree of crystallization in the samples, also reported in our BiOI/CNT work [151]. It is also evident through XRD which reports increased diffraction peak intensity values in the presence of CNT. Furthermore, it should be noted that this material is also considered as a photocatalyst [152-154]. The presence of this compound is confirmed through its diffraction peaks.

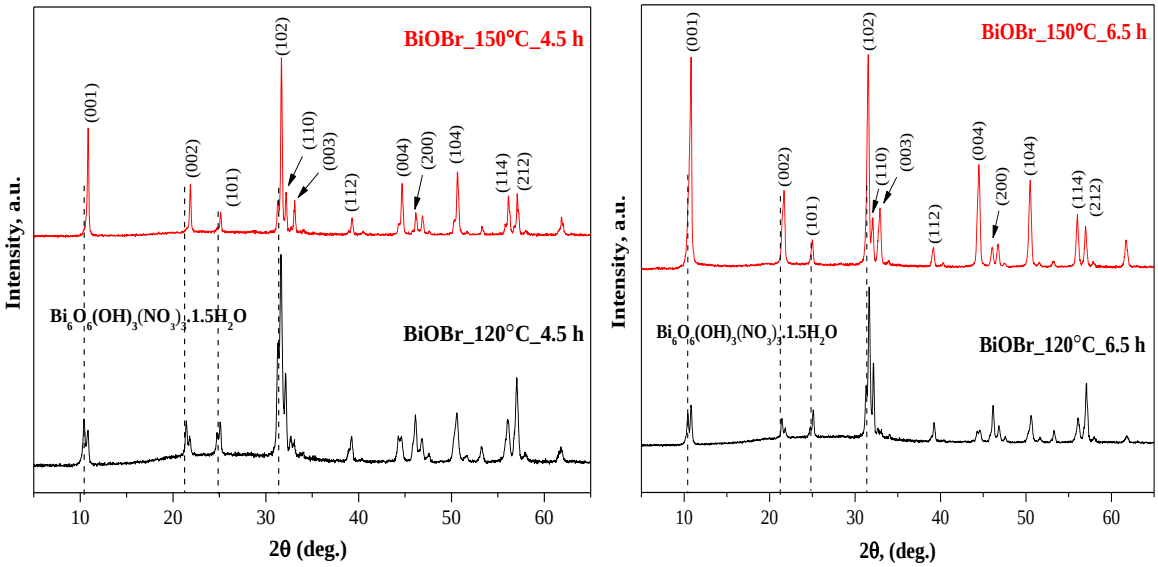

Figure 30. X-Ray diffractograms of BiOBr prepared at 120ºC (*left*) and 150ºC (*right*), both prepared at 4.5 h and 6.5 h showing the diffraction peaks for the newly appeared compound $Bi_6O_6(OH)_3(NO_3)_3 \cdot 1.5H_2O$.

The specific surface areas of the samples varied with changes in hydrothermal synthesis parameters (time and temperature). However, these measurements have confirmed that all the samples have low surface areas in agreement with the higher crystallite size as calculated from XRD data. The specific surface area ranges from 2.3 m^2/g to 7.3 m^2/g. The detailed list of average primary particle size, specific surface areas and band gap energy values of all the samples is provided in **Appendix 3**.

The morphology of the BiOBr/CNT samples were investigated using SEM. For all the composites, microplate-like structure was obtained. **Figure 31** shows SEM micrographs of the BiOBr/CNT composites prepared at 150ºC. **Figure 31 (a)** and **(b)** shows the morphology of BiOBr (reference samples) with microplate-like structure, stacked on top of each other. The CNT in the composites were found to be in close contact with the microplates. In **Figure 31 (c)**, from the investigated sample areas it seems that CNT were not homogeneously distributed throughout the sample. In addition to BiOBr microplates, the surface of CNT were covered with the BiOBr particles (see inset of **Figure 31 (c)**). At longer reaction time, a decrease in thickness of microplates was observed which ranged in between 133-145 nm for the samples prepared at 150ºC and 4.5 and 6.5 h, as marked in **Figure 31 (a)** and **(b)**, and in case of 120 ºC at 4.5 and 6.5 h, the values fall between 55-78 nm.

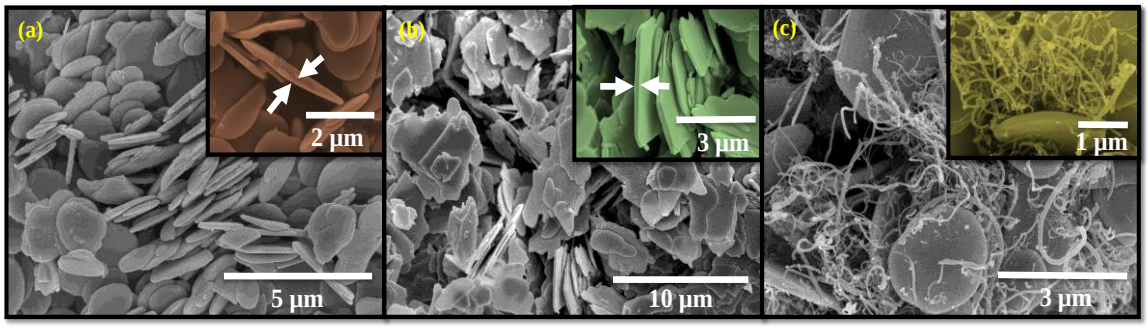

Figure 31. SEM micrographs representing the micro-plate like morphology of the investigated samples each synthesized at 150ºC **(a)** 4.5 h and **(b)** 6.5 h, and **(c)** BiOBr+0.5% CNT composite prepared at 150ºC for 6.5 h.

The light absorption property of BiOBr/CNT composites was measured by DRS and the band gap energy (E_g) of the prepared samples was calculated using the Kubelka-Munk function. Through the optical measurements, it was found that increase in CNT percentage led to a decrease in band gap value of the composites, from 2.87 and 2.84 eV in case of 0% CNT to 2.41 eV for 2% CNT. This may be due to the light absorption capacity of CNT that absorbs the available electromagnetic radiation (black color of CNT), also evident from the color of the samples. The band gap reduction also suggests the separation of charge carriers with low probability of recombination, although a short-circuiting mechanism is also known for these composites [120, 155]. Even though, a decrease in band-gap energy of the samples was found using Kubelka-Munk theory but when the first derivative spectra of DRS spectrum was analyzed, no shift in the absorption spectrum was found which means that these decreased E_g values were not the actual band-gap values of the composites. These represent somewhat misleading values of the band gap energy of the composites rather than indicate the overall band-properties of them.

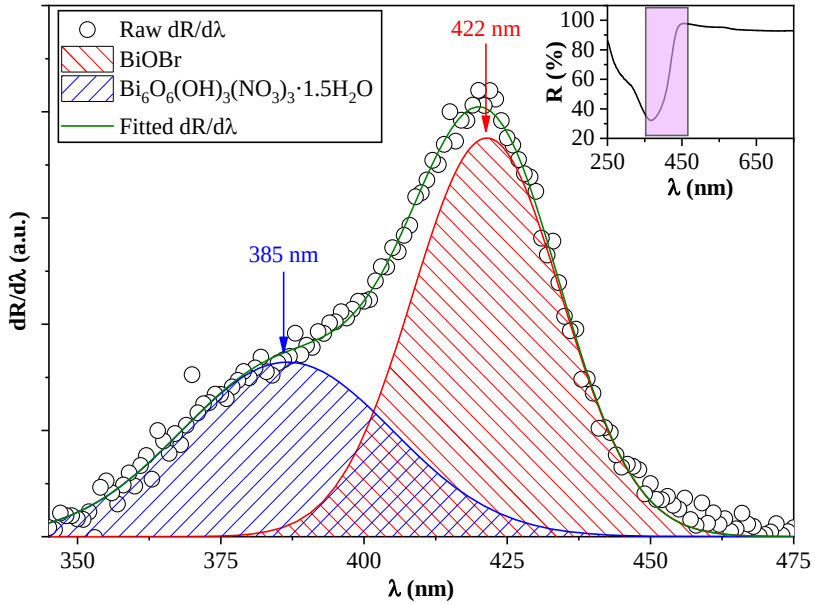

Figure 32. First derivative DRS spectrum of sample BiOBr_120°C_4.5 h showing two electron transition bands at 385 nm and 422 nm belonging to the two products, namely, $Bi_6O_6(OH)_3(NO_3)_3 \cdot 1.5H_2O$ and BiOBr, respectively; and the inset Figure shows the original DRS spectra of the same sample.

Further analyzing the band structure of the materials, the first derivative spectra of the samples were investigated. It was found that in all the cases two electro-transition bands were observed in nearly all the cases, shown in **Figure 32**. One at 3.3 eV (electron transition band located at 385 nm) and the other at 2.9 eV (electron transition band located at 422 nm). The band at 2.9 eV belongs to BiOBr but the second one was unexpected. However, in XRD section, it was found that $Bi_6O_6(OH)_3(NO_3)_3 \cdot 1.5H_2O$ was present in the samples. The band gap value of this compound coincides with the value reported in the literature, *i.e.* at 3.3eV [156]. Furthermore, this signal is omnipresent in all the samples, likewise, $Bi_6O_6(OH)_3(NO_3)_3 \cdot 1.5H_2O$ is also present but in different amounts. This shows that this compound will participate in the charge separation mechanism during the photocatalytic experiments.

5.3.2 Photocatalytic evaluation of BiOBr and BiOBr/CNT

After the characterization for structural, morphological and optical properties of BiOBr/CNT composites, the samples were investigated for their photocatalytic activity for the removal of phenol under visible light. **Figure 33** shows the photocatalytic degradation efficiency for phenol by BiOBr/CNT composites with different CNT compositions under visible light irradiation. We found that the samples without CNT showed the highest photocatalytic efficiency for phenol photodegradation. In our case, the trends as expected

from the theoretical information and literature were not observed with the addition of CNT even at lower concentrations. However, it can be affirmed here that one major trend is clearly visible from **Figure 33** which is that with increasing CNT content, lowered photoactivity was observed, except in the case of BiOBr + 1%CNT prepared at 150°C (4.5 h) where no precise activity order can be defined. The explanation for this increase in the activity of this sample will be discussed later in the stability section. Clearly, it is visible from **Figure 33** that CNTs did not contribute to the charge separation process and thus, the typical behavior of CNTs of trapping the electrons could be ruled out in our case. All BiOBr reference samples prepared at 120ºC and 150ºC showed the highest photocatalytic activity (as shown in **Figure 34**) for phenol under visible light irradiation. The reason for this trend is explained with the help of some correlations which will be discussed in the further sections in detail. For instance, significant correlations were found between the structural and optical properties of BiOBr together with its photocatalytic performance.

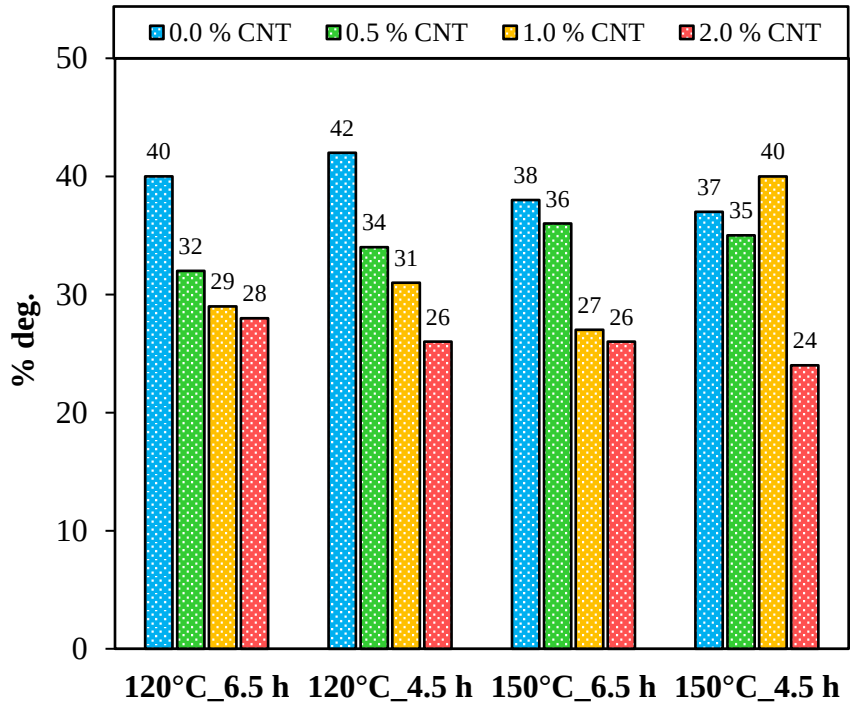

Figure 33. The comparison of % deg. of the investigated BiOBr and BiOBr/CNT samples with respect to the CNT amount reflecting a sharp decrease in the photocatalytic performance of the samples in presence of CNTs, except in the case of BiOBr+1%CNT synthesized at 150°C_4.5 h.

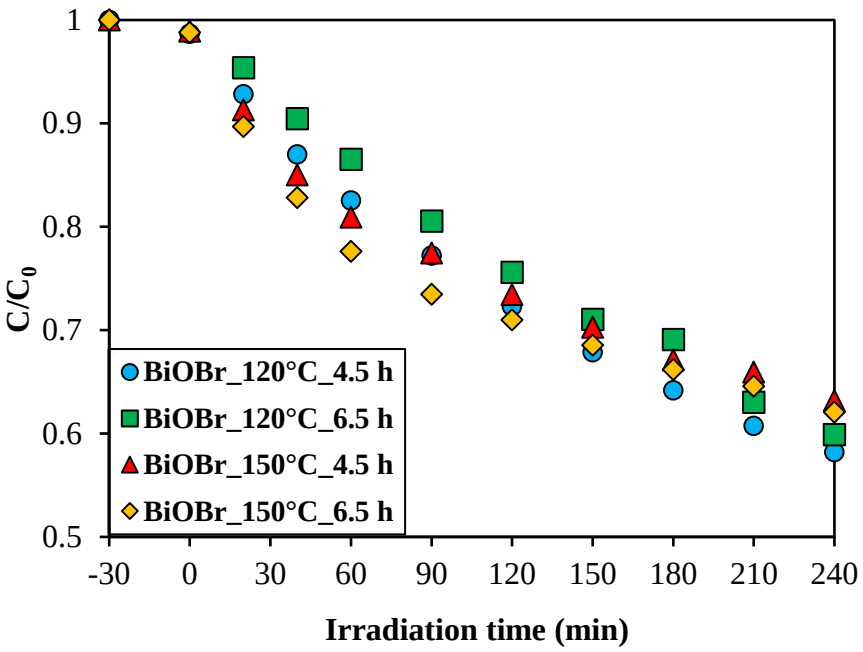

Figure 34. Photocatalytic degradation (%) of all BiOBr reference samples (without CNT) prepared at 120°C and 150°C for 4.5 h and 6.5 h (each) representing the highest photocatalytic efficiency obtained for the removal of phenol under visible light irradiation for 240 min.

5.3.3 Correlation of photocatalytic activity with different parameters

To gain insights about the decreasing photocatalytic activity of BiOBr/CNT composites, several correlations were made. The average primary crystallite size is a well-known parameter which has been widely studied and discussed in the literature (*e.g.* for TiO_2) [157]. Usually, with decrease in crystallite size an increase in the photocatalytic activity is found which is logical because the specific surface area increases as well. However, in the present case, we are dealing with very low surface area values (below 10 m^2/g). The photocatalytic degradation efficiency showed two types of dependencies:

i. Firstly, as the primary crystallite size increased (see **Figure 35**), the degradation efficiency of the photocatalysts decreased which is expected but after 80 nm particle size, the degradation values began to increase again. For instance, for the samples prepared at 150°C.

ii. The samples synthesized at 120°C did not show any changes in the trend unlike the samples prepared at 150°C.

These two observations pointed out that some structural changes may occur in the samples synthesized at 150°C which showed high (but not the highest) activity even at

higher primary crystallite size values. This shows the interference of some other factors at this temperature condition.

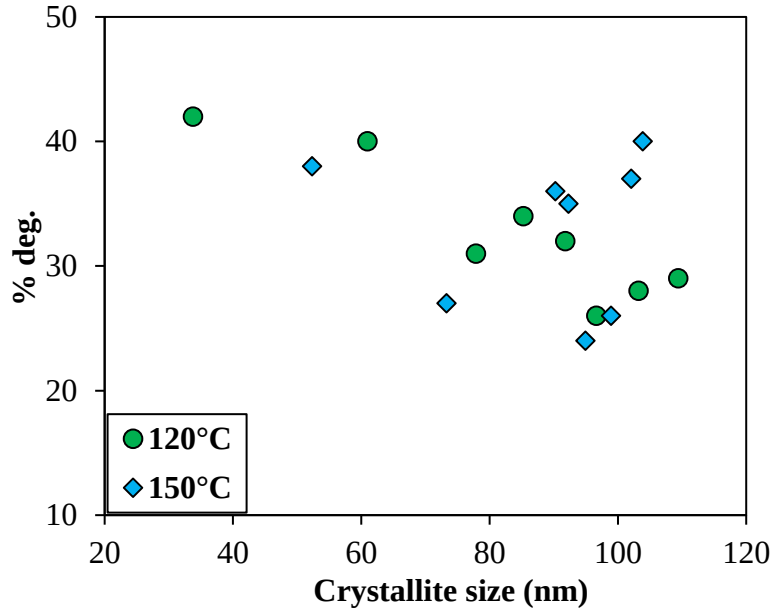

Figure 35. Correlation between the primary crystallite size (nm) and degradation efficiency (%) of BiOBr and BiOBr/CNT samples for the photodegradation of phenol under visible light irradiation showing the decreasing trend in photocatalytic activity with increase in crystallite size of the samples, except in the case of samples prepared at 150°C for 4.5 h.

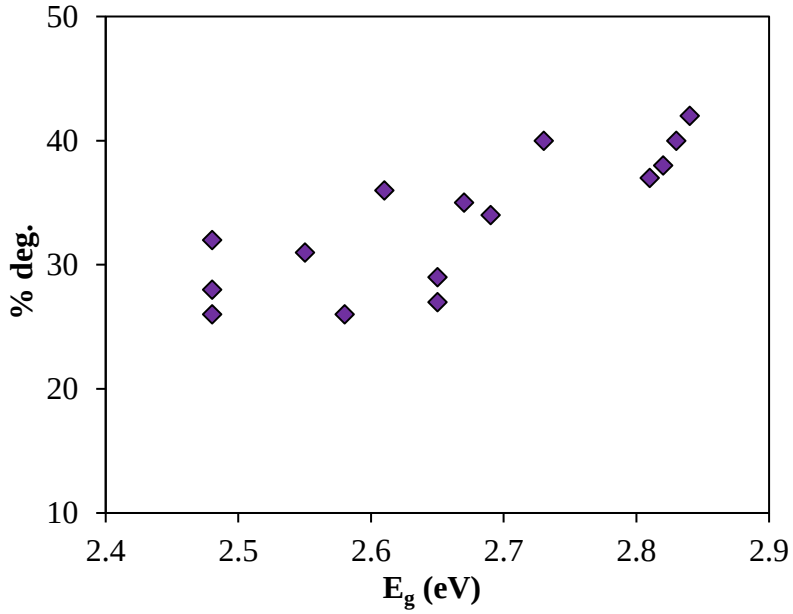

Figure 36. Correlation between the band gap values (eV) and the degradation efficiency (%) of BiOBr and BiOBr/CNT samples for the photodegradation of phenol under visible light irradiation representing the increase in photocatalytic activity with increase in band gap energy of the investigated BiOBr samples.

Figure 36 shows the correlation between the band gap energy values with the degradation efficiency. Although a decrease in the band gap values was observed with the addition of CNT, it did not contribute to the overall enhancement of photocatalytic activity, the fact that has been already observed in the case of titania photocatalyst doped with nitrogen [158]. BiOBr prepared at 120ºC and 4.5 and 6.5 h had higher E_g = 2.84 eV with the highest photodegradation efficiency of 40% and 42%, respectively, while the lowest band gap value (E_g) of 2.41 eV was obtained for the composites containing 0.5% CNT with lower photodegradation efficiency of 26% under visible light irradiation. However, this fact is very well supported from the data obtained from our first derivative DRS spectrum. As the amount of $Bi_6O_6(OH)_3(NO_3)_3$•$1.5H_2O$ compound increased (from 1.52% to 8.23%), the band-gap of the catalyst increased and also their visible light photocatalytic activity. At this point, it is important to mention that those materials which had higher E_g values are the samples without CNT and as proved through the XRD results that the samples with lower CNT amount were the ones with higher $Bi_6O_6(OH)_3(NO_3)_3$•$1.5H_2O$ content. Therefore, we can say that the presence of this by product ($Bi_6O_6(OH)_3(NO_3)_3$•$1.5H_2O$) was one of the possible reasons for the high photocatalytic activity of these samples. Also, it can be understood here that as the carbon nanotube content increased, the formation of BiOBr was favored instead of $Bi_6O_6(OH)_3(NO_3)_3$•$1.5H_2O$.

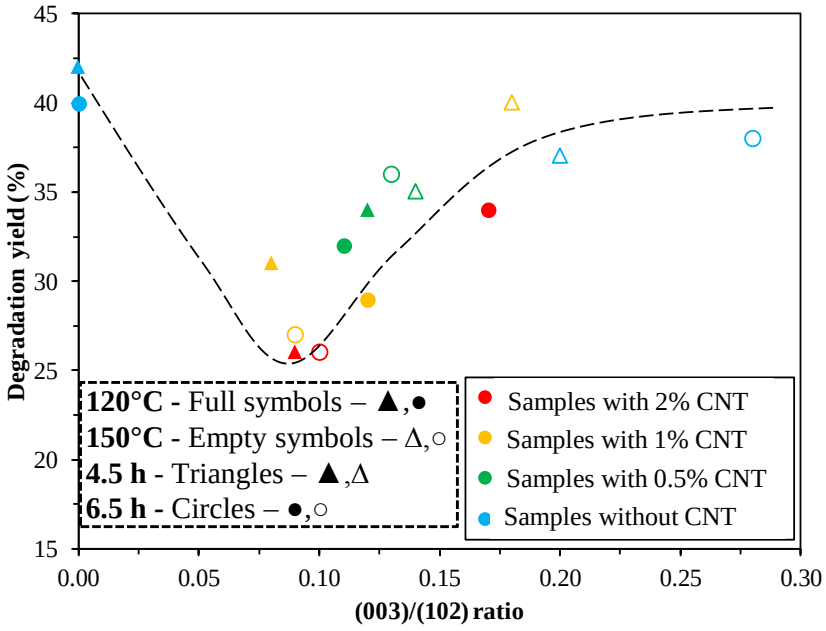

Figure 37. Correlation between (003)/(102) crystallographic planes' ratio and the photocatalytic degradation (%) of BiOBr and BiOBr/CNT samples for the photodegradation phenol under visible light irradiation reflecting the beneficial effect of (003) plane under certain circumstances.

Not just the presence of a specific compound would influence the activity. As these are shape-tailored materials the crystal orientation could also show the origin of the activity. That is why all the important diffraction peaks were indexed. One significant correlation was observed with that of crystal facet (003). In the literature, the reported crystal facets responsible for higher photocatalytic activity of BiOX includes (001), (120), (110) and (102) [159, 160]. Clearly, this was not the case here. The presence of (003) inhibited the activity of the BiOBr/CNT samples until the ratio of (0.075), after that, a constant increase of activity with the presence of (003) was noticed. In **Figure 37**, subseries values are denoted with different colors which show that except for sample series without CNTs, all the others aligne perfectly with the beneficial effect of (003). The highest amounts of CNT (2%) showed the lowest (003) presence which again emphasizes on the crystallization promoting effect of CNTs while the other CNT concentration values produced higher amount of the desired crystallographic plane. Furthermore, the two samples with very low (003) crystallographic ratio were the most active samples and had the highest amount of $Bi_6O_6(OH)_3(NO_3)_3 \cdot 1.5H_2O$ which is why they are not part of the increasing activity trend (**Figure 37**) in function of the presence of (003).

All in all, the growth of $Bi_6O_6(OH)_3(NO_3)_3 \bullet 1.5H_2O$ was observed, which was a by-product, which decreases as the crystallization parameters are favoring further recrystallization processes, to achieve higher crystallinity (which means high MWCNT content, longer hydrothermal crystallization duration and higher temperature, as mentioned in the XRD section). This intermediate compound proved to be an efficient component in enhancing the photoactivity of the samples, although its exact functioning mechanism needs to be clarified. Also, the presence of $Bi_6O_6(OH)_3(NO_3)_3 \cdot 1.5H_2O$ influenced the band-gap value causing a blue-shift while enhancing the photoactivity. At last, the orientation of the crystals proved to be again a key factor but this time, a not yet reported (003) facet was suspected to be responsible in enhancing the overall photocatalytic activity of BiOBr and its composites with CNT.

In all the cases the question of stability arises, as always. To verify the stability and reusability of the investigated materials were tested under the conditions mentioned in the experimental section. The first step was to check the COD and TOC removal rate of the best performing material in order to verify if a constant decrease is visible or not. Surprisingly the mentioned values did not change at all suggesting that during the degradation an

inhibition mechanism or a poisoning process was underway, which did not permit the total mineralization of phenol.

As shown in the previous sections the obtained photocatalysts showed specific morphology, thus the next experiment was to verify the morphological stability after 3 successive photocatalytic runs of the best 3 samples for phenol degradation under the same conditions. At the first glance, no changes were observed in the SEM micrographs (**Figure 38**), meaning that the same plate-like morphology was obtained. Consequently, the concentration evolution of phenol was evaluated during the 3 photodegradation cycles (**Figure 39**). It was found that the photoactivity of all the tested samples were lowered after each test. The overall activity loss was around 50% and in one case activity regain was also observed (sample BiOBr + 1%CNT_150°C_4.5 h). The latter observation is rather unique and further investigations are needed to clarify this issue.

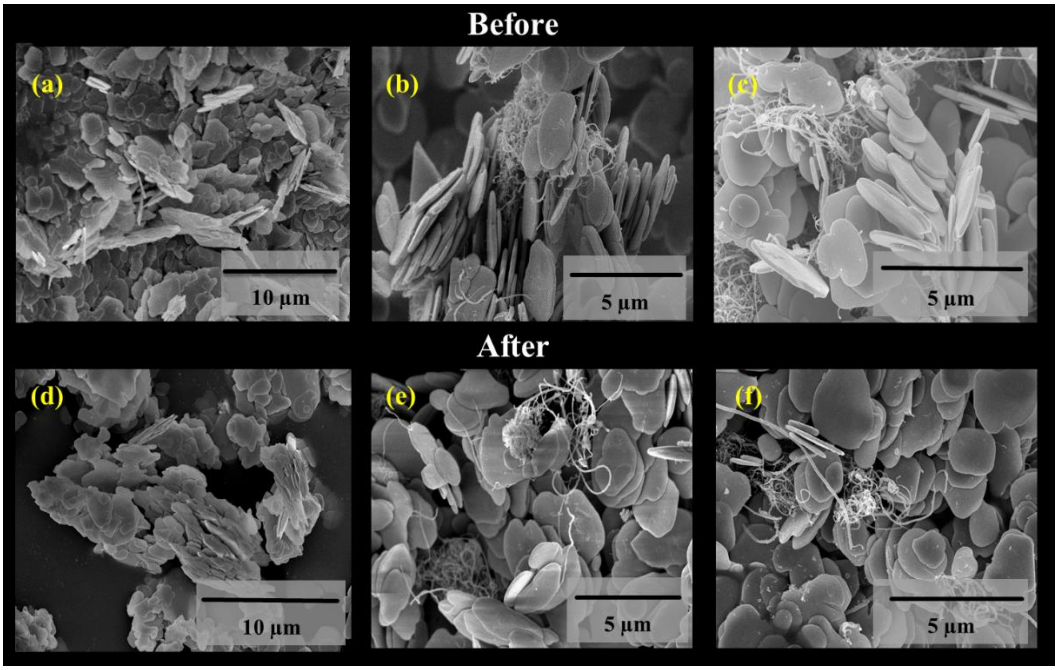

Figure 38. SEM micrographs of the samples before (a, b, c) and after (d, e, f) stability tests showing similar morphologies even after the stability tests (a) BiOBr_120°C_4.5 h, (b) BiOBr + 0.5%CNT_150°C_6.5 h, (c) BiOBr + 1%CNT_150°C_4.5 h and after the stability tests (d) BiOBr_120°C_4.5 h, (e) BiOBr + 0.5%CNT_150°C_6.5 h, (f) BiOBr + 1%CNT_150°C_4.5 h.

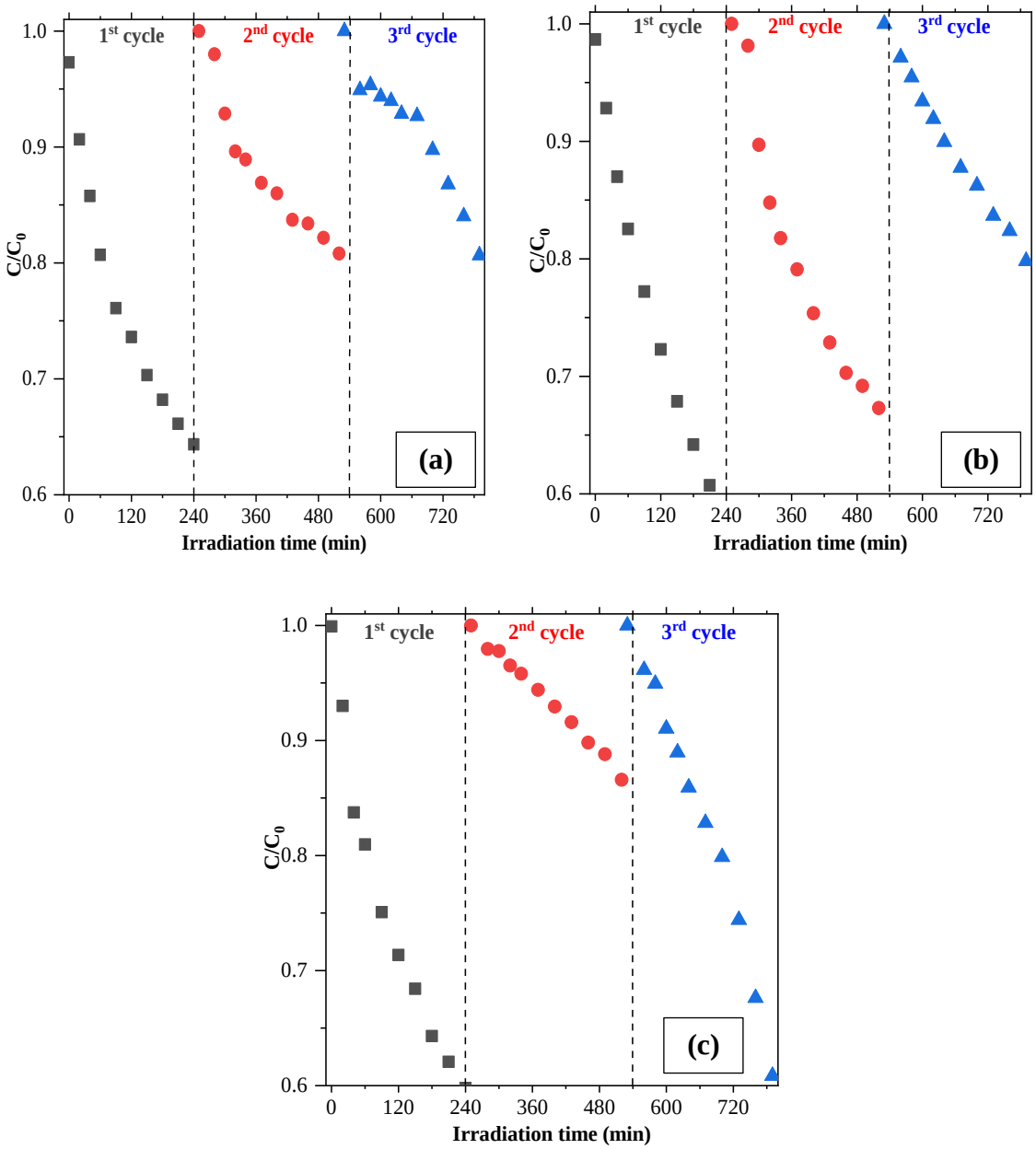

Figure 39. Photocatalytic reusability tests (3 cycles) of the investigated BiOBr and BiOBr/CNT samples (a) BiOBr_120°C_4.5 h, (b) BiOBr + 0.5%CNT_150°C_6.5 h and (c) BiOBr + 1%CNT_150°C_4.5 h, with the overall activity loss of 50% in all cases, except for BiOBr + 1%CNT_150°C_4.5 h.

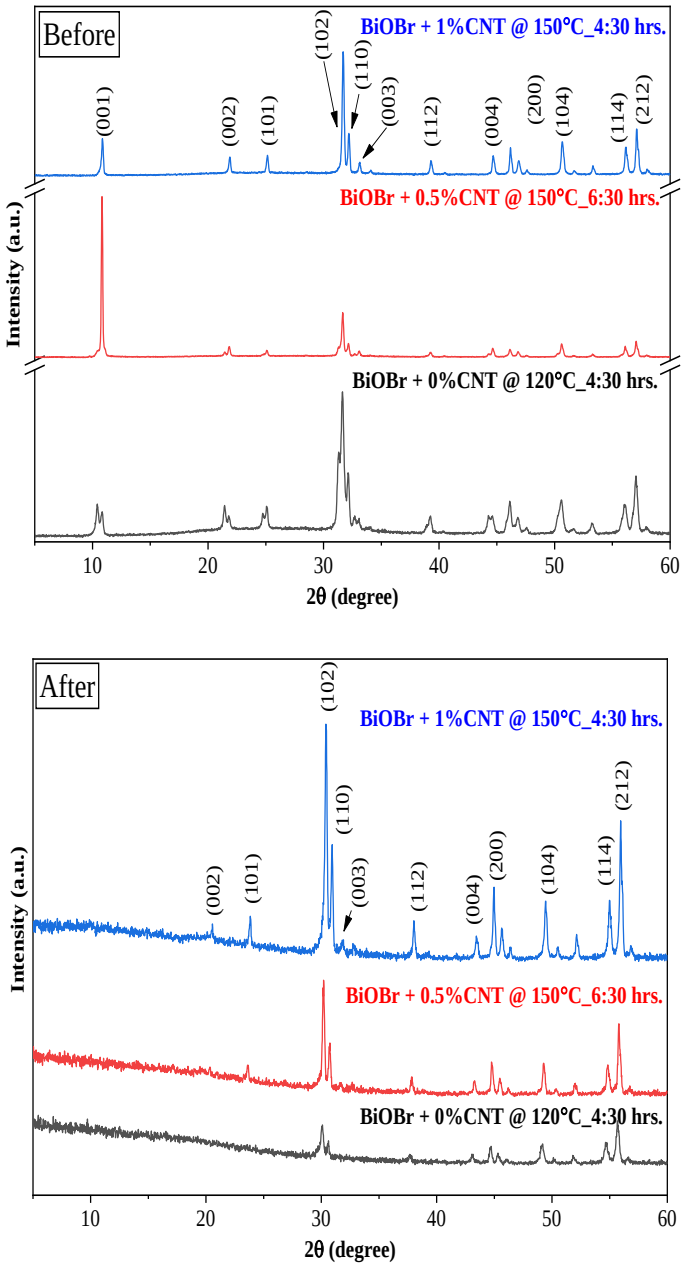

Figure 40. XRD of the samples before and after the stability tests showing a change in the crystal orientation which was associated with a decrease in crystallinity grade as well.

If no changes were observed in the morphology, the only explanation must lie in the crystal structure of the samples. The XRD patterns (**Figure 40**) of the studied samples showed significant changes. First, the $Bi_6O_6(OH)_3(NO_3)_3 \cdot 1.5H_2O$ related diffraction peaks totally disappeared, only the signals of BiOBr remained, emphasizing the recrystallization hypothesis mentioned at the beginning of this section. The (001) crystallographic plane did not give any signals in the reused material, pointing out a morphology preservation but total recrystallization, which was supported by the lower crystallinity grades and primary crystallite size values (a lowering of almost 50% in size, achieving values between 10.2-

24.5 nm). Moreover, the important (003) crystallographic plane disappeared in all the samples (except for BiOBr + 1% CNT_150°C_4.5 h, but also here its ratio was quite low). However, in the exception sample was registered the only activity increase which is new and direct evidence that the formation of (003) is beneficial.

6. Conclusion

This work involved the preparation of BiOX composites modified with CNT *via* hydrothermal synthesis. For the sample preparation, different compositions of CNTs were prepared (0.5, 1 and 2 wt.%) at different synthesis conditions (time and temperature). In order to gain the insight of factors responsible for diverse photocatalytic behavior of BiOXs, the identical synthesis conditions and CNT amount were used for all three BiOXs (X= Br, I, Cl). The impact of such parameters on the structural, morphological and optical properties of the BiOX material was studied. At last, the photocatalytic activity of the composites was measured for phenol and RhB as model pollutants. Besides this, a part of my study also involved the roles of CNT in our BiOX/CNT composites. Some significant correlations were attempted to be established between the photocatalytic activity and physicochemical properties of our BiOX and BiOX/CNT composites. The results obtained for the photodegradation of phenol, in this study, are promising since ordinary visible light was used as a source of irradiation, unlike Xe or Hg-lamps which are commonly reported in the literature.

One of the most significant findings of our work is based on the comparison of three BiOXs (X= Cl, I, Br) in terms of photocatalytic activity. Through the results obtained in our study, we can clearly say that different trends and dependencies were seen in all the three cases which proves that these trends observed may be true for one member of BiOX which may or may not be true in the case of other members of the BiOX family. For instance in the case of BiOCl, higher hydrothermal time and temperature conditions resulted in highly crystalline material which promoted the photocatalytic activity of BiOCl and in some case, highest CTN amount (2%) also resulted in higher photocatalytic activity of BiOCl. In some cases where CNT amount was 0.5 or 1%, detrimental effects on the performance of the BiOCl/CNT composites were seen. Contrary to this, the presence of CNT enhanced the photodegradation efficiency of BiOI/CNT composites together with the appearance of mixed bismuth oxoiodide phases which were iodide-deficient. In the case of BiOBr, again the presence of CNT deteriorated the photocatalytic activity of BiOBr/CNT composites rather the appearance of a bismuth nitrate (III) as a side-product resulted in higher photocatalytic activity for BiOBr. In addition to this, in some case, beneficial effect of a crystallographic plane (003) on the photodegradation efficiency of BiOBr was also seen. Therefore, it can be concluded here that different factors were responsible for the

enhancement of the photocatalytic activity of BiOXs depending on the type of halogen in BiOX.

Firstly, in the case of **BiOCl** and **BiOCl/CNT,** the addition of CNT had an influence on the crystallinity of the samples, *i.e.* higher degree of crystallization with increasing CNT amount. This higher degree of crystallization was also observed when higher temperature and longer duration was applied during the synthesis. This was the common observation in all three halides cases. The higher degree of crystallinity played an important role in the case of BiOCl, as discussed through significant correlations in our study. The samples with higher crystallite size showed higher photodegradation efficiency for both the pollutants due to the highly crystalline structures. When higher temperature and longer time was used, crystallization of BiOCl crystals completed and as a result, it resulted in highly crystallinity structures and hence higher photocatalytic activity, even at the lower CNT amount. The higher CNT amount (2%) showed the correlation with the optical property while no correlation was observed for lower CNT amount. This means that CNTs besides imparting crystallinity also influenced the optical properties of BiOCl which indicates different light absorption properties for all samples due to their different band gap energies The morphological properties of BiOCl and BiOCl/CNT composites were slightly influenced by CNT presence, *i.e.* from irregular microplates to the appearance of edges forming square-like plates started to appear with the addition of CNT.

Moving on to the **BiOI** and **BiOI/CNT** composite study, first and foremost, noticeable changes were observed through SEM investigations in morphology indicating the transformation from nanosheets to micro flower-like structures as the temperature increased. The composition of the final products revealed different ratios of Bi:I:O which apparently showed different light absorption and thus, different band gap energy. This is an indication of the presence of iodide-deficiency in the materials. As a result, the presence of these different iodide-deficient phases resulted in composition-dependent photocatalytic activity of the samples for the photodegradation of phenol and RhB under visible light irradiation. The higher degradation efficiency for phenol and RhB was achieved by BiOI/CNT composites than their respective reference samples. Moreover, the composites with microflower morphology showed superior photocatalytic performance for both pollutants. It was also observed that mixed phases in BiOI were present by changing hydrothermal crystallization conditions (time and temperature). These results provide a clear understanding of the instability of BiOI when heat treated (like calcination) and questions

its existence as a pure phase even at lower temperature conditions. At every point it becomes particularly important to identify the phases of BiOI so as to answer adequately which phase is responsible for the photocatalytic activity enhancement.

BiOBr and **BiOBr/CNT** samples obtained using different crystallization parameters and in the presence of CNT showed interesting results. The formation of **$Bi_6O_6(OH)_3(NO_3)_3 \cdot 1.5H_2O$** as a side-product was observed. The amount of this by-product decreases as the crystallization parameters favored further recrystallization processes in order to achieve higher crystallinity (high CNT content, longer hydrothermal crystallization duration and higher temperature). This intermediate compound proved to be an efficient component in enhancing the photocatalytic activity, although its exact functioning mechanism needs to be discovered. Also, the presence of $Bi_6O_6(OH)_3(NO_3)_3 \cdot 1.5H_2O$ influenced the band-gap value, causing a blue-shift while enhancing the photocatalytic activity. The morphology of the particles was microplate-like. The photocatalytic activity of the samples proved to be dependent also on the crystallite size, showing that also at higher primary particle size values, high activity can be achieved. The orientation of the crystals proved to be again a key factor, but a not yet reported (003) facet suggested to be responsible in enhancing the overall photocatalytic activity.

This study forms the basis for the materials like CNT that acts as a crystallinity promoter and can impart higher photocatalytic activity to the photocatalyst even if the semiconductor material loses its surface properties during the hydrothermal crystallization treatment. The loss of surface properties, here, means the lower surface areas for all the samples observed in our case. In other words, using electron conductive materials like CNT in appropriate concentration could compensates for the low surface area of the material with the higher crystallization that affects the overall photocatalytic activity of semiconductor material. Therefore, we can affirm here that in our study CNT acted as a crystallization promoting agent for each BiOX.

7. References

[1] Boretti A., *et al.* Nature Npj Clean Water, 2019. **2**, 15

[2] US EPA, Phenol Hazard Summary, Phenol, 2000. **1**, 95-108

[3] Chequer F.M.D., *et al.* Textile Dyes: Dyeing Process and Environmental Impact, G.A.R. de Oliveira (Ed.), in Intech Open, Rijeka, 2013, p. Ch. 6

[4] Velusamy S., *et al.* The Chemical Record, 2021. **21**, 1570-1610

[5] Chequer F.M. D., *et al.* Textile Dyes: Dyeing Process and Environmental Impact, in Intech Open, Eco-Friendly Textile Dyeing and Finishing, 2013. **41**411

[6] Rochkind M., *et al.* Molecules, 2015. **20**, 88-110

[7] Das M., *et al.* Journal of Molecular Catalysis A: Chemistry, 2014. **391**, 121-129

[8] Cui H.J., *et al.* Geochemical Transcriptions, 2015. **16**, 10-12

[9] Braslavsky S.E., *et al.* Glossary of terms used in photocatalysis and radiation catalysis, Pure Applied Chemistry, 2011. **83**, 931-1014

[10] Fujishima A., *et al.* Nature, 1972. **238**, 37-38

[11] Matthews R.W., *et al.* Journal of Catalysis, 1988. **111**, 264-272

[12] Dworschak D., *et al.* ACS Applied Material Interfaces, 2020. **12**, 51530-51536

[13] Quan H., *et al.* Inoranic Chemistry Frontiers, 2020. **7**, 817-838

[14] Biernat K., *et al.* The possibility of future biofuels production using waste carbon dioxide and solar energy, Fang Z. (Ed.), in Intech Open, 2013. 187–248, p. Ch. 5

[15] C.R. Edition, Industrial Inorganic Pigments, 2005. in: n.d.

[16] Maile F.J., *et al.* Journal of Progress in Organic Coatings, 2005. **54**, 150-163

[17] Michel C.R., *et al.* Sensors and Actuators B: Chemical, 2011. **160**, 271-277

[18] Briand G.G., *et al.* Chemical Reviews, ACS, 1999. **99**, 2601-2657

[19] Kijima N., *et al.* Applied Catalysis A: General, 2011. **206**, 237-244

[20] Ghosh R., *et al.* Tetrahedron Letters, 2004. **45**, 6775-6778

[21] U.S.P. Documents, United States Patent, 1978. **19**

[22] Cross L.E., *et al.* Materials Research Bulletin, 1971. **6**, 939-949

[23] Nava-Núñez M.Y., *et al.*, Catalysts, 2020. **10**, 226

[24] Li J., *et al.* Accounts of Chemical Research, ACS, 2017. **50**, 112-121

[25] Vadivel S., *et al.* Material Letters, 2018. **210**, 109-112

[26] Dutta S., *et al.* Journal of Alloys Compounds, 2020. **820**, 153115

[27] Xu Y., *et al.* Nanoscale, 2016. **8**, 2715-12722

[28] Xie F., *et al.* Journal of Materials Chemistry A, 2018. **6**, 13236-3243

[29] J. Li, *et al.* Nanoscale, 2014. **6**, 8473-8488

[30] Bhachu D.S., *et al.* Journal of Chemical Science, 2016. **7**, 4832-4841

[31] Singh S., *et al.* Korean Journal of Chemical Engineering, 2018. **35** (10)

[32] Monllor-Satoca D., *et al.* Catalysis Today, 2007. **129**, 247-255

[33] Alzamly A., *et al.* Journal of Photochemistry and Photobiology A: Chemistry, 2019. **375,** 30-39

[34] Hu L., *et al.* Journal of Alloys Compounds, 2015. **633**, 256-264

[35] Zhao L., *et al.* Physica B Condensed Matter, 2012. **407**, 3364-3370

[36] Ganose A.M., *et al.* Chemistry of Materials, 2016. **28**, 1980-1984

[37] Li Y., Wood-Polymer Composites, in Intech Open, 2011. **234**

[38] Anku W.W., *et al.* Bismuth-based nanoparticles as photocatalytic materials, Advanced applications and defects characterization, Zhou Y. (Ed.), in Intech Open: Bismuth, 2018. 59765

[39] Deng H., *et al.* Chemistry A European Journal, 2005. **11**, 6519-6524

[40] Durán-Álvarez J.C., *et al.* Journal of Visualized Experiments, 2019. **145**, 1-9

[41] Tadjarodi A., *et al.* Sciform, MDPI, 2014, 1-30

[42] He R., *et al.* Chinese Journal of Catalysis, 2014. **35**, 989-1007

[43] Wang X., *et al.* Journal of Catalysis, 2014. **310**, 100-108

[44] Hamaguchi T., *et al.* Journal of Photochemistry and Photobiology A: Chemistry, 2005. **173**, 99-105

[45] Joo J.B., *et al.* Journal of Materials Research, 2013. **28**, 362-368

[46] Nandiyanto A.B.D., *et al.* Arabian Journal of Chemistry, 2020. **13**, 1283-1296

[47] Jung K.Y., *et al.* Applied Catalysis A: General, 2002. **224**, 229-237

[48] Mera A.C., *et al.* Journal of Sol-Gel Science and Technology, 2020. **95**, 146-156

[49] Bárdos E., *et al.* Applied Surface Science, 2019. **479**, 745-756

[50] Imam S.S., *et al.* Journal of Environmental Chemical Engineering, 2021. **9**, 105404

[51] Zhang K.L., *et al.* Applied Catalysis B: Environmental, 2006. **68**, 125-129

[52] Zhao H., *et al.* Revised Advanced Science Engineering, 2014. **3**, 3-27

[53] Li G., *et al.* Environmenal Science Processes and Impacts, 2014. **16**, 1975-1980

[54] Hu J., *et al.* Applied Catalysis B: Environmental, 2014. 158-159, 182-189

[55] Li H., *et al.* Nanoscale, 2016. **8**, 1986-1993

[56] Xiao C., *et al.* ChemCatChem, 2019. **11**, 6467-6472

[57] Sánchez R. D., *et al.* Journal of Environmental Chemical Engineering, 2018. **6**, 1601-1612

[58] Zhao M., *et al.* Chinese Physical Letters, 2015. **32** , 098101

[59] Ge J., *et al.* RSC Advances, 2015. **5**, 49598-49605

[60] Sun J., *et al.* Chemical Physics Letters, 2018. **711**, 207-212

[61] Ding L., *et al.* Chemical Communications, 2016. **52**, 994-997

[62] Liu J., *et al.* Materials Letters, 2018. **233**, 174-176

[63] Arumugam M., *et al.* Journal of Industrial and Engineering Chemistry, 2020. **81**, 237-268

[64] Zhang X., *et al.* Journal of Physical Chemistry C, 2008, **112**, 3, 747–753

[65] Yan Q., *et al.* Journal of Nanoscience and Nanotechnology, 2016. **16**, 7731-7737

[66] Xiao X., *et al.* RSC Advances, 2011. **1**, 1099-1105

[67] Wang Y., *et al.* Journal of Physical Chemistry C, 2011. **115**, 14300-14308

[68] Wu G., *et al.* Journal of Colloid Interface Science, 2018. **510**, 228-236

[69] Putri A.A., *et al.* Journal of Electronic Materials, 2019. **49**, 1827-1834

[70] Wang X., *et al.* ACS Sustainable Chemistry and Engineering, 2019. **7**, 7900-7907

[71] Bai Y., *et al.* Chemical Engineering Journal, 2016. **304**, 454-460

[72] Ding C., *et al.* Journal of CO_2 Utilisation, 2016. **14**, 135-142

[73] P. Praveenkumar, *et al.* Materials Science in Semiconductor Processing, 2019. **104**, 104686

[74] You J., *et al.* Chemical Engineering Journal, 2019. **373**, 624-641.

[75] Varga G., *et al.* Molecular Catalysis, 2020. **493**, 111072

[76] Sajjad M., *et al.* AIP Advances, 2020. **10**, 075309

[77] Putri A.A., *et al.* Journal of Science: Advanced Materials and Devices, 2019. **4** 116-124

[78] Zhang G., *et al.* Materials Research Bulletin, 2014. **55**, 43-47

[79] Lei Y., *et al.* Dalton Transactions, 2010. **39**, 3273-3278

[80] Wang X., *et al.* Journal of Nanomaterials, 2020. 1013075

[81] Pennington A.M., *et al.* Rutgers, 2015. 81-87

[82] Garg S., *et al.* Materials, 2018. **11**, 1273

[83] Ge B., *et al.* Science China Technological Sciences, 2020. **63**, 859-865

[84] Fang Y.F., *et al.* Applied Mechanics and Materials, 2014. **488**, 248-251

[85] Li Y., *et al.* Journal of Alloys and Compounds, 2020. **816**, 152665

[86] Lyu J., *et al.* Journal of Physics and Chemistry of Solids, 2019. **129**, 61-70

[87] Gao Z., *et al.* Environmental Technology, 2019. **42**, 1-22

[88] Zhang H., *et al.* Journal of Material Sciences, 2020. **55**, 10785-10795

[89] Tang Q.Y., *et al.* Journal of Hazardous Materials, 2021. **407**, 124798

[90] K. Liu, *et al.* RSC Advances, 2019. **9**, 14391-14399

[91] Ai Z., *et al.* Journal of Physical Chemistry C, 2011. **115**, 25330-25337

[92] Wang Y., *et al.* Applied Surface Science, 2020. **514**, 145927

[93] Ge J., *et al.* Materials, 2019. **12**. 1916

[94] Jariwala D., *et al.* Chemical Society Reviews, 2013. **42**, 2824-2860

[95] Nuilek K., *et al.* Scientific Reports, 2020. **10**, 1-12

[96] Khalid N.R., *et al.* Ceramics International, 2017. **43**, 14552-14571

[97] Power A.C., *et al.* Nanotechnol. Revisions, 2018. **7,** 19-41

[98] Guillaume K. B., *et al.* Russian Journal of Non-Ferrous Metals, 2020. **61**, 112-118

[99] Shao P., *et al* .Journal of Applied Surface Science, 2015. **324**, 35-43

[100] Kumar S., *et al.* Beilstein Journal of Nanotechnology, 2017. **8**, 1571-1600

[101] Lu J., *et al.* in Photocatalysis, 2009. 481-506

[102] Syed N., *et al.* Frontier Chemistry, 2019. **7**, 1-7

[103] Varela A.S., *et al.* ACS Catalysis, 2019. **9**, 7270-7284

[104] Cao S., *et al.* Journal of Photochemistry and Photobiology C: Photochemistry, 2016. **27**, 72-99

[105] Hossain A., *et al.* Nano-Micro Letters, 2019. **11**, 1-26

[106] Jiang C., *et al.*, IOP Confernce Series: Earth and Environmental Sciences, 2019. **237**, 022049

[107] Liang Y.T., *et al.* Journal of Physical Chemistry Letter, 2012. **3**1, 760-1765

[108] Gusain R., *et al.* Applied Catalysis B: Environmental, 2016. **181**, 352-362

[109] Zhang Y., *et al.* Journal of Alloys and Compounds, 2016. **686**, 106-114

[110] Kandy M.M., *et al.* Sustainable Energy Fuels, 2020. **4**, 469-484

[111] Low J., *et al.* Energy Storage Materials, 2016. **3**, 24-35

[112] Sen Lin L., *et al.* Journal of Materials Chemistry B, 2014. **2**, 1031-1037

[113] Zhu J., *et al.* ACS Applied Material Interfaces, 2014. **6**, 16449-16465

[114] Zhao Z., *et al.* Nanoscale, 2015. **7**, 15-37

[115] Yousif E., *et al.* Archives of Nanomedicine Open Access Journal, 2018. **1**, 65-70

[116] Bárdos E., *et al.* Catal. Today, 2018. **300**, 28-38.

[117] Wang W., *et al.* Journal of Molecular Catalysis A: Chemical, 2005. **235**, 194-199

[118] Miribangul A., *et al.* Photochemistry and Photobiology, 2016. **92**, 523-527

[119] K. Wu, *et al.* Journal of Material Sciences, 2020. **55**, 15945-15962

[120] B. Réti, *et al.* Applied Catalysis A: General, 2014. **469**, 153-158

[121] L.L. Ma, *et al.* Nanotechnology, 2008. **19**, 115709

[122] T.A. Saleh, *et al.* The role of carbon nanotubes in enhancement of photocatalysis, Satoru Suzuki (Ed.), in: Intech Open. 2013. 38214

[123] S.E. Plush, *et al.* Journal of Carbon Research, 2017. **3** (2), 18

[124] S. Yin, *et al.* Clean - Soil, Air, Water, 2016. **44**, 781-787

[125] M. Su, *et al.* Journal of Hazardous Materials, 2012. 229–230, 72-82

[126] B. Weng, *et al.* Journal of Nanoparticle Research, 2014. **16**, 2766

[127] W. Guo, *et al.* Advanced Materials, 2012. **24**, 4761-4764

[128] S. Li, *et al.* Nanomaterials, 2017. **7**, 1-13

[129] J. Xia, *et al.* Ceramics International, 2014. **40**, 4607-4616

[130] D. Liu, *et al.* Chemical Physics Letter, 2019. **729** 42-48

[131] P. Kubelka, *et al.* An Article on Optics of Paint Layers, 31 (1931) 1–16.

[132] L. Wang, *et al.* ACS Sustainable Chemical Engineering, 2019. **7** , 3010–3017.

[133] F. Gao, *et al.* Phys. Chem. Chem. Phys. 2012. **14**, 10572-10578

[134] A. Phuruangrat, *et al.* Applied Physics A Materials Science and Processing, 2020. **126**, 1-8

[135] J. Xiong, *et al.* RSC Advances, 2011. **1**, 1542-1553

[136] D. Liu, *et al.* Chemical Physics Letter, 2019. **729**, 42-48

[137] S. Cao, *et al.* Journal of Photochemistry and Photobiology C: Photochemistry Revisions 2016. **27**, 72-99

[138] R. Kaveh, *et al.* Journal of Asian Ceramic Society, 2021. **9**, 343-365

[139] H. Liu, *et al.* Journal of Molecular Catalysis A: Chemical, 2014. **391**, 175-182

[140] J. Xia, *et al* Journal of Alloys and Compounds, 2017. **695**, 922-930

[141] A.A. Putri, *et al.* Applied Sciences, 2019. **9**, 3342

[142] X. Zhang, *et al.* Journal of Physical Chemistry C, 2010. **114**, 18198-18206

[143] M.M. Xu, *et al.* Water Science and Technology, 2015. **72**, 2122-2131

[144] C. Yu, *et al.* Materials Research Bulletin, 2011. **46**, 140-146

[145] X. Xiao, *et al.* Applied Catalysis B: Environmental, 2014. 148-149, 154-163

[146] H. Liu, *et al.* RSC Advances, 2020. **10**, 5913-5918

[147] C. Liu, *et al.* Dalton Transactions, 2016. **45**, 7720-7727

[148] J. Yang, *et al.* Applied Surface Science, 2014. **319**, 265–271

[149] J. Chen, *et al.* Physical Chemistry Chemical Physics, 2014. **16**, 20909-20914

[150] Z. Jiang, *et al.* Journal of Photochemistry and Photobiology A: Chemical, 2010. **212**, 8-13

[151] N. Sharma, *et al.* Applied Surface Science, 2021. **565**, 150605

[152] Y. Yang, *et al.* Chemosphere, 2013. **93**, 701-707

[153] Xie L., *et al.* Materials Chemistry and Physics, 2012. **136**, 309-312

[154] L.M. Yang, *et al.* RSC Advances, 2015. **5**, 79715-79723

[155] B. Réti, *et al.* Journal of Molecular Catalysis A: Chemical, 2016. **414**, 140-147

[156] A.N. Christensen, *et al.* Journal of Chemical Society, Dalton Transactions, 2000. 265-270

[157] D. Xiong, *et al.* Science of the Total Environment, 2011. **409**, 1444-1452

[158] Z. Pap, *et al.* Journal of Molecular Structure, 2014. **1073**, 157-163

[159] C. Yuan, *et al.* IOP Confernce Series: Mater. Sci. Eng, 2019. **585**, 012040

[160] Y. Peng, *et al.* CrystEngComm, 2017. **19**, 6473-6480

8. Acknowledgement

I would like to express my sincere gratitude to my mentor and supervisor, Prof. Dr. Hernadi Klara, for her technical and professional guidance. I thank her for giving me an opportunity to be a part of her wonderful research team. Working with her is a lifetime experience for me that I will always cherish in my life. She has been a constant source of motivation for me. I am glad that I could pursue my doctoral studies under her guidance. Her positive attitude towards everything has encouraged me to surpass all the obstacles during my studies. This dissertation could not be completed without the help of Dr. Pap Zsolt, one of my co-supervisors, who has been there, day and night, and has assisted me with his brilliant ideas and knowledge. I would also like to express my gratitude to Dr. Seema Garg, my other co-supervisor, for giving me tremendous support throughout the work. I cannot thank her enough for introducing me to Prof. Hernadi and her research group.

Sincere thanks to all my colleagues from the research team for making the workplace comfortable. Our mini coffee breaks and off-topic discussions have helped me in many ways and also ease the pressure of work and made a friendly-environment.

My special thanks to all of my friends for their moral support, especially Hussein, Erdensuvdha, and Elham Seifi who stood by me through thick and thin. They have helped me in making this journey memorable for me. I appreciate your immense support. Thank you all for being a part of the most important chapter of my life.

Last but not the least, I would like to thank my beautiful family: my parents, my sister and brother, Tanvi and Janit, for their love, care, encouragement, inspiration and faith in me. The support from my family has been a driving force for me and helped me in overcoming every situation no matter how challenging or hard it was. I sincerely thank my family for believing in my ability to succeed.

I would also like to take this opportunity to acknowledge the Department of Applied and Environmental Sciences, Doctoral School, for offering me the chance to pursue my doctoral studies at University of Szeged. Lastly, I would like to thank *Indo-Hungarian TET projec*t (TET_15_IN-1-2016-0013), *Tempus Public Foundation (Bilateral Scholarship Program)* and *Advanced Materials and Intelligent Technologies Higher Education and Industrial Cooperation Centre* (GINOP- 2.3.4-15-2016-00004) University of Miskolc, for providing financial support to conduct the research work of my doctoral study smoothly.

9. APPENDIX

Appendix 1. Average primary particle sizes, specific surface areas and band gaps of the investigated BiOCl and BiOCl/CNT composites prepared at 120°C and 150°C.

Sample Name	Primary crystallite size (nm)	Specific surface area (m^2/g)	Band gap energy E_g (eV)
BiOCl/CNT prepared at 120°C (4.5 and 6.5 h)			
BiOCl_120°C_4.5 h	~ 77	7	3.38
BiOCl + 0.5%CNT	~ 71	8	3.15
BiOCl + 1%CNT	~ 73	6.7	3.17
BiOCl + 2%CNT	~ 78	3	3.21
BiOCl _120°C_6.5 h	~ 65	2.7	3.35
BiOCl + 0.5%CNT	~ 69	10.5	3.29
BiOCl + 1%CNT	~ 73	1.8	3.17
BiOCl + 2%CNT	~ 61	2.6	3.17
BiOCl/CNT prepared at 150°C (4.5 and 6.5 h)			
BiOCl_150°C_4.5 h	> 120	3	3.28
BiOCl + 0.5%CNT	> 120	6.2	3.01
BiOCl + 1%CNT	~ 90	4	2.94
BiOCl + 2%CNT	43	8.2	2.96
BiOCl _150°C_6.5 h	> 125	6.4	3.26
BiOCl + 0.5%CNT	> 110	5.5	3.17
BiOCl + 1%CNT	~ 94	2.3	3.03
BiOCl + 2%CNT	43	3.7	3.01

Appendix 2. Average primary particle sizes, specific surface areas and band gaps of the investigated BiOI and BiOI/CNT composites prepared at 120°C and 150°C.

Sample Name	Primary crystallite size (nm)	Specific surface area (m^2/g)	Band gap energy E_g (eV)
BiOI/CNT prepared at 120°C (4.5 and 6.5 h)			
BiOI_120°C_4.5 h	> 142	4	1.79
BiOI + 0.5%CNT	~ 69	4	1.6
BiOI + 1%CNT	~ 76	9.1	1.67
BiOI + 2%CNT	~ 67	7.8	1.6
BiOI _120°C_6.5 h	51	4	1.64
BiOI + 0.5%CNT	~ 63	6	1.73
BiOI + 1%CNT	~ 67	6.4	1.67
BiOI + 2%CNT	~ 72	9.1	1.61
BiOI/CNT prepared at 150°C (4.5 and 6.5 h)			
BiOI _150°C_4.5 h	~80	3.6	1.82
BiOI + 0.5%CNT	~ 60	4.2	1.74
BiOI + 1%CNT	~ 75	6.4	1.7
BiOI + 2%CNT	~ 56	9.2	1.53
BiOI _150°C_6.5 h	~ 90	2.6	1.79
BiOI + 0.5%CNT	~ 66	5	1.65
BiOI + 1%CNT	~ 71	4.8	1.57
BiOI + 2%CNT	~ 68	6.7	1.46

Appendix 3. Average primary particle sizes, specific surface areas and band gaps of the investigated BiOBr and BiOBr/CNT composites prepared at 120°C and 150°C.

Sample Name	Primary crystallite size (nm)	Specific surface area (m^2/g)	Band gap energy E_g (eV)
BiOBr/CNT prepared at 120°C (4.5 and 6.5 h)			
BiOBr_120°C_4.5 h	33.75	7.3	2.84
BiOBr + 0.5%CNT	~ 85.25	4.3	2.69
BiOBr + 1%CNT	~ 77.85	5.2	2.55
BiOBr + 2%CNT	~ 96.6	5	2.58
BiOBr_120°C_6.5 h	61	3	2.83
BiOBr + 0.5%CNT	~ 92	2.8	2.48
BiOBr + 1%CNT	> 110	4	2.65
BiOBr + 2%CNT	> 103.2	4.5	2.48
BiOBr/CNT prepared at 150°C (4.5 and 6.5 h)			
BiOBr_150°C_4.5 h	> 102	6.5	2.81
BiOBr + 0.5%CNT	~ 90	4.3	2.67
BiOBr + 1%CNT	>104	4	2.73
BiOBr + 2%CNT	~ 95	5.3	2.38
BiOBr_150°C_6.5 h	52	2.3	2.82
BiOBr + 0.5%CNT	~ 89	3.3	2.61
BiOBr + 1%CNT	~ 74	4.6	2.65
BiOBr + 2%CNT	~ 98	5	2.48